UNIVERSITY OF OKLAHOMA

GRADUATE COLLEGE

CHEMICAL MODELING OF UNSTABLE INTERMEDIATES IN HEME−MEDIATED NO_X BIOLOGY

A DISSERTATION

SUBMITTED TO THE GRADUATE FACULTY

in partial fulfillment of the requirements for the

Degree of

DOCTOR OF PHILOSOPHY

By

ERWIN G. ABUCAYON
Norman, Oklahoma
2017

CHEMICAL MODELING OF UNSTABLE INTERMEDIATES
IN HEME−MEDIATED NO_X BIOLOGY

A DISSERTATION APPROVED FOR THE
DEPARTMENT OF CHEMISTRY AND BIOCHEMISTRY

BY

_____
Dr. George B. Richter-Addo, Chair

_____
Dr. Mark A. Nanny

_____
Dr. Ann H. West

_____
Dr. Robert K. Thomson

_____
Dr. Zhibo Yang

This work is dedicated to my beloved parents and siblings.

Acknowledgments

I would like to express my sincere gratitude to my research mentor, Dr. George B. Richter-Addo for his unconditional support and for always believing in me. I am extremely fortunate and grateful for his motivation, unwavering enthusiasm, and immense knowledge in bioinorganic research.

My sincere thanks goes to my research advisory committee; Drs. Daniel Glatzhofer, Ann West, Robert Thomson, Zhibo Yang, and Mark Nanny for their suggestions and advice throughout my graduate studies.

I would like to give special thanks to both past and present members of the Richter-Addo laboratory; to (i) Dr. Dennis Awasabisah who introduced me to the lab and taught me new synthetic skills, spectroscopy, and electrochemical techniques during my first year, (ii) Dr. Nan Xu who provided the foundation that forms the basis of the first chapter of my dissertation, (iii) Dr. Jun Yi for the many interesting scientific discussions that we had, and (iv) Dr. Guan Ye, Dr. Bing Wang, Neda Hessami, Jimmy Herndon, Samantha Powell, Jeremy Zink, Mike Gorbett, Viridiana Hererra, and Megan Ayala for the stimulating conversations that we had about science and non-science matters.

I would like to thank our research collaborators; Dr. Mike Shaw (SIUE) for research discussions and critical suggestions regarding some of our experiments, Dr. Yong Zhang (SIT) for the very fruitful collaboration and the time that he spent performing advanced DFT calculations to verify some of our novel experiments, Dr. Naresh Dalal (FSU) for the advanced EPR and magnetization studies for our iron−NONOate complexes, and Dr. Ralph Tanner (OU Department of Microbiology and Plant Botany) for conducting gas chromatographic detection (GC-TCD) of H_2 gas for one of our

important HNO experiments. I was also deeply indebted to the research support staff in our department; to Dr. Douglas Powell for his patience in helping me with my crystallographic work; Dr. Susan Nimmo for her assistance with low temperature NMR spectroscopy; Dr. Steve Foster for helping me with mass spectrometry; Jim Cornell for the glass-blowing work, as well as Chad, Karl, and Jeff in the electronic shop for all their help.

I am very grateful to my family who were a constant source of my strength during my Ph.D. studies. Special thanks to my special someone, Melissa Borlagdan, for the unconditional love, support, understanding, and encouragement throughout my Ph.D. years.

We are extremely grateful to the U.S. National Science Foundation (CHE-1213674 and CHE-1566509) for funding this work. Finally, I would like to express my gratitude to the university for the Nancy Mergler Dissertation Completion Fellowship (OU) during the final year of my graduate work.

Table of Contents

List of Tables

List of Figures

Abstract

This dissertation describes the preparation, characterization, and reactivity of several critical unstable intermediates of relevance to the global N-cycle. Their spectroscopic signatures and chemical reactivities were used to correlate and delineate their observed biological effects and functions in nature.

Chapter 1 introduces the importance of nitric oxide (NO) in physiology and its involvement in the N-cycle. The chapter briefly overviews the complexity of metal-mediated NO_x activation in physiology, agriculture, and the environment. Also described in this chapter are significant areas of N-chemistry that are currently underexplored, but important to study if we are to move the field forward.

Chapter 2 highlights the reactions of organic *C*-NONOate compounds with iron porphyrins. NONOates (diazeniumdiolates) containing the $[X\{N_2O_2\}]^-$ functional group are frequently employed as nitric oxide (NO) donors in biology, and some NONOates have been shown to bind to metalloenzymes. In this chapter, the preparation, crystal structures, detailed magnetic behavior, redox properties, and reactivities of two alkyl *C*-NONOate complexes of heme models, namely (OEP)Fe(η^2-ON(*t*-Bu)NO) (**1**) and (TPP)Fe(η^2-ON(*t*-Bu)NO) (**2**) (OEP = octaethylporphyrinato dianion, TPP = tetraphenylporphyrinato dianion) are presented. The compounds display the unusual NONOate *O,O*-bidentate binding mode for porphyrins, resulting in significant apical Fe displacements (+0.60 Å for **1**, and +0.69 Å for **2**) towards the axial ligands. Magnetic susceptibility and magnetization measurements recorded in the 1.8–300 K temperature range at magnetic fields from 0.02 to 5T, yielded magnetic moments of 5.976 and 5.974 Bohr magnetons for **1** and **2**, respectively, clearly identifying them as high-spin ($S = {}^5/_2$)

ferric compounds. Variable-frequency (9.4 GHz and 34.5 GHz) EPR measurements, coupled with computer simulations, confirmed the magnetization results and yielded more precise values for the spin Hamiltonian parameters : g_{avg} = 2.00 ± 0.03, $|D|$ = 3.89 ± 0.09 cm^{-1}, and E/D = 0.07 ± 0.01 for both compounds, where D and E are the axial and rhombic zero field splittings. IR spectroelectrochemistry studies reveal that the first oxidations of these compounds occur at the porphyrin macrocyles and not at the Fe-NONOate moieties. Reactions of **1** and **2** with a histidine mimic (1-MeIm) generates RNO and NO, both of which may bind to the metal center if sterics allow, as shown by a comparative study with the Cupferron complex (T(*p*-OMe)PP)Fe(η^2-ON(Ph)NO). Protonation of **1** and **2** yields N_2O as a gaseous product, presumably from the initial generation of HNO that dimerizes to the observed N_2O product.

Chapter 3 focuses on probing the previously unknown key reaction steps and intermediates in the NO to N_2O reduction by fungal cyt P450 nitric oxide reductase (NOR) using heme models. Low temperature IR and ^{1}H NMR spectroscopic characterizations of (por)Fe(HNO)(L) (por = OEP, PPDME, TTP; L = 5-MeIm, 1-MeIm, Im) derivatives from the reactions of hydride with ferric−NO species are described. The ν_{NO} bands of the heme model Fe−HNO products are in the range of 1381 cm^{-1} to 1389 cm^{-1}. ^{1}H NMR spectroscopy, a more sensitive technique for the bound HNO, shows mild *cis* and *trans* effects in the chemical shifts observed in the 13.65−14.26 ppm range. The ν_{NO} bands, ^{1}H NMR chemical shifts, and coupling constants ($J_{^{15}N\text{-}H}$ ~77 Hz) of the ferrous Fe−HNO derivatives are close to those from literature values. Results from the DFT calculations are consistent with the direct attack of H^- at the nitrosyl N-atom to form the Fe−HNO products. Interestingly, these Fe−HNO species exhibit varied decomposition

pathways, one involving H_2 formation from Fe(N−H)O bond cleavage and the other involving Fe−N(H)O bond cleavage to generate N_2O gas. Importantly, these Fe−HNO species react with external NO to form N_2O in which the central N-atom and O-atom originate from the external NO reagent, and the terminal N-atom derives from the bound HNO. This is the first experimental evidence of the N−N coupling step in heme models supporting Fe−HNO as an active intermediate in NO reduction to N_2O catalyzed by cyt P450nor. Differential reactivity of six- and five-coordinate ferric heme−NO models with hydride is also described in this chapter. The formation of Fe−HNO from hydride attack at the bound six-coordinate ferric nitrosyl was shown to be thermodynamically and kinetically favorable. However, for the five-coordinate case, although Fe−HNO formation is thermodynamically favored, (NO)Fe−H formation is the kinetically favored and experimentally observed outcome.

The last chapter (Chapter 4) of my dissertation centers on the transformation of metal−NO to metal−RNO derivatives via attack of *C*-based nucleophiles to form new carbon−nitrogen bonds. *C*−based nucleophiles react at two sites of ferric−NO compounds, (i) at the nitrosyl N-atom to afford a low yield ferrous−RNO derivative, and (ii) at the Fe center to form a high yield organometallic Fe−phenyl product. In the case of the Ru-analogues, the nucleophilic reactions of $\{RuNO\}^6$ species with phenyl anions result in a reasonable yield of the Ru-PhNO product. The (OEP)Ru(PhNO)(5-MeIm) product from the reaction of [(OEP)Ru(NO)(5-MeIm)]BF_4 with the phenyl nucleophile was characterized by IR spectroscopy, and its molecular structure confirmed by X-ray crystallography. The formation of organic RNO compounds from the inorganic metal−NO precursors via nucleophilic attack by *C*−based nucleophiles represents the first

experimental evidence of the conversion of inorganic-NO_x to organo-NO derivatives mediated by heme models. This chemistry was extended to nitrogen−nitrogen bond formation in these systems using an *N*−based nucleophile (NaN_3). Nucleophilic attack of azide (N_3^-) at a bound NO^+ in $\{MNO\}^6$ (M = Fe, Ru) species generates N_2O gas as detected by gas phase IR spectroscopy.

Chapter 1. Introduction

Living systems depend on a wide range of proteins to survive. In fact, proteins are an integral part of all living things. Proteins are made up of covalently-linked chains of amino acids that vary in the linear sequence of amino acids. Curiously, however, many proteins are not functional unless they recruit additional non-protein components called cofactors that allow the proteins to perform specific chemistry on substrates (Fig. 1.1A).

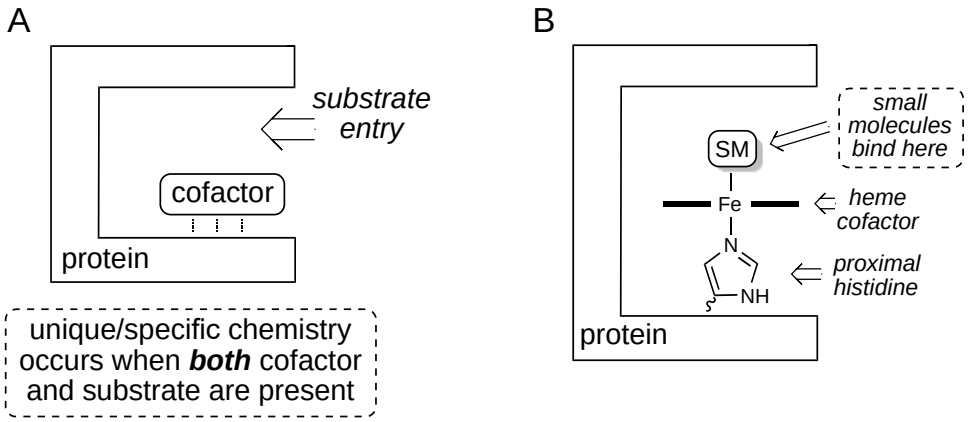

Figure 1.1. (A) Sketch of the active site of a protein with its cofactor. (B) An example of a protein with a heme cofactor.

For example, the liver enzyme cytochrome P450 detoxifies xenobiotics only when electron transfer cofactors (*e.g.*, heme, NAD(P)H) are present.[1] Some cofactors such as heme contain metals (Fig. 1.1B), while others do not. Interestingly, deficiencies of several metals are linked to specific health effects; for example, Mg (muscle cramps), Cu (artery weakness), Zn (skin damage), Mn (infertility), Cr (diabetes), and Ni (growth suppression).[2]

My thesis research deals with the role of metalloproteins (*i.e.*, proteins with metal-containing cofactors) in the global nitrogen cycle. Unlike the element carbon that is abundant on the earth's surface, for example in carbohydrates and proteins, the element nitrogen is mostly "trapped" as the non-reactive N_2 gas in the atmosphere, comprising ~78% of the atmosphere. Bacteria and fungi have evolved specialized enzymes that can, and do, interconvert various N-containing species such as nitrite (NO_2^-), ammonia (NH_3), hydroxylamine (NH_2OH), nitric oxide (NO), and nitrous oxide (N_2O; "laughing gas").[3] *While much is known about the role that bacteria and fungi play in conversions between these N-species, there is surprisingly very little known about exactly how the metalloenzymes of bacteria and fungi actually work to achieve their observed chemistry.*

My thesis research focuses on modeling the chemistry of metalloproteins containing heme (Fe porphyrin) cofactors ligated and attached to the protein chain by a proximal histidine amino acid sidechain (Fig. 1.1B). The natural heme, the most common being Fe−protoporphyrin−IX (heme *b*), is shown on the left of Figure 1.2. To unravel the

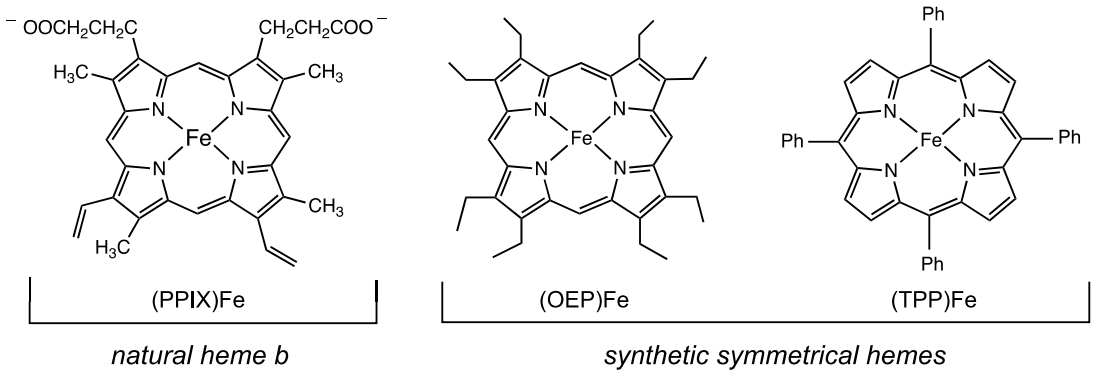

Figure 1.2. Chemical drawings of the natural heme *b* and representative synthetic porphyrins used in my work.

chemistry enabled by this heme cofactor which is normally in a hydrophobic active site of a protein, bioinorganic chemists model these heme proteins by employing symmetrical synthetic porphyrins such as octaethylporphyrin (OEP) and tetraphenylporphyrin (TPP) (middle and right of Fig. 1.2). These synthetic porphyrins are more amenable to ^{1}H NMR spectroscopic analyses, and perform the target reactions in the absence of water and air (*i.e.*, under hydrophobic and anaerobic conditions).

In line with this, the three main chapters of my dissertation are centered on modeling various heme−NO active site species and their derivatives as shown schematically in Figure 1.3; these species are relevant to biology, physiology, and the environment.

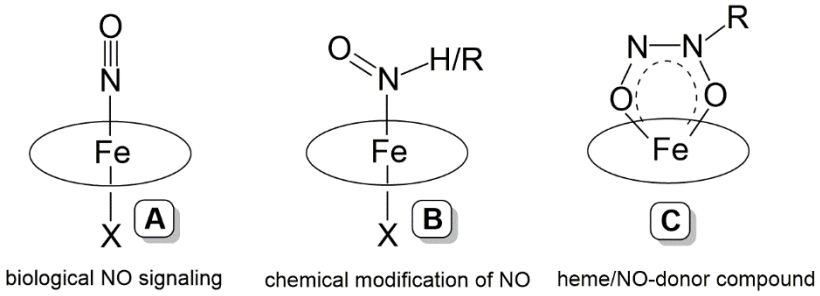

Fig. 1.3. Examples of active site heme−NO_x intermediates involved in NO biology and in the global N-cycle.

Nitric oxide (NO) is a signaling molecule that is an important component in processes leading to cardiovascular regulation, neurotransmission, the immune response, and other critical physiological processes.[4-6] Such physiological effects stem from the interactions of NO with heme proteins, the common receptors of NO in biological systems. In mammalian biology, a low concentration of NO is produced as a byproduct of the oxidation of L-arginine to citrulline catalyzed by a heme-containing enzyme nitric

oxide synthase (NOS).[7] One particularly important characteristic associated with heme−NO signaling is the *trans* effect, a weakening/lengthening of the Fe−$N_{(his)}$ bond *trans* to NO (*i.e.*, on the opposite side of the Fe-bound NO ligand; *e.g.*, Fig. 1.1B). It has been speculated by many researchers that the cleavage of the *trans* Fe−$N_{(his)}$ bond in the heme cofactor of soluble guanylyl cyclase (sGC) during NO binding triggers sGC activity in the mammalian signaling pathway.[7,8] Although the chemistry and biochemistry of the NO molecule is relatively well-established, its less known redox sibling HNO is currently attracting attention as researchers have found that it elicits physiological functions distinct from that of NO. For example, in the cardiovascular system, while NO only relaxes the muscles, HNO is capable of inducing both muscle relaxation and contraction.[9,10]

Interestingly, NO is toxic to bacteria and fungi, and they have designed machinery to detoxify NO to the less toxic gas N_2O. This biotransformation is catalyzed by Fe-containing metalloproteins such as the NO reductases (NORs) that utilize heme as cofactors (in fungi), and a combination of heme/nonheme cofactors (in bacteria) for the NO to N_2O transformation.[11,12] This transformation is not only an important component of the global N-cycle, but is also relevant to growing concerns over climate change, as N_2O is a known potent greenhouse gas.[13-15] In addition to the significant role of HNO in mammalian physiology, Fe-bound HNO (Fe−HNO; Fig.1.3B) species have been proposed as important intermediates in the fungal NO detoxification pathway,[16,17] nitrite reduction by cytochrome *c* nitrite reductase (*cc*NIR),[18,19] and in the reaction mechanism of hydroxylamine oxidoreductase.[20]

One important component of N-chemistry is the "inorganic−NO_x to organo−N conversion" which is of great significance in the field of agriculture and the environment

as highlighted by the National Science Foundation's "Innovation at the Nexus of Food, Energy, and Water Systems (INFEWS)" program launched in 2015.[21] Huge gaps in knowledge still exist in this inorganic−NOx to organo−NOx field. This has relevance to agriculture in terms of determining the metal-catalyzed systems that convert inorganic-N fertilizer (*e.g.*, NO_2^-/NO_3^-) to organo-N species as part of the plant N-uptake process. Directly relevant to this transformation are C−N bond-forming reactions that possibly link NO to that of organic nitroso (R−NO) compounds during NO_x activation. Some RNO compounds are also known to be carcinogenic and capable of deactivating cyt P450 enzymes,[22,23] and damaging heme proteins[24] by binding to the Fe centers of the hemes to form stable Fe−RNO adducts. The known pathways for generating RNO in biology are through oxidative amine and reductive organic-nitro compound metabolism. In addition, ferric heme Fe-NO species as intermediates of NO interactions with hemes are very prevalent. These formally $(FeNO)^+$ species have been invoked as intermediates during biological nitrosations of heme proteins such as cyt cd_1[25] and myoglobin (Mb)[26] possibly via nucleophilic attack of the substrates at the metal-bound NO^+ to generate RNO. Such a nucleophilic reaction of a substrate with a ferric−NO species is related to the transformation of inorganic−NO_x to organo−NO derivatives which, as mentioned above, is an underexplored but highly urgent and significant research area that is critical in NO biology and plays a huge part in the global nitrogen inventory.

Much attention has been given in the last decade to the design of NO and HNO donor compounds. One class of organic compounds that shows promise for donating NO/HNO under physiological conditions are the diazeniumdiolates (NONOates).[27-30] Detailed reviews on the plausible mechanisms of NO release from NONOates have been

reported.[27,28] NONOates interact with metals via different binding modes;[31,32] one of these is the unusual bidentate (por)Fe−NONOate mode shown in Figure 1.3C. Most of the literature reports in this area to date focus on the effect of pH on the release of NO from uncomplexed NONOates[33,34] however, very little is still known about metal-mediated NO release from these compounds. [31,35,36] My first project as a formal member of the Richter-Addo group focused on the reactions of NONOates (NO-donor compounds) with Fe porphyrins as possible models for the interactions of these NO-donor compounds with heme active sites. I probed this chemistry by examining the mechanistic aspects of this reaction using biologically relevant species such as histidine mimic 1-MeIm and protons. Questions I had to help guide my research included: how do heme groups interact with NO-donor compounds, and what are the subsequent chemical steps that occur after NO release? These questions form the basis of Chapter **2** of my dissertation.

Chapter **3** of my dissertation stems from our interest in studying the binding of NO to the less studied ferric porphyrins with histidine mimics (*e.g.*, 5-MeIm) as *trans* ligands. Although there are a handful of ferric nitrosyl [(por)Fe(NO)(*histidine mimic*)]$^{+}$ complexes[37] that were reported prior to my work in this area, these reported species were unstable and prone to loss of NO from the ferric sites, limiting their utility for further reactivity studies. The main focus of this chapter was to explore and examine the factors that lead to successful hydride addition at ferric−NO to form Fe−HNO, a known key intermediate in the fungal cyt P450 NO reduction *en route* to N_2O formation.

As noted above, it is known that nitroso (RNO) metabolites are involved in some reaction pathways with heme biomolecules as intermediates during amine and organic

nitro-compound metabolism.[38,39] For example, the binding of RNO to heme active sites to form heme−RNO adducts has been implicated in nitrobenzene poisoning.[39] A significant gap in knowledge I identified is the transformation of NO to RNO derivatives during metal-mediated NO_x activation. Such a transformation is also related to the conversion of inorganic−NO_x to organo−N compounds important in agriculture. One of my particular interests, that forms the basis of Chapter **4** of my dissertation, is the *in-situ* generation of heme−XNO from the reactions of the ferric $\{FeNO\}^6$ species, and their reactions with X-nucleophiles ($X = C^-$, N^-) to form new N−C and N−N bonds.

It is my hope that this dissertation will provide new and relevant information to help researchers advance their fundamental knowledge in the chemical biology of heme−NO_x, and in the global N-cycle.

References

1. Guengerich, F. P., ed. *Human Cytochrome P450 Enzymes*. 3rd Ed. ed. Cytochrome P450: Structure, Mechanism, and Biochemistry, ed. P.R. Ortiz de Montellano. **2005**, Kluwer Academic / Plenum: New York. pp 377-530.

2. Bertini, I., Gray, H., Lippard, S., and Valentine, J. S. *Bioinorganic Chemistry*. University Science Book: California, **1994**.

3. Tavares, P., Pereira, A. S., Moura, J. J. G., and Moura, I. *J. Inorg. Biochem.* **2006**, *100*, 2087-2100.

4. Butler, A. R. and Williams, D. L. H. *Chem. Soc. Rev.* **1993**, *22*, 233-241.

5. Culotta, E. and Koshland, D. E. *Science* **1992**, *258*, 1862-1865.

6. Averill, B. A. *Chem. Rev.* **1996**, *96*, 2951-2964.

7. Derbyshire, E. R. and Marletta, M. A. *Annu. Rev. Biochem.* **2012**, *81*, 533-559.

8. Herzik, M. A., Jonnalagadda, R., Kuriyan, J., and Marletta, M. A. *Proc. Natl. Acad. Sci. U.S.A.* **2014**, *111*, E4156-E4164.

9. Paolocci, N., Jackson, M. I., Lopez, B. E., Miranda, K., Tocchetti, C. G., Wink, D. A., Hobbs, A. J., and Fukuto, J. M. *Pharmacol. Ther.* **2007**, *113*, 442-458.

10. Miranda, K. M. *Coord. Chem. Rev.* **2005**, *249*, 433-455.

11. Shoun, H., Fushinobu, S., Jiang, L., Kim, S. W., and Wakagi, T. *Philos. Trans. R Soc. B Biol. Sci.* **2012**, *367*, 1186-1194.

12. Moenne-Loccoz, P. *Nat. Prod. Rep.* **2007**, *24*, 610-620.

13. Zhang, H., Wennberg, P. O., Wu, V. H., and Blake, G. A. *Geophys. Res. Lett.* **2000**, *27*, 2481-2484.

14. Yamazaki, T., Hozuki, T., Arai, K., Toyoda, S., Koba, K., Fujiwara, T., and Yoshida, N. *Biogeosciences* **2014**, *11*, 2679-2689.

15. Tolman, W. B. *Angew. Chem. Int. Ed.* **2010**, *49*, 1018-1024.

16. Daiber, A., Shoun, H., and Ullrich, V. *J. Inorg. Biochem.* **2005**, *99*, 185-193.

17. Kramos, B., Menyhard, D. K., and Olah, J. *J. Phys. Chem. B* **2012**, *116*, 872-885.

18. Einsle, O., Messerschmidt, A., Huber, R., Kroneck, P. M. H., and Neese, F. *J. Am. Chem. Soc.* **2002**, *124*, 11737-11745.

19. Bykov, D. and Neese, F. *Inorg. Chem.* **2015**, *54*, 9303-9316.

20. Cabail, M. Z., Kostera, J., and Pacheco, A. A. *Inorg. Chem.* **2005**, *44*, 225-231.

21. Feeding the World in the 21st Century: Grand Challenges in the Nitrogen Cycle. *NSF-INFEWS* **2015**. 1-37.

22. Mansuy, D., Rouer, E., Bacot, C., Gans, P., Chottard, J. C., and Leroux, J. P. *Biochem. Pharmacol.* **1978**, *27*, 1229-1237.

23. Bensoussan, C., Delaforge, M., and Mansuy, D. *Biochem. Pharmacol.* **1995**, *49*, 591-602.

24. Yi, J., Ye, G., Thomas, L. M., and Richter-Addo, G. B. *Chem. Commun.* **2013**, *49*, 11179-11181.

25. Kim, C.-H. and Hollocher, T. C. *J. Biol. Chem.* **1984**, *259*, 2092-2099.

26. Wade, R. S. and Castro, C. E. *Chem. Res. Toxicol.* **1990**, *3*, 289-291.

27. Hrabie, J. A. and Keefer, L. K. *Chem. Rev.* **2002**, *102*, 1135-1154.

28. Keefer, L. K. *ACS Chem. Biol.* **2011**, *6*, 1147-1155.

29. Salmon, D. J., de Holding, C. L. T., Thomas, L., Peterson, K. V., Goodman, G. P., Saayedra, J. E., Srinivasan, A., Davies, K. M., Keefer, L. K., and Miranda, K. M. *Inorg. Chem.* **2011**, *50*, 3262-3270.

30. Dutton, A. S., Suhrada, C. P., Miranda, K. M., Wink, D. A., Fukuto, J. M., and Houk, K. N. *Inorg. Chem.* **2006**, *45*, 2448-2456.

31. Xu, N., Christian, J. H., Dalal, N. S., Abucayon, E. G., Lingafelt, C., Powell, D. R., and Richter-Addo, G. B. *Dalton Trans.* **2015**, *44*, 20121-20130.

32. Schneider, J. L., Halfen, J. A., Young, V. G., and Tolman, W. B. *New J. Chem.* **1998**, *22*, 459-466.

33. Salmon, D. J., de Holding, C. L. T., Thomas, L., Peterson, K. V., Goodman, G. P., Saayedra, J. E., Srinivasan, A., Davies, K. M., Keefer, L. K., and Miranda, K. M. *Inorg. Chem.* **2011**, *50*, 3262-3270.

34. Dutton, A. S., Suhrada, C. P., Miranda, K. M., Wink, D. A., Fukuto, J. M., and Houk, K. N. *Inorg. Chem.* **2006**, *45*, 2448-2456.

35. Hassanin, H. A., Hannibal, L., Jacobsen, D. W., El-Shahat, M. F., Hamza, M. S. A., and Brasch, N. E. *Angew. Chem. Int. Ed.* **2009**, *48*, 8909-8913.

36. Shiino, M., Watanabe, Y., and Umezawa, K. *Bioorg. Med. Chem.* **2001**, *9*, 1233-1240.

37. Ellison, M. K., Schulz, C. E., and Scheidt, W. R. *J. Am. Chem. Soc.* **2002**, *124*, 13833-13841.

38. Lee, J., Chen, L., West, A. H., and Richter-Addo, G. B. *Chem. Rev.* **2002**, *102*, 1019-1065.

39. Murayama, M. *J. Biol. Chem.* **1960**, *235*, 1024-1028.

Chapter 2: Six-coordinate Ferric Porphyrins Containing Bidentate *N*-*t*-Butyl-*N*-nitrosohydroxylaminato (NONOate) Ligands: Structure, Magnetism, IR spectroelectrochemisty, and Biologically Relevant Reactivity*

2.1 Introduction

As I mentioned in Chapter 1, NO is biosynthesized in humans and is responsible for initiating the control of normal blood pressure. Consequently, in clinical cases where the extent of NO biosynthesis is insufficient to maintain normal blood pressure, external sources of NO have been used to relieve high blood pressure. Several "NO donors" are being examined by numerous researchers, and one of the more attractive NO precursors contains the NONOate (diazeniumdiolate) functional group. This functional group formally contains two NO moieties linked to an organic fragment X as sketched in Figure 2.1. The most widely-known NONOates contain carbon-bound (*C*-NONOates) and nitrogen-bound (*N*-NONOates) organic fragments, although several NONOates containing *S*-bound and *O*-bound fragments are also known.[1]

*Reproduced in part from, "Six-coordinate ferric porphyrins containing bidentate *N*-*t*-butyl-*N*-nitrosohydroxylaminato ligands: structure, magnetism, IR spectroelectrochemistry, and reactivity" Xu, N., Christian, J. H., Dalal, N., Abucayon, E. G., Lingafelt, C., Powell, D., and Richter-Addo, G. B. *Dalton Trans.* **2015**, *44*, 20121-20130 with permission from The Royal Society of Chemistry. *Copyright © RSCPublishing*.

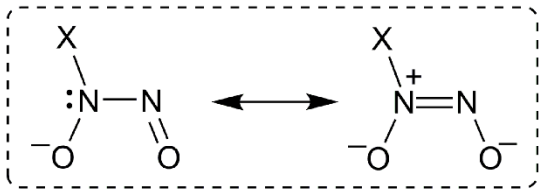

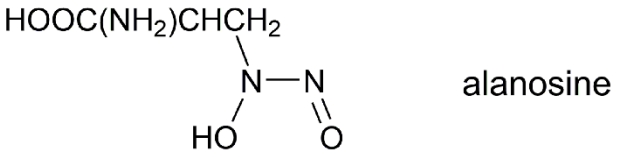

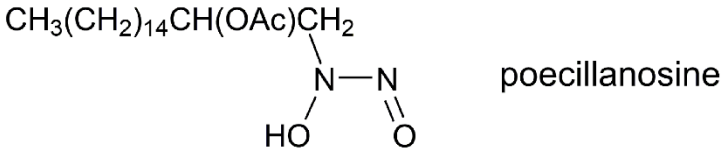

Figure 2.1. *Top*: Sketch of the NONOate functional group showing the common resonance forms. *Bottom:* Chemical structures of the NONOate-containing natural products alanosine and poecillanosine.

C-NONOates have attracted a lot of attention from the viewpoint of their coordination chemistry. For example, the Cupferron anion (*i.e.*, $[Ph\{N_2O_2\}]^-$) binds to several metal ions, and has historically been widely used as an analytical reagent for the colorimetric detection of Fe and Cu.[2] However, there is also biological interest in the chemistry of *C*-NONOate compounds due to the fact that the *C*-NONOate functional group is present in several natural products including the antitumor antibiotic alanosine isolated from *Streptomyces alanosinicus*[3,4] and the free radical scavenger poecillanosine isolated from the marine sponge *Poecillastra* spec. aff. *tenuilaminaris* (Figure 2.1),[5] and several others such as dopastin and fragin.[1] *C*-NONOates such as Cupferron and the related *N*-NONOates are frequently employed as NO donors in physiological media.[6]

NONOates bind to metals in coordination compounds almost exclusively via the bidentate *O,O*-binding mode.[2] The only structurally characterized exception of an observed monodentate *O*-binding mode is that of a Cu complex containing the ($[Et_2N\{N_2O_2\}]^-$) ligand.[7]

Given the biological importance of *C*-NONOates, I became interested in determining what kind of interactions would be present if *C*-NONOates encountered heme in biology. Cupferron has been reported to be a good substrate for horseradish peroxidase (releasing PhNO and NO),[8] and a direct binding of an *N*-NONOate to the metal center of cobalamin has been suggested to precede the release of NO.[9] Interestingly, a related direct binding of the natural product dopastin via its NONOate functional group to the di-Cu active site of mushroom tyrosinase has been proposed to precede the observed inhibition of this enzyme.[10]

To date, the mechanism of the NO release from NONOate compounds remains poorly understood due to the lack of structural and spectroscopic information related to the intermediates of the "NO release" reaction step. This chapter describes the design and execution of reactions of *C*-NONOate compounds with heme model complexes to gain a fundamental understanding on the interactions of NONOates with heme active sites and their subsequent reactions. The results and mechanistic insights presented and discussed in this chapter will help provide a molecular basis for the design of safe and selective NO donor compounds that can be administered to humans. Combined with our group's initial report on a Cupferron complex,[11] the complexes described in this work remain the only isolable NONOate adducts of heme models reported to date. In this work, I employed a combination of spectroscopy (IR, NMR, and EPR), electrochemistry, crystallography,

and variable temperature-variable field (VTVH) magnetization techniques to explore the chemistry and chemical biology of NONOates with heme active sites using synthetically derived heme-NONOate model systems.

2.2 Results and Discussion

2.2.1 Synthesis

Our research group previously reported the preparation of the *aryl* NONOate Cupferron iron porphyrin complexes (por)Fe(η^2-ON(Ph)NO) (por = TPP, T(*p*-OMe)PP) from the reactions of the (por)FeCl precursors with Ag[ON(Ph)NO].[11] I, together with another lab member (Dr. Nan Xu) designed, and utilized a more convenient route to prepare the previously unknown *alkyl* NONOate complexes (por)Fe(η^2-ON(*t*-Bu)NO) (por = OEP (**1**), TPP (**2**)) using the readily obtainable porphyrin oxo-dimer precusors and *N*-*t*-butyl-*N*-nitrosohydroxylamine as shown in eq. 2.1. The analytically pure products were obtained in 55−68% isolated yields. The solids are stable in air for short periods, but their solutions were sensitive to air as judged by IR spectroscopy. The IR spectrum of (OEP)Fe(η^2-ON(*t*-Bu)NO) **1** as a KBr pellet reveals a new strong band at 1166 cm^{-1} associated with the N_2O_2 moiety,[12,13] in addition to the porphyrin bands. For the compound (TPP)Fe(η^2-ON(*t*-Bu)NO) **2**, in addition to the new related band at 1163 cm^{-1}, a new medium intensity band at 961 cm^{-1} is observed that is in a region associated with δ(ONNO).[12,14]

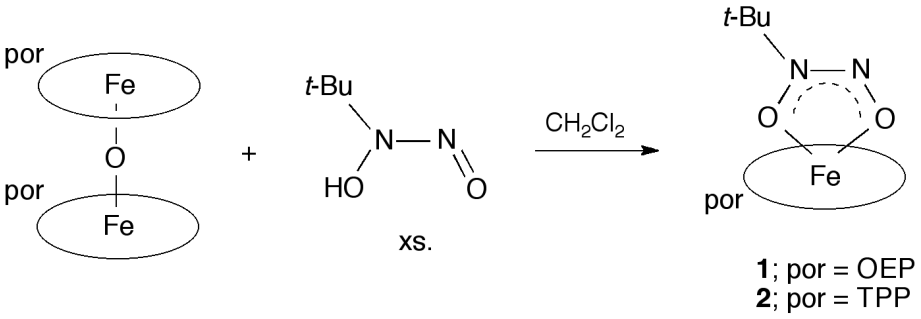

(**2.1**)

Other IR bands of the bidentate ligand were not readily discernible in the spectrum, presumably due to overlap with the porphyrin bands.

2.2.2 Molecular Structures

The crystal structures of (OEP)Fe(η^2-ON(*t*-Bu)NO) **1** and (TPP)Fe(η^2-ON(*t*-Bu)NO) **2**, the latter crystallizing as a CH_2Cl_2 solvate, are shown in Figures 2.2, and 2.3, respectively, with selected bond lengths and angles collected in Table 2.1. The most striking features of the structures are the bidendate *O,O*-binding modes of the ligand to the porphyrin Fe centers resulting in substantial apical Fe displacements (ΔFe) of +0.60 Å (for **1**) and +0.69 Å (for **2**) from their respective 24-atom porphyrin planes towards the ligands. The Fe−O bond lengths are nearly equivalent at ~2.11 Å for **1** and ~2.05 Å for **2**, with respective O−Fe−O bite angles of 68.0(3)° (with 69.9(6)° for the minor component) for compound **1** and 72.3(1)° for compound **2**.

It is interesting to note that for the OEP derivative **1**, the terminal N5−O1 bond length of 1.231(7) Å (1.232(8) Å for minor component) is significantly shorter than the N6−O2 bond length (1.340(9) Å), whereas the related N−O bond lengths in the TPP derivative are closer to each other (1.306(3) and 1.313(3) Å, respectively). The ONNO

moiety in **2** (ONNO torsion angle of 0.6(4)°) is nearly planar, compared with the wider torsion angle of 9.2(15)° (–19(3)° for the minor component) of compound **1**, although both compounds possess N6 atoms with essentially planar geometries. The N−N bond length of **1** is 1.250(8) Å, and is 1.261(4) Å in **2**.

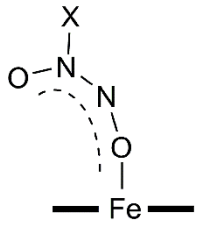

η^1 - binding
(Fe expected to be in-plane)

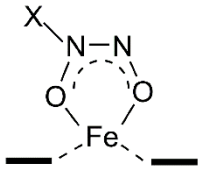

η^2 - binding
(Fe expected to be out-of-plane;
displaced toward the NONOate ligand)

The η^2-*O,O* binding mode of the axial ligands in **1**, **2**, and (T(*p*-OME)PP)Fe(η^2-ON(Ph)NO) **4** is extremely rare.[15,16] Based on the steric limitations imposed by the planar porphyrin macrocycle, it was expected that the NONOate ligand would bind in a monodentate fashion; the bidentate (η^2) mode was not expected to be the stable preferred form. In fact, there are only three other iron porphyrin complexes that display this η^2-*O,O* binding mode, namely the high-spin ferric nitrato complexes (TPP)Fe(NO_3)[17] and (TpivPP)Fe(NO_3),[18,19] and the ferric tropolonate complex (OEP)Fe($O_2C_7H_5$),[20] reported by our group (Table 2.2). The X-ray crystal structural data for **1** and **2** are indicative of these ferric complexes having high-spin centers, using the stereochemical/spin-state relationships described by Scheidt and Reed.[21] To probe possible changes in spin-states and associated spin-crossover[22,23] temperatures of the complexes **1** and **2**, I embarked (with our collaborators) on detailed variable-temperature magnetic studies of these complexes.

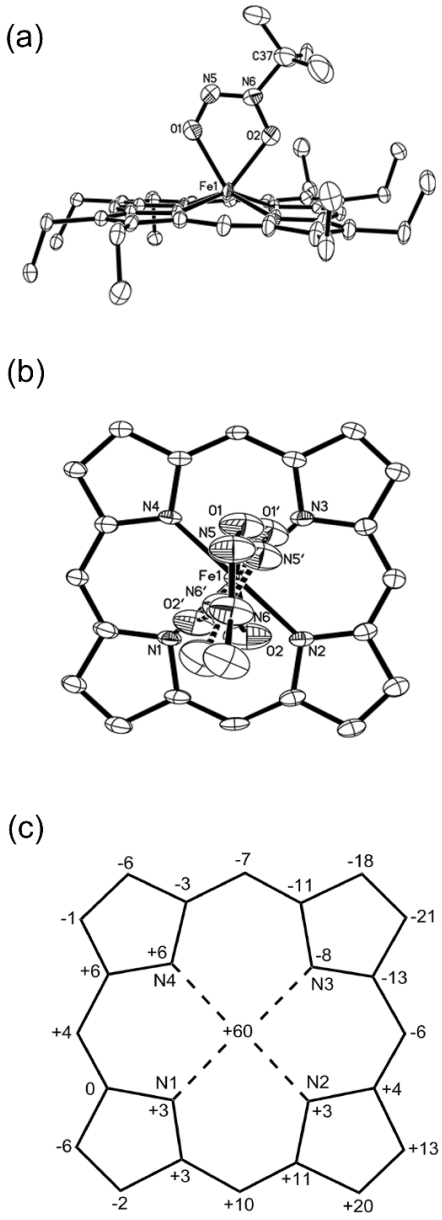

Figure 2.2. (a) Molecular structure of (OEP)Fe(η^2-ON(*t*-Bu)NO) (**1**). H atoms have been omitted for clarity, and only the major disordered ligand (67% occupancy) orientation is shown, with thermal ellipsoids drawn at 35%. (b) View of the disordered bidentate ligand orientations relative to the porphyrin core atoms, with the ligand facing the viewer and the minor disordered component represented by dashed lines. The peripheral por and *t*-Bu substituents have been omitted for clarity. (c) Perpendicular atom displacements (in units of 0.01 Å) of the porphyrin core atoms from the 24-atom mean porphyrin plane.

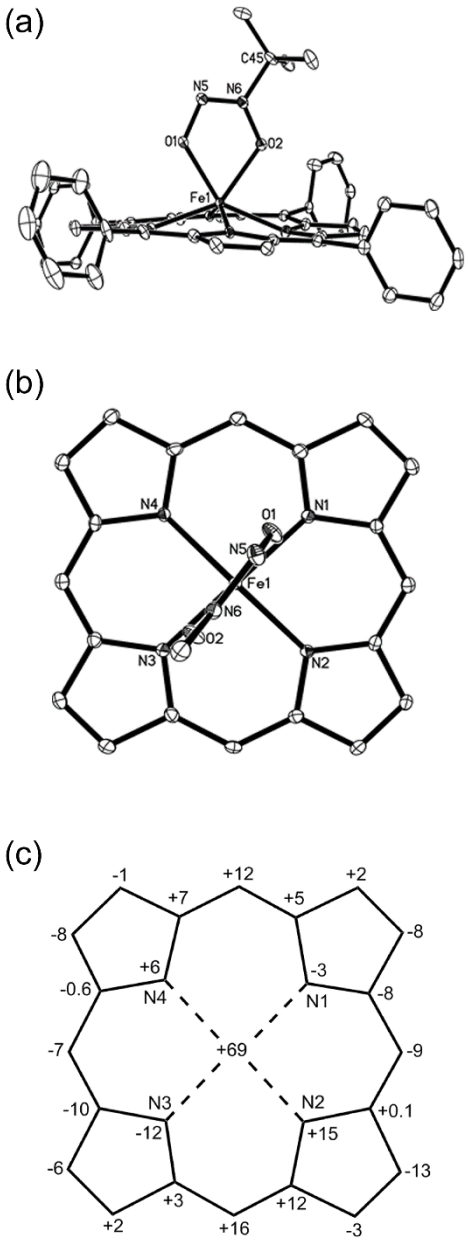

Figure 2.3. (a) Molecular structure of (TPP)Fe(η^2-ON(*t*-Bu)NO) (**2**). H atoms have been omitted for clarity. Thermal ellipsoids are drawn at 35%. (b) View of the bidentate ligand orientation relative to the porphyrin core atoms, with the ligand facing the viewer. The peripheral por and *t*-Bu substituents have been omitted for clarity. (c) Perpendicular atom displacements (in units of 0.01 Å) of the porphyrin core atoms from the 24-atom mean porphyrin plane.

Table 2.1. Selected bond lengths (Å), bond angles (°) for **1** and **2**•(CH_2Cl_2).

	1	**2**•(CH_2Cl_2)
Fe−O1	2.114(5)	2.051(3)
	[2.113(6)][a]	
Fe−O2	2.112(6)	2.051(3)
	[2.113(6)][a]	
O1−N5	1.230(8)	1.306(4)
	[1.231(8)][a]	
O2−N6	1.328(9)	1.312(4)
	[1.329(9)][a]	
N5−N6	1.264(9)	1.260(5)
	[1.264(9)][a]	
N6−C(CMe_3)	1.526(9)	1.496(5)
Fe−N1	2.103(4)	2.141(3)
Fe−N2	2.084(4)	2.085(3)
Fe−N3	2.094(4)	2.148(3)
Fe−N4	2.074(4)	2.086(3)
∠O2−Fe−O1	67.9(3)	72.26(11)
	[69.8(7)][a]	
∠N5−O1−Fe	122.4(8)	120.1(2)
	[121.5(17)][a]	
∠N6−O2−Fe	114.7(5)	115.0(2)
	[111.7(8)][a]	
∠N6−N5−O1	112.6(11)	111.7(3)
	[112(2)][a]	
∠N5−N6−O2	117.7(8)	120.9(3)
	[120.8(14)][a]	
∠N5−N6−C(CMe_3)	125.5(7)	121.3(3)
	[127.7(13)][a]	
∠O2−N6−C(CMe_3)	115.6(6)	117.7(3)
	[110.8(9)][a]	

[a] The data in brackets are for the disordered (second) component.

Table 2.2. Structural data for η^2-*O,O* liganded iron(III) porphyrins.

	Fe−O (Å)	O−Fe−O (°)	ΔFe (Å)[b]	Ref.
1[a]	2.113(6) 2.118(5)	68.0(3)	0.60	tw
2	2.051(2) 2.050(2)	72.31(9)	0.69	tw
4	2.044(3) 2.091(2)	71.52(9)	0.69	11
(TPP)Fe(NO_3)	2.019(4) 2.323(8)	51.6(2)	0.60	17
(TpivPP)Fe(NO_3)	2.123(3) 2.226(3)	57.75(10	0.61	18, 19
(OEP)Fe($O_2C_7H_5$)	2.064(6) 2.067(6)	73.1(2)	0.80	20

[a] For the major disordered component. [b] Apical displacement from the 24-atom porphyrin planes. tw = this work

2.2.3 Magnetic Behavior

Magnetic susceptibility (χ) measurements were undertaken to establish the electronic spins of **1** (por = OEP) and **2** (por = TPP). The magnetic moments of **1** and **2** were found to be 5.976 μ_B and 5.974 μ_B, respectively, at room temperature, that is, close to the spin-only value for an $S = {}^5/_2$ system (5.916 μ_B for $g = 2$). The magnetic moments of both compounds remain nearly constant down to 20 K, but decrease sharply below 20 K, as shown in Figure 2.4. The sharp decrease in μ_{eff} suggested that both compounds have significant zero-field splitting (zfs) resulting from spin-spin and spin-orbit coupling, as expected for an S = $^5/_2$ state in a noncubic environment.[24]

The data in Figure 2.4 were well simulated using the parameters $S = {}^5/_2$, $D = 4.3 \pm 0.2$ cm^{-1}, and $g_{avg} = 2.02 \pm 0.01$. Further confirmation of these parameters was achieved by variable temperature/variable field (VTVH) magnetization measurements (1.8–300 K). The VTVH data for both compounds are shown in the inset of Figure 2.4. These data were well simulated using $S = {}^5/_2$, $g_{avg} = 2.02 \pm 0.01$, and $D = 3.6 \pm 0.2$ cm^{-1}, which is in

good agreement with the susceptibility results. In both compounds the magnetic data are consistent with the assignment of an $S = {}^5/_2$ high-spin (HS) ferric (Fe^{3+}) ion. Since magnetization and magnetic susceptibility are not the most accurate methods for determining D or g, a detailed EPR study was undertaken.

Figure 2.5 shows the room temperature, X-band (9.4 GHz) powder EPR spectra of both compounds (middle segment, blue (compound **1**) and black (compound **2**)). Also shown are the simulated energy level diagrams with the magnetic field orientation parallel to the principal symmetry axis of the molecule (H || z) and parallel to the x, y directions (top and bottom segments, respectively). The simulated energy level diagrams and EPR spectra were calculated using a locally developed computer program,[25,26] which diagonalizes the Hamiltonian matrix of eq. 2.6.

At X-band (9.4 GHz), two distinct features were seen, at $g' = 7.60$ and $g' = 4.15$. Computer simulations of the X-band spectra (middle segment, red trace), using the parameters: $S = {}^5/_2$, $g_z = 2.03 \pm 0.03$, $g_{x,y} = 1.97 \pm 0.03$, $|D| = 3.89\ cm^{-1} \pm 0.09$, and $E/D = 0.07 \pm 0.01$, are in good agreement with the experimental spectra with minor artifacts due to an imperfectly random distribution of crystallites in the used powder sample, not an uncommon feature in powder EPR studies. The EPR peaks are rather broad, thus suggesting g-anisotropy due to the electrostatic field from neighboring porphyrin molecules. Similarly broadened spectra have been previously reported for ferric nitrato porphyrinates.[19] A small, sharp peak was observed at $g = 2.02$, which is tentatively ascribed to a minor $S = ½$ impurity or decomposed product.

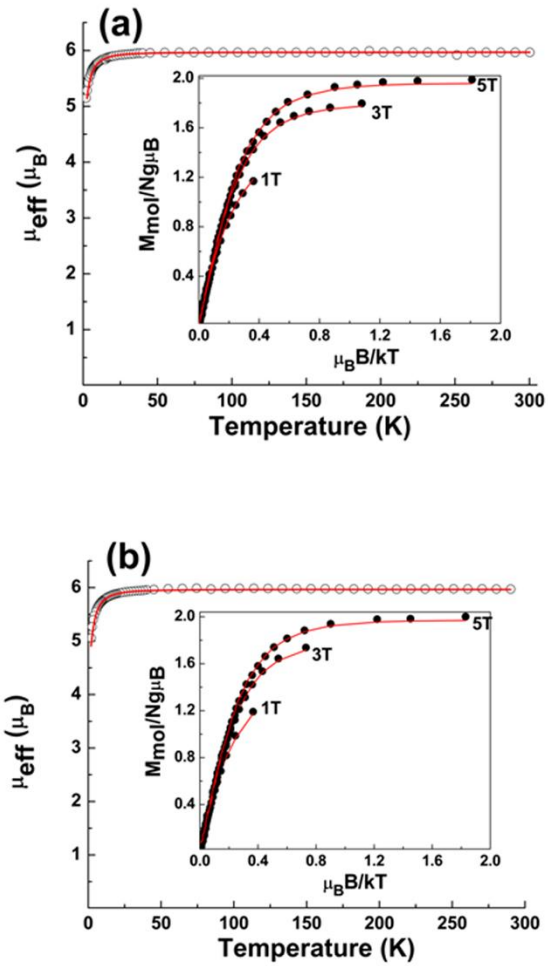

Figure 2.4. Temperature dependence of μ_{eff} (main figure) and VTVH measurements (inset) for compounds **1** and **2** labeled (a) and (b), respectively. The solid lines represent the best fit simulations to the experimental data using $S = {}^{5}/_{2}$, $g_{avg} = 2.02 \pm 0.01$, and $D = 4.3 \pm 0.2$ cm^{-1}for μ_{eff}; and $S = {}^{5}/_{2}$, $g_{avg} = 2.02 \pm 0.01$, and $D = 3.6 \pm 0.2$ cm^{-1} for VTVH measurements.

The X-band EPR analysis was confirmed by additional measurements at Q-band (34.5 GHz), a four-fold higher microwave frequency. The improved resolution provided by Q-band (34.5 GHz) splits the spectra into three peaks at $g^{'}$ = 7.59, 5.58, and 4.15 as shown in Figure 2.5 (middle segment).

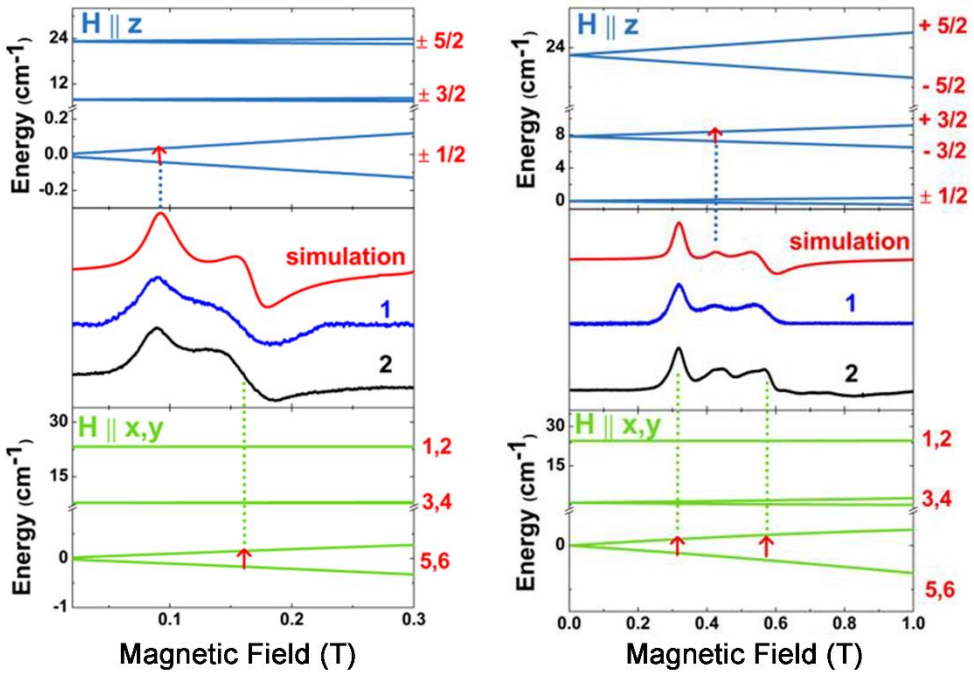

Figure 2.5. (*Left*) X-band (9.4 GHz) EPR experimental and simulation spectra of **1** (por = OEP) and **2** (por = TPP) at room temperature. (*Right*) Q-band (34.5 GHz) EPR experimental and simulation spectra of **1** and **2**. The top and bottom portions in each figure show the energy level diagrams, for the H || z and H || x, y directions respectively. The red numbers in the top figure represent the M_s quantum numbers in the high-field limit. In the bottom figure; however, they are just a label for an energy level since the field strength was not enough to be in the 'high-field' limit. Red arrows mark the EPR transition assignment.

The Q-band spectra were well fit using the same parameters as the X-band data. At both frequencies we label the *g* values with prime symbols indicating that they are only effective values, which are skewed from the usual high-spin Fe^{3+} values (*g* ~2.002–2.009),[27-30] due to large zfs, a result that has been seen in many high-spin Fe^{3+} systems.[27-30] For example, the report of large g-values has been seen in biological systems with high spin ferric ions like the heme proteins[28-32] and in other Fe^{3+} porphyrinates where the effective *g* values have been shown to range from ~7.7 to 1.8.[30] The EPR data, combined

with magnetic susceptibility, unambiguously show that the iron centers in these compounds exist as high-spin ferric ions, with large axial and non-vanishing rhombic zfs.

2.2.4 Redox Behavior and IR Spectroelectrochemistry

The redox behaviors of compounds **1** (por = OEP) and **2** (por = TPP) in CH_2Cl_2 were investigated by cyclic voltammetry and infrared spectroelectrochemistry. The cyclic voltammagrams are shown in Figure 2.6. Both compounds **1** and **2** show well-defined first reversible oxidations. The OEP derivative **1** is oxidized at an $E^{o'}$ potential of +0.27 V versus the Fc/Fc^+ couple, lower than that of the TPP analog that displays its redox couple at +0.44 V. The difference in the magnitude of redox couples is reflective of the influence of the electron-donating capacity of the macrocycles (OEP > TPP),[33] suggestive of electrooxidations at the site in close proximity to or on the porphyrin macrocycles (*vide infra*).

The OEP derivative **1** displays an irreversible reduction with E_{pc} at −1.60 V and an associated small return peak at −0.99 V. In contrast, the TPP analogue **2** exhibits a reversible reduction couple with $E^{\circ'}$ at −1.26 V. The peak separation of this reduction couple (0.33 V) is larger than that of the Fc/Fc^+ couple (0.14 V) under identical conditions, indicative of a quasi-reversible reduction and/or slow electron transfer during the reduction process.

IR spectroelectrochemistry of compound **1** upon oxidation was investigated under the same experimental conditions used for the cyclic voltammetry experiments, with the applied potential held slightly above the E_{pa} for the first oxidation. The resulting difference IR spectrum is shown in Figure 2.7. Importantly, an intense new band at 1541

cm^{-1} grew in after the first oxidation; this band is in the region associated with the characteristic bands for OEP containing π-radical monocations.[34] No new band was detected in the range typical for ferric-NO moieties.[35]

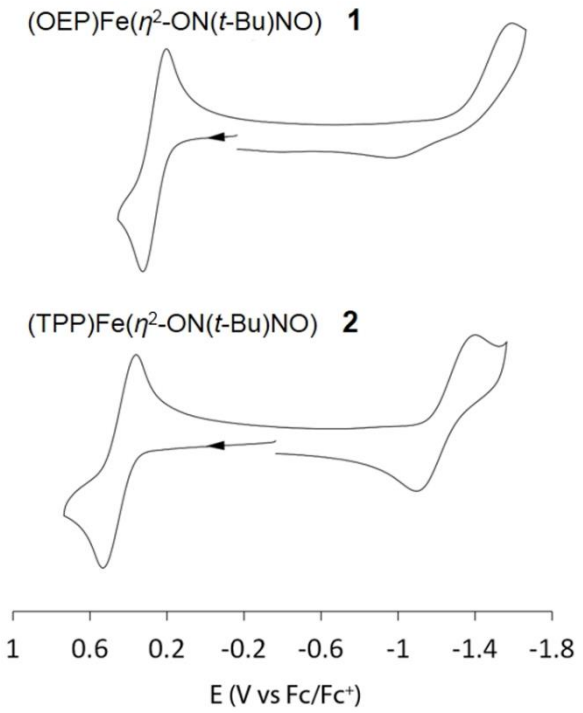

Figure 2.6. Cyclic voltammograms of the (por)Fe(η^2-ON(*t*-Bu)NO) (por = OEP, TPP) compounds in CH_2Cl_2 containing 0.1 M $[NBu_4]PF_6$ and at a scan rate of 0.2 V/s at room temperature.

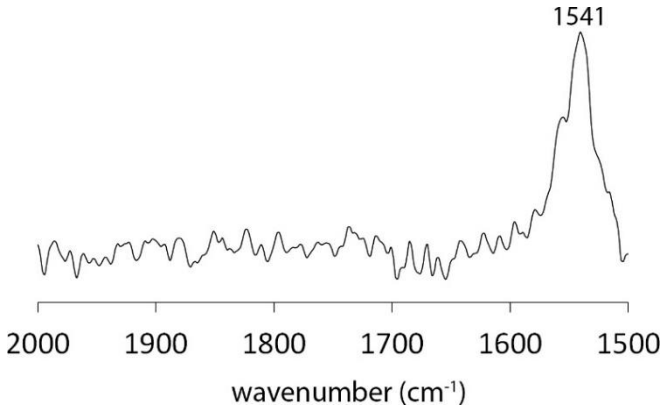

Figure 2.7. Difference FTIR spectrum showing formation of the porphyrin radical product during the first oxidation of (OEP)Fe(η^2-ON(*t*-Bu)NO).

Based on both cyclic voltammetry and spectroelectrochemistry results, I conclude that the bound diazeniumdiolate ligand is retained upon oxidation, and that the oxidation occurs on the macrocycle and not on the axial metal-ligand fragment (eq. 2.2).

$$(\text{por})\text{Fe}(\eta^2\text{-ON}(t\text{-Bu})\text{NO}) \rightarrow (\text{por}^{\bullet+})\text{Fe}(\eta^2\text{-ON}(t\text{-Bu})\text{NO}) + e^- \quad (\mathbf{2.2})$$

The difference IR spectrum obtained during spectroelectrochemical oxidation of **2** does not show any new band formed in the 2000−1500 cm^{-1} region. We note that the characteristic bands of tetraarylporphyrin radicals at 1295−1270 cm^{-1} in the IR spectra[34] are outside of the accessible IR spectral window of our instrumentation. However, chemical oxidation of (TPP)Fe(η^2-ON(*t*-Bu)NO) using $AgBF_4$ (see Experimental Section) results in a product with a new band at 1293 cm^{-1}, consistent with the generation of the ($TPP^{\bullet+}$)Fe(η^2-ON(*t*-Bu)NO) radical cation product as described in eq. 2.2.

2.2.5 Biologically Relevant Reactivity

The final products obtained when (OEP)Fe(η^2-ON(*t*-Bu)NO) was reacted with 1-MeIm were not the expected six-coordinate compounds shown in eq. 2.3, but rather the known nitrosyl compound (OEP)Fe(NO) (ν_{NO} = 1665 cm^{-1}) and the organic *t*-BuNO product (eq. 2.4), the latter characterized by ^1H NMR spectroscopy. No stable six-coordinate product was obtained in this case.

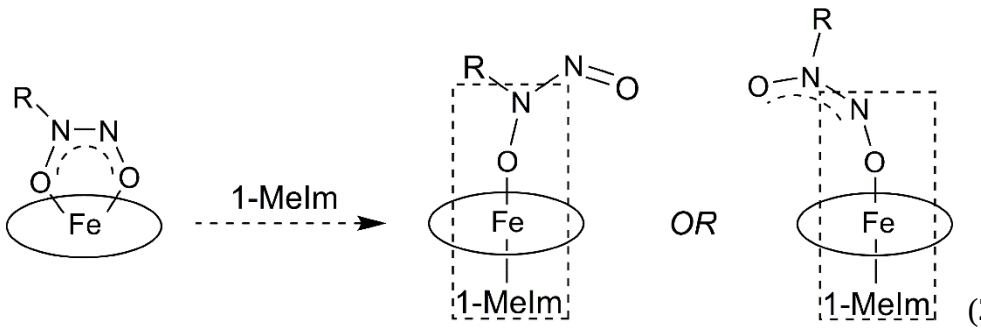

(**2.3**)

We propose that the reaction of eq. 2.3 results in the elimination of both NO and *t*-BuNO, with NO being the only reagent capable of re-binding to Fe, as the *t*-BuNO ligand is likely too bulky to re-bind effectively with the Fe porphyrin.

$$(\text{OEP})\text{Fe}(\eta^2\text{-ON}(t\text{-Bu})\text{NO}) + \text{1-MeIm} \rightarrow (\text{OEP})\text{Fe}(\text{NO}) + t\text{-BuNO} + \text{other products} \quad (\mathbf{2.4})$$

Indeed, to examine this proposed reaction pathway further, we prepared the related Cupferron analog (OEP)Fe(η^2-ON(Ph)NO) **3** and performed a similar reaction with 1-MeIm (eq. 2.5). In this case, I was successful at isolating both the known five-coordinate (OEP)Fe(NO) compound and the six-coordinate derivative (OEP)Fe(PhNO)(1-MeIm) that were identified by IR spectroscopy and X-ray crystallography (eq. 2.5).[36] The analogous reaction of (T(*p*-OMe)PP)Fe(η^2-ON(Ph)NO) (**4**) with 1-MeIm generated the nitrosyl compound (T(*p*-OMe)PP)Fe(NO) and the new six-coordinate (T(*p*-OMe)PP)Fe(PhNO)(1-MeIm) (**6**) derivative that were characterized by IR spectroscopy and X-ray crystallography (Fig. 2.8).

$$(\text{OEP})\text{Fe}(\eta^2\text{-ON(Ph)NO}) + \text{1-MeIm} \rightarrow (\text{OEP})\text{Fe}(\text{PhNO})(\text{1-MeIm}) + (\text{OEP})\text{Fe}(\text{NO}) \quad (\mathbf{2.5})$$

The C−N−O plane of the PhNO ligand of (T(*p*-OMe)PP)Fe(PhNO)(1-MeIm) bisects adjacent porphyrin N-atoms, and the axial ligands are essentially mutually perpendicular. Similar axial ligand orientations have been observed previously for (OEP)Fe(*i*-PrNO)(py),[37] (por)Fe(*i*-PrNO)(1-MeIm) (por = TPP, TTP),[37] and (TPP)Fe(PhNO)$_2$,[38] although parallel (or near-parallel) orientations are present in the crystal structures of (OEP)Fe(*i*-PrNO)(1-MeIm),[37] and related complexes.[36]

Based on the products formed from the reactions of the NONOate compounds with 1-MeIm (top of Scheme 2.1; path A), I propose that the initial binding of 1-MeIm *trans* to the NONOate group would likely need to be coincident with a bidentate-to-monodentate binding shift of the NONOate group, analogous to the expected products of eq. 2.3. Surprisingly, there is only a single structural precedent for such a monodentate NONOate binding (in a Cu complex).[7] Decomposition of this (por)Fe(1-MeIm)(η^1-ON(R)NO) intermediate then results in the release of RNO and Fe-bound NO. I note that the (por)Fe(RNO)(1-MeIm) and (por)Fe(NO) products were obtained in relatively low yields (~50% total isolated yield based on Fe), and I was not successful in identifying the other products of the reaction, hence this proposed path for the reaction with 1-MeIm does not necessarily represent the complete picture for this reaction pathway.

I also explored the possible adduct formation between the (por)Fe(η^2-ON(*t*-Bu)NO) compounds and NO in an attempt to generate the six-coordinate (por)Fe(NO)(η^1-ON(*t*-Bu)NO) products. Addition of NO (or ^{15}NO) to **1** in CH_2Cl_2 yielded a product with a ν_{NO} band at 1883 cm^{-1} ($\nu_{^{15}NO}$ = 1848 cm^{-1}) assigned to the desired nitrosyl (OEP)Fe(NO)(η^1-ON(*t*-Bu)NO) product (Scheme 2.1; path B). The related nitrosyl (TPP)Fe(NO)(η^1-ON(*t*-Bu)NO) product displayed ν_{NO} at 1888 cm^{-1} ($\nu_{^{15}NO}$ = 1851 cm^{-1}).

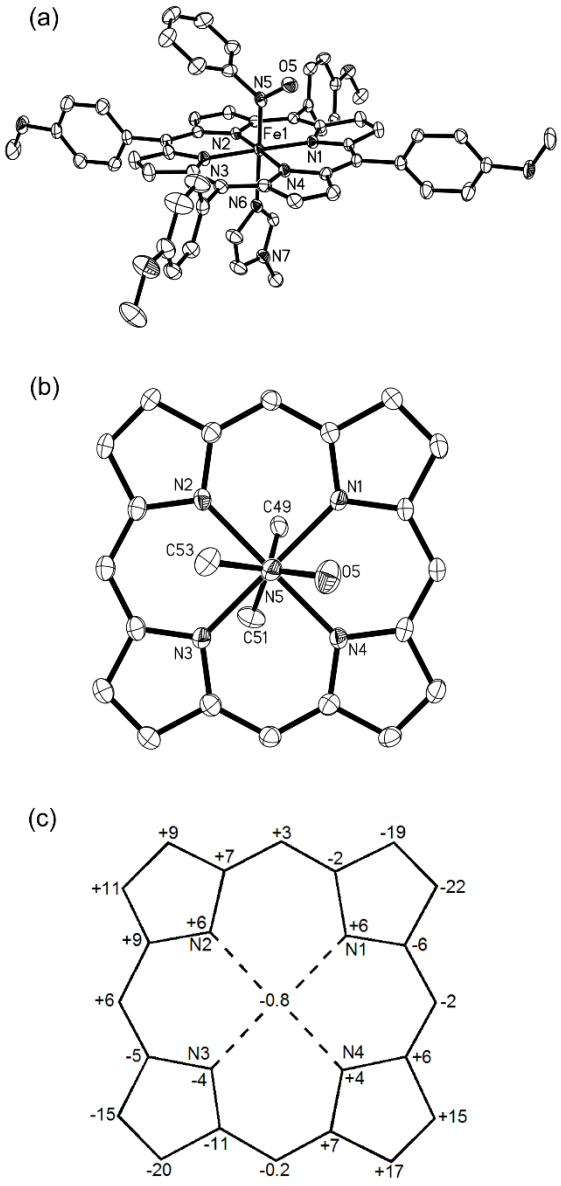

Figure 2.8. (a) Molecular structure of (T(*p*-OMe)PP)Fe(PhNO)(1-MeIm) (**6**). H atoms have been omitted for clarity. Thermal ellipsoids are drawn at 50%. (b) Top view of the relative axial ligand orientations. Only the core axial ligand atoms are shown for clarity. (c) Perpendicular atom displacements (in units of 0.01 Å) of the porphyrin core atoms from the 24-atom mean porphyrin plane. Selected bond lengths and angles: Fe1–N5 = 1.795(2) Å, Fe1–N6 = 2.044(2) Å, Fe1–N5–O5 = 123.4(2)°, N5–Fe1–N6 = 178.8(1)°, N4–Fe1–N5–O5 = 38.1(2)°.

Although there are no isolable (por)Fe(NO)(alkoxide) compounds reported in the literature, the ν_{NO} of (TPP)Fe(NO)(η^1-ON(*t*-Bu)NO) at 1888 cm^{-1} is lower than the ν_{NO} of the neutral nitrosyl trifluroacetate compound (TPP)Fe(NO)(OC(=O)CF_3) at 1907 cm^{-1}.[39] Unfortunately, all attempts to isolate the (por)Fe(NO)(η^1-ON(*t*-Bu)NO) products from solution resulted in their decomposition to the known five-coordinate (por)Fe(NO) derivatives.

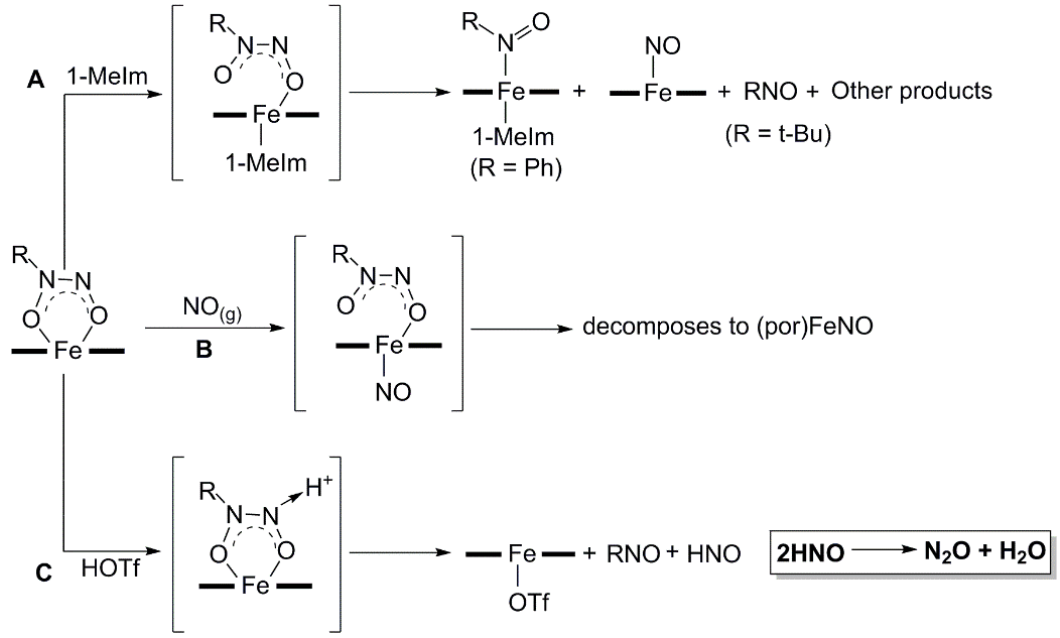

Scheme 2.1. Proposed reaction pathways of (por)Fe(η^2-ON(R)NO). (A) Reaction with 1-MeIm, (B) Reaction with NO, (C) Protonation reaction with triflic acid (HOTf).

Another important biologically-relevant reaction that I examined was the protonation of the (por)Fe(η^2-ON(R)NO) complexes. Similar to the reactions with 1-MeIm described above, these protonation reactions were performed under reduced laboratory lighting to minimize the light-induced decomposition of the starting (por)Fe(η^2-ON(R)NO) compounds. Reaction of (OEP)Fe(η^2-ON(*t*-Bu)NO) (**1**) with

anhydrous triflic acid generated the known (OEP)Fe(OTf) that was characterized by X-ray crystallography, with *t*-BuNO as the organic product that was identified by ^{1}H NMR spectroscopy (path C in Scheme 2.1). Interestingly, gas-phase IR spectroscopic analysis of the collected headspace gases revealed the formation of N_2O. The analogous protonation reaction with the Cupferron complex (T(*p*-OMe)PP)Fe(η^2-ON(Ph)NO) (**4**) likewise yielded N_2O gas as a product. Based on these results, we propose that protonation likely occurs at the "exposed" N5 atoms, as both O-atoms of the NONOate group are involved in binding to the ferric center in the (por)Fe(η^2-ON(R)NO) complexes (*i.e.*, first product of pathway C in Scheme 2.1). Similar *N*-protonations have been considered in the pH-dependent decompositions of NONOates to help explain the release of HNO in these systems.[40,41] This protonated [(por)Fe(η^2-ON(R)N(H)O)]$^+$ intermediate would then release both RNO and HNO, the latter decomposing according to its known dimerization[42,43] to the observed N_2O gas.

2.3 Summary and Conclusions

This study demonstrates that the alkyl NONOate derivatives **1** and **2** are isolable and characterizable by X-ray structural, spectroelectrochemical, and magnetic measurements. These species may thus be more stable than previously thought. The detailed magnetic studies showing high-spin ($S = {}^5/_2$) formulations for these ferric compounds are consistent with the significant apical displacements of the Fe centers towards the axial *O,O*-bidentate ligands. Although **1** and **2** are thermodynamically stable, they are reactive towards a histidine mimic (1-MeIm),

NO, and protons, providing additional insight into *C*-NONOate decomposition pathways in the presence of metal active sites.

This work provides the first systematic study of the interactions of heme active sites and NONOates using synthetically derived heme models. The results generated shed light on the fate of the corresponding carcinogenic RNO fragment of NONOate after the release of NO which is significant in the field of drug design.

2.4 Experimental Section

The reactions were performed anaerobically using nitrogen as the inert gas. Standard Schlenk glassware and an inert atmosphere glove box were utilized for the syntheses. Solvents were distilled under nitrogen from appropriate drying agents or collected under nitrogen from a Pure Solv 400-5-MD Solvent Purification System (Innovative Technology).

2.4.1 Chemicals

The free base porphyrin (TPP)H_2[44] was synthesized by literature procedure, and the related (OEP)H_2 was purchased from Mid-century Chemicals and used as received. The metalloporphyrins (por)FeCl (por = TPP, OEP)[45] were prepared according to their published procedures. The μ-oxo dimers [(por)Fe]$_2$O (por = TPP, OEP)[46-48] were prepared from their respective (por)FeCl precursors following published procedures. The compounds trifluoromethanesulfonic acid (CF_3SO_3H), ferrocene (Fc, 98%), tetrabutylammonium hexafluorophosphate ([NBu_4]PF_6, ≥ 99%), and 1-methylimidazole (1-MeIm, ≥99%) were purchased from Sigma-Aldrich and were used as received. *N-t-*

butyl-*N*-nitrosohydroxylamine (HON(*t*-Bu)NO) was prepared by literature methods.[49] The Cupferron salt Ag[ON(Ph)NO] was prepared as described previously.[50] Chloroform-*d* ($CDCl_3$, 99.96 %D) was purchased from Cambridge Isotopes, deaerated by three freeze-pump-thaw cycles, and stored over molecular sieves. Natural abundance nitric oxide (NO) gas was passed through a KOH column and through a cold trap prior to its contact with the precursor solution to avoid the introduction of NO_x impurities. Labeled ^{15}NO (Icon Isotope Inc., 99% ^{15}N) was used as received without further purification.

2.4.2 Instrumentation/Spectroscopy

Infrared (IR) spectra for compound characterization were recorded on a Bruker Tensor 27 FTIR spectrometer equipped with mid-IR fiber optic probe and liquid N_2 cooled MCT detector. ^1H NMR spectra were collected on a 400 MHz Varian NMR spectrometer at 25°C using $CDCl_3$ as a solvent (referenced at 7.26 ppm). Electrochemical experiments were performed using a BAS CV 50W instrument. X-ray diffraction experiments were conducted by Dr. Douglas R. Powell on a diffractometer equipped with a Bruker APEX ccd area detector [51,52] using graphite-monochromated Mo Kα radiation (λ = 0.71073 Å). EPR spectra were recorded on a Bruker E500 spectrometer equipped with X- and Q-band microwave sources (9.4 and 34.5 GHz, respectively) at Florida State University. Magnetic behavior of the heme-model complexes were studied using a Quantum Design MPMS-XL-5 SQUID magnetometer at Florida State University. Elemental analyses were performed by Atlantic Microlab, Inc., Norcross, GA.

2.4.3 Syntheses

The following reactions are representative for the preparation of (por)Fe(η^2-ON(R)NO) (por = OEP, TPP, T(*p*-OMe)PP; R = *t*-Bu, Ph).

Preparation of (OEP)Fe(η^2-ON(*t*-Bu)NO) (1). To a CH_2Cl_2 (10 mL) solution of [(OEP)Fe]$_2$(μ-O) (25 mg, 0.021 mmol) under an atmosphere of nitrogen was added a CH_2Cl_2 solution (2.5 mL) of excess *N*-*t*-butyl-*N*-nitrosohydroxylamine (68 mg, 0.58 mmol, ~28x excess). The solution was stirred for 1 h during which time the color changed gradually from brown to purple-red. The solvent was removed under vacuum. Hexane (~5 mL) was added to the residue, and the mixture stirred for ~ 1 min and left to stand for 5-10 min. The light red supernatant was discarded and the remaining dark purple solid dried in vacuo overnight to give (OEP)Fe(η^2-ON(*t*-Bu)NO) (**1**) (16 mg, 0.022 mmol, 55% isolated yield). Anal. Calcd for $C_{40}H_{53}N_6O_2Fe.0.055CH_2Cl_2$ (MW 710.40): C: 67.72; H, 7.53; N, 11.83; Cl, 0.55. Found: C, 67.73; H, 7.58; N, 11.73; Cl, 0.53. IR (KBr) spectroscopy revealed a new peak at 1166 cm^{-1} assigned to the [ON(*t*-Bu)NO]$^-$ ligand. X-ray quality crystals were obtained by a slow evaporation of a CH_2Cl_2/hexane (2:1) solution of the complex under nitrogen. Residual CH_2Cl_2 was present in the sample sent for elemental analysis (as judged by Cl analysis), but it was not detectable by X-ray diffraction.

Preparation of (TPP)Fe(η^2-ON(*t*-Bu)NO) (2). The tetraphenylporphyrin derivative of **1** above, namely (TPP)Fe(η^2-ON(*t*-Bu)NO) (**2**), was obtained similarly in 68% isolated yield. Anal. Calcd for $C_{48}H_{37}N_6O_2Fe.0.74CH_2Cl_2$ (MW 933.44): C, 68.99; H, 4.57; N, 9.90; Cl, 6.18. Found: C, 69.23; H, 4.86; N, 9.61; Cl, 6.25. IR (KBr): 1163 (sh) and 961 (m) cm^{-1} are assigned to the ONNO moiety of the ligand. X-ray quality crystals were

obtained by a slow evaporation of a CH_2Cl_2/cyclohexane (2:1) solution of the complex under nitrogen. Fractional CH_2Cl_2 was present in the sample sent for elemental analysis (as judged by Cl analysis), but it was present in full occupancy in the structure obtained by X-ray diffraction.

Preparation of (OEP)Fe(η^2-ON(Ph)NO) (3). The synthesis was performed under reduced laboratory lighting to minimize the light-induced decomposition of the product. To a Schlenk tube charged with (OEP)FeCl (23.1 mg, 0.04 mmol) in CH_2Cl_2 (10 mL) was added an excess of freshly prepared Ag[ON(Ph)NO] (22.3 mg, 0.09 mmol). The mixture was stirred for 15 min during which time the color changed from brown-red to bright red-orange. The solution was then filtered via cannula and the solvent removed in vacuo. The dark residue was washed with hexane and dried *in vacuo* to give (OEP)Fe(η^2-ON(Ph)NO) (**3**) (15.7 mg, 59% yield). IR (KBr): 1340 (m), 1283 (s), 940 (m) cm^{-1}, assigned to $\nu_{N=N}$, ν_{NO}, and δ_{ONNO}, respectively.

Preparation of (T(*p*-OMe)PP)Fe(η^2-ON(Ph)NO) (4).[11] The (T(*p*-OMe)PP) derivative of **3** above was obtained similarly in 63% yield (46.0 mg) from the reaction of (T(*p*-OMe)PP)FeCl (65.0 mg, 0.08 mmol) in CH_2Cl_2 (10 mL) with excess freshly prepared Ag[ON(Ph)NO)] (64.3 mg, 0.26 mmol) under reduced laboratory lighting. IR (KBr, cm^{-1}): δ_{ONNO} = 937 cm^{-1}. The IR frequencies due to N=N and N=O vibrations were not detected due to the intense porphyrin ring signals in the region where those peaks are normally expected.

2.4.4 Reactivity Studies

2.4.4.1 Reactions of the (por)Fe(η^2-ON(R)NO) Complexes (por = OEP, T(*p*-OMe)PP; R = *t*-Bu, Ph) with 1-MeIm. The following reactions performed under reduced laboratory lighting are representative.

(i) To a $CDCl_3$ (3 mL) solution of compound **1** (16 mg, 0.013 mmol) was added excess 1-MeIm (28.2 mg, 0.34 mmol). The reaction mixture was stirred at room temperature for 1 hr during which time the color gradually changed from purple to red-purple. The solvent and volatiles were transferred by vacuum to a separate flask. The remaining solid in the reaction flask was washed with hexane and dried *in vacuo* to give a mixture of the known (OEP)Fe(NO) (ν_{NO} = 1672 cm^{-1}) compound[35] and unreacted **1** as judged by IR spectroscopy. A ^1H NMR spectroscopic analysis of the trapped volatiles revealed the formation of *t*-BuNO [δ, ppm: 1.67 (s, (*t*-BuNO)$_2$ dimer) and 1.22 (s, *t*-BuNO monomer)][53] as the primary by-product of the reaction in ~50% unoptimized yield based on **1**.

(ii) To a CH_2Cl_2 (5 mL) solution of (T(*p*-OMe)PP)Fe(η^2-ON(Ph)NO) (**4**; 20.0 mg, 0.02 mmol) was added excess 1-MeIm, and the reaction mixture stirred for ~1 h at –45 °C during which time the color changed from bright red-orange to red-purple. The solvent was removed *in vacuo* and the residue was washed with hexane and the product dried *in vacuo* overnight. Crystallization of the residue from the slow evaporation of its CH_2Cl_2/hexane (1:1) solution gave a mixture (~9.0 mg) of the crystalline products (T(*p*-OMe)PP)Fe(NO) (23% yield; ν_{NO} = 1670 cm^{-1})[35] and (T(*p*-OMe)PP)Fe(PhNO)(1-MeIm) (23% yield; ν_{NO} = 1346 cm^{-1}) in a 1:1 ratio.

The corresponding reaction of (OEP)Fe(η^2-ON(Ph)NO) with excess 1-MeIm similarly gave a 1:1 mixture of (OEP)Fe(NO) (ν_{NO} = 1672 cm^{-1}) and (OEP)Fe(PhNO)-(1-MeIm) (ν_{NO} = 1337 cm^{-1})[36] as products in ~21% yield each.

2.4.4.2 Reactions of the (por)Fe(η^2-ON(*t*-Bu)NO) Complexes (por = OEP, TPP) with NO gas. Solutions of the (por)Fe(η^2-ON(*t*-Bu)NO) (por: OEP, **1**; TPP, **2**) complexes in CH_2Cl_2 (3 mL) were exposed to NO gas (via bubbling of the gas through the solutions) for 5 min during which time the color of the solutions changed from purple to bright red-purple. The unreacted NO gas in the headspace was then replaced by sparging with N_2 gas for ~5 min. The IR spectrum of the product solution from the reaction of **1** with NO in CH_2Cl_2 displayed a new strong ν_{NO} band at 1883 cm^{-1} ($\nu_{^{15}NO}$ = 1848 cm^{-1}) assigned to the six-coordinate (OEP)Fe(NO)(η^1-ON(*t*-Bu)NO). The IR spectrum of the product of the reaction of **2** with NO yielded a strong ν_{NO} band at 1888 cm^{-1} ($\nu_{^{15}NO}$ = 1851 cm^{-1}) assigned to the six-coordinate (TPP)Fe(NO)(η^1-ON(*t*-Bu)NO). Attempted crystallization of the OEP adduct led to the formation of the known five coordinate (OEP)Fe(NO) compound identified by IR spectroscopy and by X-ray crystallography.

2.4.4.3 Protonation of the (por)Fe(η^2-ON(R)NO) Complexes. The following reactions performed under reduced laboratory lighting are representative.

(i) (TPP)Fe(η^2-ON(*t*-Bu)NO) (**2**): Triflic acid (20 μL, 0.2 mmol) was added dropwise to a $CDCl_3$ (3.0 mL) solution of **2** (13.1 mg, 0.02 mmol) at room temperature. The bright red-purple solution immediately changed to an orange-black color. The reaction mixture was stirred for 1 h in a sealed Schlenk tube. The headspace gases were

then vacuum transferred into a gas IR cell. The gas phase IR spectrum revealed bands at 2237/2212 and 1276/1261 cm^{-1} assigned to ν_{as} and ν_{sym} of N_2O, respectively.[54] The remaining reaction solution was vacuum transferred to another flask for ^1H NMR spectroscopic analysis. ^1H NMR ($CDCl_3$, 25 ˚C, 400 MHz; δ, ppm): 7.26 (s, $CDCl_3$), 5.32 (s, CH_2Cl_2), 2.21 (s, acetone), 1.75 (s, H_2O), 1.59 (s, (*t*-BuNO)$_2$ dimer) and 1.27 (s, *t*-BuNO monomer),[53] 1.22 (hexane impurity), and 0.06 (s, silicone grease impurity).[55] The solid residue was dried *in vacuo* and crystallized from the slow evaporation of a CH_2Cl_2/hexane solution of this residue. The resulting crystals were identified from an X-ray structural analysis as the known five coordinate complex (TPP)Fe(OSO_2CF_3).[56]

(ii) (T(*p*-OMe)PP)Fe(η^2-ON(Ph)NO) (**4**): Triflic acid (20 μL, 0.2 mmol) was added dropwise to a CH_2Cl_2 (10.0 mL) solution of **4** (18.2 mg, 0.02 mmol) at room temperature. The bright red-purple solution immediately changed to a dark orange color. The reaction mixture was stirred for 12 h in a sealed Schenk tube, and the headspace gases were then vacuum transferred into a gas IR cell. The gas phase IR spectrum revealed the formation of N_2O.[54] The solvent was then removed from the residual mixture in the Schlenk tube under reduced pressure. Diethyl ether was added to the oily residue, and the mixture was stirred overnight and then left to stand for several minutes to allow the resulting solid particles to separate. The solvent was discarded and the solid product was dried *in vacuo*. The IR spectrum of the solid product showed a peak at 1347 (sh) cm^{-1} assigned to an Fe-bound PhNO ligand.

2.4.4.4 Chemical oxidation of (TPP)Fe(η^2-ON(*t*-Bu)NO). To a $CDCl_3$ (2.5 mL) solution of (TPP)Fe(η^2-ON(*t*-Bu)NO) (5 mg, 0.01 mmol) under reduced laboratory

lighting was added $AgBF_4$ (1.5 mg, 0.01 mmol). The reaction mixture was stirred for 15 min during which time the color of the solution changed from purple-red to a bright red. IR spectral analysis of the product solution under N_2 showed the formation of a new band at 1293 cm^{-1} indicative of a TPP-type π-radical cation product.[34]

2.4.5 Magnetic Susceptibility and EPR Measurements

2.4.5.1 Magnetic measurements. Temperature-dependent magnetic susceptibility measurements on polycrystalline samples of **1** and **2** were made using a Quantum Design MPMS-XL-5 SQUID magnetometer over a temperature range of 1.8 to 300 K at a measuring field of 0.02 T (with collaborators at Florida State University). Magnetization measurements at variable temperature and variable field (VTVH) were performed at 1, 3, and 5 T over the temperature range of 1.8 to 300 K. A diamagnetic correction of 4.585 x 10^{-4} emu/mol for **1** and 5.139 x 10^{-4} emu/mol for **2** were calculated using Pascal's constants[57] and were applied to the experimental data along with a contribution from the gelatin sample holder and straw. The magnetic properties were evaluated using the following standard spin Hamiltonian of a system with $S = {}^5/_2$ and zero-field splitting (zfs) terms, D and E.

$$\widehat{H} = \beta \vec{H} \cdot \tilde{g} \cdot \hat{S} + D\left(\hat{S}_z{}^2 - \widehat{\boldsymbol{S}}^2/3\right) + E\left(\hat{S}_x{}^2 - \hat{S}_y{}^2\right) \qquad (\mathbf{2.6})$$

In this Hamiltonian, β is the Bohr-magneton, $\vec{H}$ is the magnetic field vector, $\tilde{g}$ is the Zeeman tensor, D and E are the axial and rhombic zfs parameters, respectively, and the $\hat{S}$ terms are spin operators.[27] The nuclear hyperfine term was omitted from the

Hamiltonian because the magnetic isotope of Fe (^{57}Fe, with I = $^1/_2$) has a very small natural abundance (~ 2.1 %), thus, each peak of the EPR hyperfine doublet would account for approximately 1% of the main peaks, and would be hardly detectable, as was the case here (*vide supra*). Since magnetic susceptibility measurements are typically insensitive towards the small energy E, evaluation of both compounds began with the assumption of axial symmetry, thus E was assumed to be zero. The principal magnetic susceptibilities for a spin S = $^5/_2$ system with zfs were derived from the van Vleck equations,[58]

$$\chi_{\parallel} = \frac{N{g_{\parallel}}^2\beta^2}{k_BT}\left(\frac{1+9\exp(-2D/k_BT)+25\exp(-6D/k_BT)}{4(1+\exp(-2D/k_BT)+\exp(-6D/k_BT)}\right) \quad \textbf{(2.7)}$$

$$\chi_{\perp} = \frac{N{g_{\perp}}^2\beta^2}{k_BT}\left(\frac{9+(8k_BT/D)(1-\exp(-2D/k_BT))+(9k_BT/2D)(\exp(-2D/k_BT)-\exp(-6D/k_BT))}{4(1+\exp(-2D/k_BT)+\exp(-6D/k_BT)}\right) \quad \textbf{(2.8)}$$

The magnetic susceptibility of a randomly oriented polycrystalline powder was described using the weighted average of $\chi_{\parallel}$ and $\chi_{\perp}$: [58]

$$(\chi_{powder} = {}^1/_3\,\chi_{\parallel} + {}^2/_3\,\chi_{\perp}) \quad \textbf{(2.9)}$$

Simulation of the experimental magnetic data was performed with the *julX* program.[23] It was necessary to include a small temperature-independent paramagnetism (*TIP*) term in the simulations according to $\chi_{calc} = \chi + TIP$.

2.4.5.2 Electron paramagnetic resonance spectroscopy. Room temperature electron paramagnetic resonance (EPR) spectra were recorded on a Bruker E500 spectrometer equipped with X- and Q-band microwave sources (9.4 and 34.5 GHz, respectively; with

collaborators at Florida State University). The frequency was recorded with a built-in digital frequency counter and the magnetic field was calibrated using a 2,2-diphenyl-1-picrylhydrazyl standard (DPPH, g = 2.0036).[59] All samples were measured in quartz tubes that were sealed with approximately 1 inch of N-grease and lids. Signals from the instrument cavity and quartz tubes were measured separately and were subtracted from the spectra of our samples. The spectra were analyzed by visual comparison with a locally developed computer simulation program, as described elsewhere.[60,61]

2.4.6 Electrochemistry and Spectroelectrochemistry

Cyclic voltammograms were recorded using a BAS CV-50W Voltammetric Analyzer equipped with a three-electrode cell (3 mm Pt disk working electrode, Pt wire auxiliary electrode, and a Ag/AgCl or Ag wire quasi-reference electrode) as described previously.[62] Solutions were 1 mM in analyte and 0.1 M in $[NBu_4]PF_6$ in CH_2Cl_2. Ferrocene (Fc) was used as an internal reference standard, with potentials (V) reported relative to the Fc/Fc^+ couple.[63]

IR spectroelectrochemical measurements were recorded using a Bruker Vector 22 FT-IR spectrometer equipped with a *Remspec* mid-IR fiber-optic dip probe and a liquid nitrogen cooled MCT detector. In our adaptation of the probe for these measurements,[64] the stainless steel mirror on the liquid transmission head of the fiber-optic dip probe was replaced with a 3 mm Pt disk working electrode and equipped with a custom-made electrochemical cell including a Pt wire auxiliary electrode and a Ag/AgCl quasi-reference electrode as described previously.[62,65]

2.4.7 X-ray Crystallography

Intensity data for the crystals at 100(2) K were collected using a diffractometer with a Bruker APEX CCD area detector[51,52] using graphite-monochromated Mo Kα radiation (λ = 0.71073 Å). A summary of the crystal and refinement data are shown in Table 2.3.

(OEP)Fe(η^2-ON(*t*-Bu)NO) (1). X-ray diffraction quality crystals of (OEP)Fe(η^2-ON(*t*-Bu)NO) **1** were obtained by slow evaporation of a CH_2Cl_2/hexane (2:1) solution of **1** under nitrogen. A black plate-shaped crystal of dimensions 0.26 x 0.23 x 0.02 mm was selected for structural analysis. The intensity data were truncated to 0.89 Å because data in the higher resolution shells all had R(int)>0.25. The ligand was found to be disordered and was modeled in two orientations. The occupancies of the disordered atoms refined to 0.667(6) and 0.333(6) for the unprimed and primed atoms, respectively. Restraints on the positional and displacement parameters of the disordered atoms were required. Cell parameters were determined from a non-linear least squares fit of 4620 peaks in the range $2.26 < \theta < 25.89°$. A total of 16423 data points were measured in the range $2.35 < \theta < 23.53°$ using ω oscillation frames. The data were merged to form a set of 5538 independent data points with R(int) = 0.0589 and a coverage of 99.9%. The monoclinic space group $P2_1/c$ was determined by systematic absences and statistical tests and verified by subsequent refinement. A total of 515 parameters were refined against 295 restraints and 5538 data points to give $wR(F^2) = 0.2001$ and S = 1.011 for weights of $w = 1/[\sigma^2 (F^2) + (0.1000\ P)^2 + 8.8000\ P]$, where $P = [F_o^2 + 2F_c^2]/3$. The final R(*F*) was 0.0707 for the 3953 observed, [$F > 4\sigma(F)$], data points. The largest shift/s.u. was 0.001 in the final refinement cycle. The final difference map had maxima

and minima of 1.206 and −0.673 e/Å^3, respectively.

(TPP)Fe(η^2-ON(*t*-Bu)NO) (2). X-ray diffraction quality crystals of (TPP)Fe(η^2-ON(*t*-Bu)NO) **2** were grown from the slow evaporation of a CH_2Cl_2/cyclohexane (2:1) solution of **2** under nitrogen. A black prism-shaped crystal of dimensions 0.48 x 0.30 x 0.30 mm was selected for structural analysis. Cell parameters were determined from a non-linear least squares fit of 9070 peaks in the range $2.21 < \theta < 28.40°$. A total of 20598 data points were measured in the range $1.22 < \theta < 26.00°$ using ϕ and ω oscillation frames. The data were merged to form a set of 8306 independent data points with R(int) = 0.0410 and a coverage of 99.9%. The triclinic space group $P\bar{1}$ was determined by statistical tests and verified by subsequent refinement. A total of 544 parameters were refined against 8306 data points to give wR(F^2) = 0.2138 and S = 0.992 for weights of $w = 1/[\sigma^2(F^2) + (0.1200\ P)^2 + 7.5000\ P]$, where $P = [F_o^2 + 2F_c^2]/3$. The final R(F) was 0.0724 for the 6817 observed, [$F > 4\sigma(F)$], data points. The largest shift/s.u. was 0.001 in the final refinement cycle. The final difference map had maxima and minima of 2.150 and −1.327 e/Å^3, respectively.

(T(*p*-OMe)PP)Fe(PhNO)(1-MeIm) (6). A purple block-shaped crystal of dimensions 0.320 x 0.240 x 0.070 mm was selected for structural analysis. Cell parameters were determined from a non-linear least squares fit of 7775 peaks in the range $2.22 < \theta < 24.74°$. A total of 45452 data points were measured in the range $1.769 < \theta < 26.105°$ using ϕ and ω oscillation frames. The data were corrected for absorption by the empirical method giving minimum and maximum transmission factors of 0.897 and 0.976. The data were merged to form a set of 10179 independent data points with R(int) = 0.0494 and a coverage of 100.0%. The triclinic space group $P\bar{1}$ was determined by

statistical tests and verified by subsequent refinement. A severely disordered solvent was removed from the model using *Squeeze*.[66] A total of 640 parameters were refined against 10179 data points to give wR(F^2) = 0.1164 and S = 0.985 for weights of w = 1/[$\sigma^2(F^2)$ + (0.0550 P)^2 + 1.7000 P], where P = F_o^2 + 2F_c^2]/3. The final R(F) was 0.0435 for the 7656 observed, [$F > 4\sigma(F)$], data points. The largest shift/s.u. was 0.001 in the final refinement cycle. The final difference map had maxima and minima of 0.350 and −0.255 e/Å^3, respectively.

Table 2.3. Crystallographic collection and refinement parameters.

Complex	**1**	**2**•(CH_2Cl_2)	**6**
Empirical formula (fw)	$C_{40}H_{53}FeN_6O_2$ (705.73)	$C_{48}H_{37}FeN_6O_2$•CH_2Cl_2 (870.61)	$C_{58}H_{47}FeN_7O_5$ (977.87)
Crystal system, space group	monoclinic, $P2_1/c$	triclinic, $P\bar{1}$	triclinic, $P\bar{1}$
Unit cell dimensions			
a (Å)	18.019(5)	9.7262(15)	9.8358(13)
b (Å)	13.583(4)	13.217(2)	11.9775(16)
c (Å)	17.340(4)	17.511(3)	23.149(3)
α (°)	90	95.746(3)	81.837(2)
β (°)	118.552(7)	105.162(3)	79.205(2)
γ (°)	90	100.150(4)	74.975(2)
Volume (Å^3)	3727.9(17)	2113.2(6)	2574.7(6)
Z, Z'	4, 1	2, 1	2, 1
F(000)	1508	902	1020
Absorption coefficient (mm^{-1})	0.447	0.532	0.348
Max. and min. transmission	0.9911 and 0.8926	0.8568 and 0.7845	0.976 and 0.897
Theta range for data collection (°)	2.35 to 23.53	1.22 to 26.00	1.769 to 26.105
Reflections collected	16423	20598	45452
Independent reflections	5538 [R(int) = 0.0589]	8306 [R(int) = 0.0410]	10179[R(int) = 0.0494]
Data/restraints/parameters	5538/295/515	8306/0/544	10179/0/640
$wR(F^2$ all data) [a]	$wR2$ = 0.2001	$wR2$ = 0.2138	$wR2$ = 0.1164
$R(F$ obsd data) [b]	$R1$ = 0.0707	$R1$ = 0.0724	$R1$ = 0.0435
Goodness-of-fit on F^2	1.011	0.992	0.985
Observed data [$I > 2\sigma(I)$]	3953	6817	7656
Largest and mean shift / s.u.	0.001and 0.000	0.001 and 0.000	0.001 and 0.000
Largest diff. peak and hole (e/Å^3)	1.206 and –0.673	2.150 and –1.327	0.350 and –0.255

[a] $wR2 = \{ \Sigma [w(F_o^2 - F_c^2)^2] / \Sigma [w(F_o^2)^2] \}^{1/2}$ [b] $R1 = \Sigma ||F_o| - |F_c|| / \Sigma |F_o|$

2.5 References

1. Hrabie, J. A. and Keefer, L. K. *Chem. Rev.* **2002**, *102*, 1135-1154.

2. Mehrotra, R. C., *Hydroxamates, Cupferron and Related Ligands*, in *Comprehensive Coordination Chemistry*, G. Wilkinson, Editor. 1987, Pergamon Press: U. K. p. 505-514 (Chapter 15.9).

3. Jayaram, H. N., Tyagi, A. K., Anandaraj, S., Montgomery, J. A., Kelley, J. A., Kelley, J., Adamson, R. H., and Cooney, D. A. *Biochem. Pharmacol.* **1979**, *28*, 3551-3566.

4. Murthy, Y. K. S., Thiemann, J. E., Coronell.C, and Sensi, P. *Nature* **1966**, *211*, 1198-1199.

5. Natori, T., Kataoka, Y., Kato, S., Kawai, H., and Fusetani, N. *Tetrahedron Lett.* **1997**, *38*, 8349-8350.

6. Wang, P. G., Xian, M., Tang, X., Wu, X., Wen, Z., Cai, T., and Janczuk, A. J. *Chem. Rev.* **2002**, *102*, 1091-1134.

7. Schneider, J. L., Halfen, J. A., Young, V. G., and Tolman, W. B. *New J. Chem.* **1998**, *22*, 459-466.

8. Alston, T. A., Porter, D. J. T., and Bright, H. J. *J. Biol. Chem.* **1985**, *260*, 4069-4074.

9. Hassanin, H. A., Hannibal, L., Jacobsen, D. W., El-Shahat, M. F., Hamza, M. S. A., and Brasch, N. E. *Angew. Chem. Int. Ed.* **2009**, *48*, 8909-8913.

10. Shiino, M., Watanabe, Y., and Umezawa, K. *Bioorg. Med. Chem.* **2001**, *9*, 1233-1240.

11. Yi, G.-B., Khan, M. A., and Richter-Addo, G. B. *Inorg. Chem.* **1995**, *34*, 5703-5704.

12. Casely, I. J., Suh, Y., Ziller, J. W., and Evans, W. J. *Organometallics* **2010**, *29*, 5209-5214.

13. Keefer, L. K., Flippen-Anderson, J. L., George, C., Shanklin, A. P., Dunams, T. A., Christodoulou, D., Saavedra, J. E., Sagan, E. S., and Bohle, D. S. *Nitric Oxide: Biol. Chem.* **2001**, *5*, 377-394.

14. Deak, A., Haiduc, I., Parkanyi, L., Venter, M., and Kalman, A. *Eur. J. Inorg. Chem.* **1999**, 1593-1596.

15. Scheidt, W. R. *J. Porph. Phthalocyanines* **2008**, *12*, 979-992.

16. Scheidt, W. R., *Systematics of the Stereochemistry of Porphyrins and Metalloporphyrins*, in *The Porphyrin Handbook*, K.M. Kadish, K.M. Smith, and R. Guilard, Editors. 2000, Academic Press: New York. p. Chapter 16.

17. Phillippi, M. A., Baenziger, N., and Goff, H. M. *Inorg. Chem.* **1981**, *20*, 3904-3911.

18. Munro, O. Q. and Scheidt, W. R. *Inorg. Chem.* **1998**, *37*, 2308-2316.

19. Wyllie, G. R. A., Munro, O. Q., Schulz, C. E., and Scheidt, W. R. *Polyhedron* **2007**, *26*, 4664-4672.

20. Cheng, L., Khan, M. A., Powell, D. R., Taylor, R. W., and Richter-Addo, G. B. *Chem. Commun.* **1999**, 1941-1942.

21. Scheidt, W. R. and Reed, C. A. *Chem. Rev.* **1981**, *81*, 543-555.

22. Ikeue, T., Ohgo, Y., Ongayi, O., Vicente, M. G. H., and Nakamura, M. *Inorg. Chem.* **2003**, *42*, 5560-5571.

23. Ikeue, T., Ohgo, Y., Yamaguchi, T., Takahashi, M., Takeda, M., and Nakamura, M. *Angew. Chem. Int. Ed.* **2001**, *40*, 2617-2620.

24. Weil, J. A. and Bolton, J. R., *Electron Paramagnetic Resonance Elementary Theory and Practical Applications*. 2nd ed. 2007, Hoboken, NJ: Wiley-Interscience.

25. Krzystek, J., Zvyagin, S. A., Ozarowski, A., Trofimenko, S., and Telser, J. *J. Magn. Reson.* **2006**, *178*, 174-183.

26. Krzystek, J., Ozarowski, A., and Telser, J. *Coord. Chem. Rev.* **2006**, *250*, 2308-2324.

27. Boča, R. *Coord. Chem. Rev.* **2004**, *248*, 757-815.

28. Laguta, V. V., Glinchuk, M. D., Bykov, I. P., Maksimenko, Y. L., Rosa, J., and Jastrabik, L. *Phys. Rev. B* **1996**, *54*, 12353-12360.

29. Pontin, R. G., Slade, E. F., and Ingram, D. J. E. *J. Phys. C Solid State Phys.* **1969**, *2*, 1146-1150.

30. Priem, A., van Bentum, P. J. M., Hagen, W. R., and Reijerse, E. J. *Appl. Magn. Reson.* **2001**, *21*, 535-548.

31. Abragam, A. and Bleaney, B., *Electron Paramagnetic Resonance of Transition Ions*. 1970, Oxford: Oxford Press.

32. Pilbrow, J. R., *Transition Ion Electron Paramagnetic Resonance*. Oxford Science Publications. 1990, Oxford: Clarendon Press.

33. Kadish, K. M., Van Caemelbecke, E., and Royal, G., *Electrochemistry of Metalloporphyrins in Nonaqueous Media*, in *The Porphyrin Handbook*, K.M. Kadish, K.M. Smith, and R. Guilard, Editors. 2000, Academic Press: San Diego, CA. p. Chapter 55. Pages 1-114 (pp 11-44, and 92-93).

34. Shimomura, E. T., Phillippi, M. A., Goff, H. M., Scholz, W. F., and Reed, C. A. *J. Am. Chem. Soc.* **1981**, *103*, 6778-6780.

35. Cheng, L. and Richter-Addo, G. B., *Binding and Activation of Nitric Oxide by Metalloporphyrins and Heme*, in *The Porphyrin Handbook*, R. Guilard, K. Smith, and K.M. Kadish, Editors. 2000, Academic Press: New York. p. 219-291.

36. Godbout, N., Sanders, L. K., Salzmann, R., Havlin, R. H., Wojdelski, M., and Oldfield, E. *J. Am. Chem. Soc.* **1999**, *121*, 3829-3844.

37. Sohl, C. D., Lee, J., Alguindigue, S. S., Khan, M. A., and Richter-Addo, G. B. *J. Inorg. Biochem.* **2004**, *98*, 1238-1246.

38. Wang, L.-S., Chen, L., Khan, M. A., and Richter-Addo, G. B. *Chem. Commun.* **1996**, 323-324.

39. Xu, N., Goodrich, L. E., Lehnert, N., Powell, D. R., and Richter-Addo, G. B. *Angew. Chem. Int. Ed. Engl.* **2013**, *52*, 3896-3900.

40. Salmon, D. J., de Holding, C. L. T., Thomas, L., Peterson, K. V., Goodman, G. P., Saayedra, J. E., Srinivasan, A., Davies, K. M., Keefer, L. K., and Miranda, K. M. *Inorg. Chem.* **2011**, *50*, 3262-3270.

41. Dutton, A. S., Suhrada, C. P., Miranda, K. M., Wink, D. A., Fukuto, J. M., and Houk, K. N. *Inorg. Chem.* **2006**, *45*, 2448-2456.

42. Miranda, K. M. *Coord. Chem. Rev.* **2005**, *249*, 433-455.

43. Shafirovich, V. and Lymar, S. V. *J. Am. Chem. Soc.* **2003**, *125*, 6547-6552.

44. Adler, A. D., Longo, F. R., Finarelli, J. D., Goldmacher, J., Assour, J., and Korsakoff, L. *J. Org. Chem.* **1967**, *32*, 476.

45. Adler, A. D., Longo, F. R., Kampas, F., and Kim, J. *J. Inorg. Nucl. Chem.* **1970**, *32*, 2443-2445.

46. Fleische, E. B. and Srivastava, T. S. *J. Am. Chem. Soc.* **1969**, *91*, 2403-2405.

47. Lamar, G. N., Eaton, G. R., Holm, R. H., and Walker, F. A. *J. Am. Chem. Soc.* **1973**, *95*, 63-75.

48. Cheng, B. S., Hobbs, J. D., Debrunner, P. G., Erlebacher, J., Shelnutt, J. A., and Scheidt, W. R. *Inorg. Chem.* **1995**, *34*, 102-110.

49. Arulsamy, N., Bohle, D. S., Imonigie, J. A., and Sagan, E. S. *J. Am. Chem. Soc.* **2000**, *122*, 5539-5549.

50. Ahmed, M., Edwards, A. J., Jones, C. J., McCleverty, J. A., Rothin, A. S., and Tate, J. P. *J. Chem. Soc., Dalton Trans.* **1988**, 257-263.

51. APEX2, *Data Collection: APEX2 Software Reference Manual*. 2007, Bruker-AXS: Madison, WI.

52. SAINT *Data Reduction: SAINT Software Refence Manual. Bruker-AXS, Madison, WI.* **2007**.

53. Freeman, J. P. *J. Org. Chem.* **1963**, *28*, 2508-2511.

54. Lapinski, A., Spanget-Larsen, J., Waluk, J., and Radziszewski, J. G. *J. Chem. Phys.* **2001**, *115*, 1757-1764.

55. Gottlieb, H. E., Kotlyar, V., and Nudelman, A. *J. Org. Chem.* **1997**, *62*, 7512-7515.

56. Gonzalez, J. A. and Wilson, L. J. *Inorg. Chem.* **1994**, *33*, 1543-1553.

57. Bain, G. A. and Berry, J. F. *J. Chem. Educ.* **2008**, *85*, 532-536.

58. Carlin, R. L. **1986**.

59. Krzystek, J., Sienkiewicz, A., Pardi, L., and Brunel, L. C. *J. Magn. Reson.* **1997**, *125*, 207-211.

60. Samuel, P. P., Mondal, K. C., Sk, N. A., Roesky, H. W., Carl, E., Neufeld, R., Stalke, D., Demeshko, S., Meyer, F., Ungur, L., Chibotaru, L. F., Christian, J., Ramachandran, V., van Tol, J., and Dalal, N. S. *J. Am. Chem. Soc.* **2014**, *136*, 11964-11971.

61. Liu, W. J., Christian, J. H., Al-Oweini, R., Bassil, B. S., van Tol, J., Atanasov, M., Neese, F., Dalal, N. S., and Kortz, U. *Inorg. Chem.* **2014**, *53*, 9274-9283.

62. Zahran, Z. N., Shaw, M. J., Khan, M. A., and Richter-Addo, G. B. *Inorg. Chem.* **2006**, *45*, 2661-2668.

63. Connelly, N. G. and Geiger, W. E. *Chem. Rev.* **1996**, *96*, 877-910.

64. Shaw, M. J., Henson, R. L., Houk, S. E., Westhoff, J. W., Jones, M. W., and Richter-Addo, G. B. *J. Electroanal. Chem.* **2002**, *534*, 47-53.

65. Carter, S. M., Lee, J., Hixson, C. A., Powell, D. R., Wheeler, R. A., Shaw, M. J., and Richter-Addo, G. B. *Dalton Trans.* **2006**, 1338-1346.

66. van der Sluis, P. and Spek, A. L. *Acta Cryst.* **1990**, *A46*, 194-201.

Chapter 3: Hydride Attack on a Coordinated Ferric Nitrosyl: Experimental and Theoretical Evidence for the Formation of Fe−HNO and (NO)Fe−H complexes*

3.1 Introduction

HNO is the conjugate acid of the one-electron reduced NO. HNO elicits biological responses such as vasodilation and cardioprotection,[1] but unlike NO, is unstable in the free state. It is also present as a heme ligand in heme-HNO intermediates in important biological processes such as NO detoxification by fungal cytochrome P450 nitric oxide reductase (P450nor)[2,3] (Fig. 3.1, eq. 3.1), and in the reaction cycles of cyt *c* nitrite reductase (ccNiR)[4,5] and hydroxylamine oxidoreductase.[6]

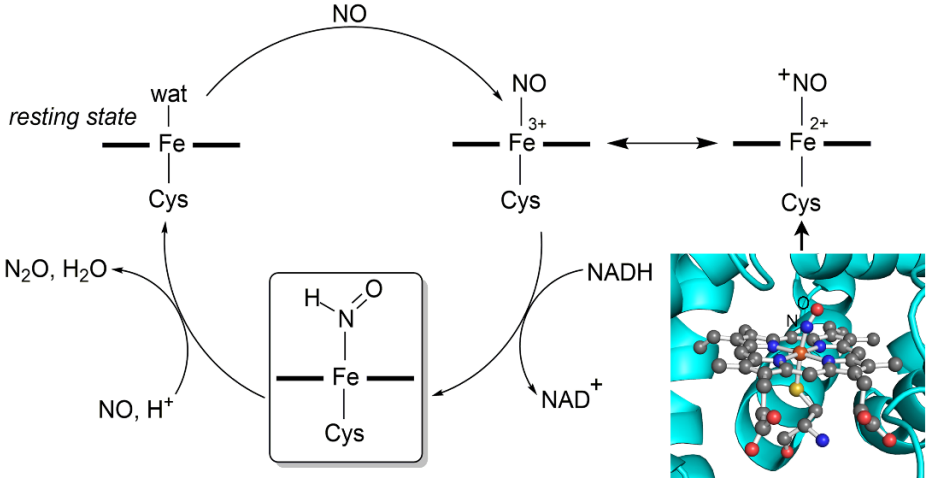

Figure 3.1. Simplified proposed mechanism of the reduction of NO to N_2O catalyzed by fungal cyt P450nor. The active site of the fungal P450nor from *Fusarium oxysporum* showing the coordinated NO ligand in the distal pocket (*inset*).

*Reproduced in part from, "Hydride Attack on a Coordinated Ferric Nitrosyls: Experimental and DFT Evidence for the formation of a Heme Model-HNO Derivative" E.G. Abucayon, R.L. Khade, D.G. Powell, Y. Zhang, G.B. Richter-Addo. *J. Am. Chem. Soc.* **2016**, *138*, 104-107 with permission from the American Chemical Society. *Copyright © ACS*; "Over or under: hydride attack at the metal versus the coordinated nitrosyl ligand in ferric nitrosyl porphyrins" E.G. Abucayon, R.L. Khade, D.G. Powell, M.G. Shaw, Y. Zhang, G.B. Richter-Addo. *Dalton Trans*. **2016**, *45*, 18259-18266 with permission from The Royal Society of Chemistry. *Copyright © RSC Publishing*.

Outstanding work by Farmer has resulted in the spectroscopic characterization of several heme protein-HNO adducts.[7] Coordination compounds with HNO ligands have been reviewed. [1,8,9]

Heme-HNO intermediates in biology may be generated either from proton attack at reduced nitrosyl moieties such as proposed in *cc*NiR (eq. 3.1; right)[4,5], or from hydride attack at the ferric nitrosyl center in cyt P450nor (eq. 3.1; left).[2] Elegant work by Ryan,[10] Meyer,[11] and others have shown that (por)Fe-HNO species are likely intermediates during the electrochemical reductions of ferrous-NO compounds in the presence of protons (eq. 3.1; right) to yield Fe-NH_2OH derivatives and NH_3. A similar inference of an Fe-HNO species was based on UV-vis spectroscopy[12] but no definitive spectral signals to verify the presence of bound HNO were obtained.

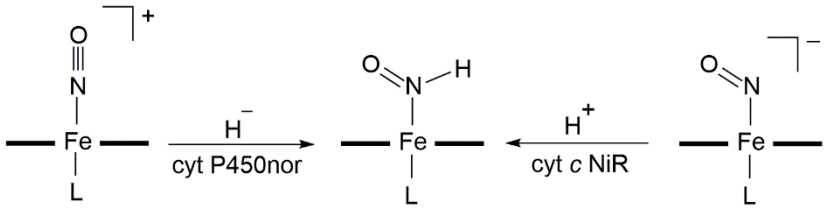

(**3.1**)

Although nucleophilic attack by hydride (H^-) at a ferric−NO moiety is a key step in NO detoxification by fungal P450nor *en route* to hyponitrite and N_2O formation, there were no well-defined examples of this nucleophilic reaction type in Fe heme models (Fig. 3.1, eq. 3.1; left) prior to my work in this area. Indeed, despite the importance of heme-HNO intermediates in biology, it is surprising that to date there are no reports of well-characterized Fe heme model-HNO compounds, and very little experimental information on heme model-HNO compounds is available. The closest example, but non-biologically

relevant, is the related low-spin Ru compound (TTP)Ru(NO)(HNO)(1-MeIm) reported by our research group just over a decade ago[13] and a hydride attack on a coordination complex $[(py(by)S_4)Ru(NO)]^+$ to give the Ru-HNO derivative reported by Sellman in 2001.[14] Although density functional theory (DFT) calculations have aided significantly in our theoretical understanding of these HNO species,[5,15-18] the general lack of appropriate heme model-HNO compounds has hindered research in this important area.

This chapter describes the preparation of pure and stable ferric nitrosyl precursors of the form [(por)Fe(NO)(L)]OTf (por = OEP, PPDME, TTP; L = 5-MeIm, 1-MeIm, 1-EtIm, and Im). The reactivity of these complexes with the hydride anion (H^-) to generate FeHNO model complexes and their subsequent variable decomposition pathways are described. The reaction pathway for Fe(N−H)O formation (*i.e.*, H^- attack at bound NO) is compared with that of (NO)Fe−H bond formation (*i.e.*, H^- attack at the Fe center). DFT calculations were used to probe the reaction pathways for Fe−HNO and (NO)Fe−H formation. This chapter also provides insight into the N−N coupling reaction of FeHNO model complexes with external NO, another key step in the fungal NO reduction to give N_2O catalyzed by P450nor. The overall goal of my research in this area was to fill in the important gaps in knowledge in the field of HNO chemical biology.

3.2 Results and Discussion

3.2.1 Synthesis and Spectroscopy of the Six-coordinate {FeNO}^{6} Precursors

The six-coordinate [(por)Fe(NO)(L)]OTf (por = OEP, PPDME, TTP; L = 5-MeIm, 1-MeIm, 1-EtIm, and Im) precursors were synthesized according to the method used to prepare other {FeNO}^{6} complexes (eq. 3.2) with slight modifications.[19]

$$[(por)Fe]OTf \xrightarrow[L]{NO} [(por)Fe(NO)(L)]OTf \qquad (\mathbf{3.2})$$

In a typical reaction, a CH_2Cl_2 solution of a 1:1 mixture of the [(por)Fe]OTf starting compound and an *N*-base ligand (L) was stirred for 1 to 2 h. The solution was then concentrated under reduced pressure to saturation (*i.e.*, without compound precipitation). This was followed by bubbling NO gas through the solution in an ice-bath for 3-5 min. An immediate color change from pale purple-brown to bright red-purple was observed. Solution IR spectra of the products were characterized by strong bands in the 1888−1917 cm^{-1} range assigned to ν_{NO}. Dry *n*-hexane was then slowly introduced to induce the precipitation of the final products [(por)Fe(NO)(L)]OTf. The solvent was decanted and the remaining solids subsequently dried *in vacuo*. IR (KBr) spectra of the products as solids showed strong peaks in the 1880−1905 cm^{-1} range assigned to the ν_{NO} bands of the products. UV-visible spectra of the final products were characterized by 3 major bands similar to those previously reported by the group of Scheidt for related species (Table 3.2).[19] ^1H NMR spectra of the OEP derivatives of these ferric nitrosyl complexes were consistent with their expected diamagnetic behavior (Fig. 3.2). Interestingly, [(OEP)Fe(NO)(L)]OTf (L = 5-MeIm, 1-MeIm, 1-EtIm, Im) derivatives as powders were found to be stable in air at room temperature for several months as judged by IR (KBr) spectroscopy. Their CH_2Cl_2 solutions were also stable for 4−7 days under inert atmosphere (N_2 gas) as judged by solution IR spectroscopy.

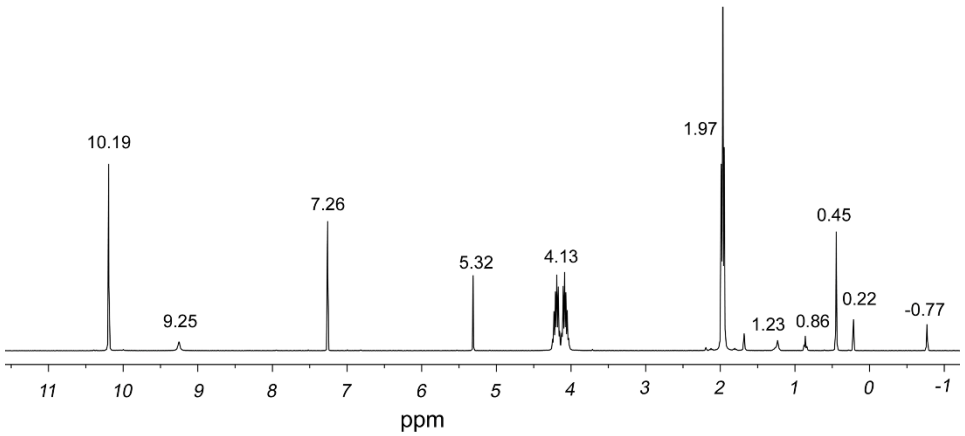

Figure 3.2. A representative ^{1}H NMR spectrum of the diamagnetic ferric nitrosyl [(OEP)Fe(NO)(5-MeIm)]OTf in $CDCl_3$ at −20 ˚C (400 MHz; δ, ppm); 10.19 (s, 4H, methine C−*H*), 9.25 (s, 1H, 5-MeIm N−*H*), 7.26 (s, $CHCl_3$), 5.32 (s, CH_2Cl_2), 4.13 (overlapping q, 16H, ethyl-CH_2), 1.97 (t, J_{H-H} = 7.6 Hz, 24H, ethyl-CH_3), 1.23 and 0.86 (hexane impurity), 0.45 (s, 3H, 5-MeIm-CH_3), 0.22 (s, 1H, 5-MeIm-H), −0.77 (s, 1H, 5-MeIm−H).

Worthy of mention is the sensitivity of the ν_{NO} bands of these complexes towards H-bonding of the *trans* axial ligands with the triflate anion. For example, the [(OEP)Fe(NO)(Im)]OTf derivative exhibits two ν_{NO} bands at 1906 and 1890 cm^{-1} (ν^{15}_{NO} = 1866 and 1854 cm^{-1}) in its IR spectrum. These two ν_{NO} bands are attributed to the species shown in the boxed area in Figure 3.3, namely, (i) with H-bonding between the ImN−H proton and the triflate anion, and (ii) without H-bonding.

I note that the H-bond between the N−H proton of the bound imidazole and triflate appears to impart stability in the case of isomer (i) as revealed by IR spectroscopy. The band at 1906 cm^{-1} (assigned to isomer ii) slowly diminishes with time; after 4 months of exposure to air at room temperature, only the band at 1890 cm^{-1} remained (Fig. 3.3b). The ν_{NO} band at 1906 cm^{-1} is close to that of the related [(OEP)Fe(NO)(1-EtIm)]OTf (ν_{NO} = 1908 cm^{-1}), which has no imidazole N−H available for H-bonding with the triflate anion.

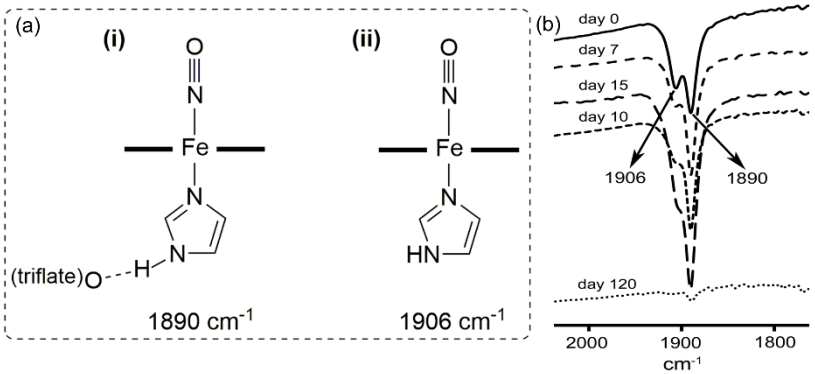

Figure 3.3. (a) Sketches of the two proposed structures present in the [(OEP)Fe(NO)-(Im)]OTf sample. (b) Infrared spectra of [(OEP)Fe(NO)(Im)]OTf highlighting its two ν_{NO} bands and its decomposition.

On other hand, the ν_{NO} band at 1890 cm^{-1} is very close to that of the [(OEP)Fe(NO)(5-MeIm)]OTf (ν_{NO} = 1895 cm^{-1}) which has been shown by X-ray crystallography to exhibit H-bonding at the N−H proton with triflate. The influence of H-bonding of the histidyl imidazole group on the chemical properties of hemes and model complexes has been reviewed previously.[20]

The preparation of the [(PPDME)Fe(NO)(L)]OTf derivative was performed in a similar manner as described for the OEP complexes. However, the final isolation of the ferric nitrosyl product was performed by crystallization in a CH_2Cl_2/CH_3OH solvent system at 0 ˚C. In the case of TTP derivatives, the ferric nitrosyls were prepared and characterized *in situ* without further isolation. The same procedure was followed as described above for the preparation of OEP derivatives except for the final step. Instead of precipitating the final products, the $CDCl_3$ solutions of these $[(TTP)Fe(NO)(L)]^+$ derivatives were maintained in an iced-bath temperature under the atmosphere of N_2. The

successful preparation of ferric nitrosyl complexes of TTP derivatives were confirmed by the formation of strong ν_{NO} peaks at 1900−1925 cm^{-1} in their solution IR spectra.

In general, the NO stretching frequencies of the synthesized ferric nitrosyl derivatives are in the range of those previously reported heme models and heme protein-NO complexes (Table 3.1). The successful isolation of the OEP derivatives of these ferric nitrosyl complexes in powder form was made possible due to (i) the eight electron-donating ethyl substituents in the α- and β-positions of the porphyrin, and (ii) the effect of the counteranion (trifate) on the stability of the ferric nitrosyls that was observed empirically. The electron-donating ability of ethyl substituents enhances the electron density at the Fe-center which, consequently strengthens the π-back donation from the metal d-electrons to the π*-orbital of the NO ligand.

Table 3.1. Vibrational and absorption spectral data for six coordinate ferric nitrosyl complexes.

Complexes	ν_{NO} (cm^{-1})	λ (nm)	Ref.
[(OEP)Fe(NO)(5-MeIm)]OTf	1895[a]	411, 526, 558[c]	tw
[(OEP)Fe(NO)(1-MeIm)]OTf	1888[a]	410, 526, 558[c]	tw
[(OEP)Fe(NO)(1-EtIm)]OTf	1908[a]	411, 526, 558[c]	tw
[(OEP)Fe(NO)(Im)]OTf	1906, 1890[a]	403, 524, 558[c]	tw
[(PPDME)Fe(NO)(5-MeIm)]OTf	1912[b]	–	tw
[(PPDME)Fe(NO)(1-MeIm)]OTf	1915[b]	–	tw
[(PPDME)Fe(NO)(Im)]OTf	1915[b]	–	tw
[(TTP)Fe(NO)(5-MeIm)]OTf	1912[b]	–	tw
[(TTP)Fe(NO)(1-MeIm)]OTf	1914[b]	–	tw
[(TTP)Fe(NO)(Im)]OTf	1917[b]	–	tw
[(OETPP)Fe(NO)(1-MeIm)]ClO_4	1871[d]	464, 577[c]	21
[(OEP)Fe(NO)(2-MeIm)]ClO_4	1917[d]	414, 529, 561[c]	21
[(OEP)Fe(NO)(1-MeIm)]ClO_4	1921[d]	410, 525, 558[c]	22
[(OEP)Fe(NO)(4-CNPy)]ClO_4	1916[d]	408, 524, 557[c]	22
[(OEP)Fe(NO)(Iz)]ClO_4	1914[d]	408, 524, 556[c]	22
[(OEP)Fe(NO)(PMS)]ClO_4	1913[d]	416, 528, 560[c]	22
[(OEP)Fe(NO)(2-MePrz)]ClO_4	1912[d]	408, 524, 557[c]	22
[(OEP)Fe(NO)(Prz)]ClO_4	1911[d]	408, 524, 557[c]	22
[(OEP)Fe(NO)(Pz)]ClO_4 [a]	1909[d]	409, 524, 557[c]	22
[(OEP)Fe(NO)(Pz)]ClO_4 [b]	1890[d]	–	22
[(OEP)Fe$(NO)_2$(Prz)]ClO_4	1899[d]	–	22
[(OEP)Fe(NO)(H_2O)]ClO_4	1937[a]	–	23
[(OEP)Fe(NO)(HO-*i*-C_5H_{11})]ClO_4	1935[a]	–	24
(T(piv)PP)Fe(NO_2)(NO)	1891[c]	433, 543[e]	25
(OEP)Fe(NO)(SR)	1850[c]	–	26
(T(piv)PP)Fe(NO)(SR)	1828	439, 555[c]	27
Heme protein-NO complexes			
P450cam-NO	1806	431, 541, 573	28, 29
P450cam-NO + adamantone	1818	–	28, 29
CPO-NO	1868	–	29, 30
HRP-NO	1903	–	31, 32
NorBC-NO	1904	416, 562	33
Mb-NO	1927	420, 536, 564	34
Hb-NO	1925	533, 566	35
rNp1-NO	1917	419	36, 37
hHO-1-NO	1918	416, 530, 566	38

a = KBr, b = $CHCl_3$, c = CH_2Cl_2, d = Nujol, e = toluene, tw = this work

3.2.2 Molecular Structures of the {FeNO}^{6} Derivatives

The molecular structures of the compounds [(OEP)Fe(NO)(L)]OTf (L = 5-MeIm, 1-MeIm, 1-EtIm, and Im) and [(PPDME)Fe(NO)(5-MeIm)]SbF_6 were determined by X-ray crystallography. Selected bond lengths (Å) and bond angles (˚) for these complexes were collected in Table 3.2.

Table 3.2. Selected geometrical parameters for the new and some previously reported six-coordinate {FeNO}^{6} compounds.

Compound	Fe-N(O) (Å)	Fe-N(axial) (Å)	Fe-Np (Å)	Fe-N-O (˚)	Ref.
$[(OEP)Fe(NO)(5\text{-}MeIm)]^{+a}$	1.6437(16)	1.9823(15)	2.008(2)	175.38(2)	tw
$[(OEP)Fe(NO)(1\text{-}MeIm)]^{+a}$	1.6408(12)	1.9941(11)	2.009(11)	172.60(2)	tw
$[(OEP)Fe(NO)(1\text{-}EtIm)]]^{+a}$	1.645(2)	1.990(2)	2.007(2)	178.8(2)	tw
$[(OEP)Fe(NO)(Im)]^{+a}$	1.649(2)	1.983(2)	2.004(2)	176.0(2)	tw
$[(PPDME)Fe(NO)(5\text{-}MeIm)]^{+b}$	1.654(5)	1.990(5)	2.000(5)	174.8(5)	tw
$[(OEP)Fe(NO)(1\text{-}MeIm)]^{+c}$	1.6465(2)	1.9889(16)	2.003(5)	177.28(2)	22
$[(OEP)Fe(NO)(Pz)]^{+c}$	1.627(2)	1.988(2)	2.004(5)	176.9(3)	22
$[(OEP)Fe(NO)(Iz)]^{+c}$	1.632(3)	2.010(3)	1.996(4)	177.6(3)	22
$[((OEP)Fe(NO))_2(Prz)]^{2+c}$	1.632(3)	2.039(2)	1.995(8)	176.5(3)	22
$[(TPP)Fe(NO)(H_2O)]^{+c}$	1.652(5)	2.001(5)	1.999(6)	174.4(10)	23
$[(TPP)Fe(NO)(HOC_5H_{11})]^{+c}$	1.776(5)	2.063(3)	2.013(3)	177.1(7)	24
$(T(piv)PP)Fe(NO)(NO_2)$	1.671(2)	1.998(2)	1.996(4)	169.3(2)	25
$[(OETPP)Fe(NO)(1\text{-}MeIm)]^{+c}$	1.650(2)	1.983(2)	1.990(9)	177.0(3)	21
$[(OEP)Fe(NO)(2\text{-}MeIm)]^{+c}$ (p)	1.649(2)	2.053(2)	2.014(8)	175.6(2)	21
$[(OEP)Fe(NO)(2\text{-}MeIm)]^{+c}$ (r)	1.648(2)	2.032(2)	2.003(7)	177.4(2)	21
NP_4(III)-NO	1.66(1)	2.013(9)	1.99(1)	156.0(1)	39

a = OTf^-, b = SbF_6^-, c = ClO_4^-, p = planar, r = ruffled, tw = this work, Pz = pyrazole, Iz = indazole, Prz = pyrazine, NP_4 = nitrophorin 4

The near-linear Fe−N−O linkages (bond angles between 174−180˚, Table 3.2) displayed by the $[(por)Fe(NO)L)]^+$ compounds are consistent with the high NO stretching frequencies observed in their IR spectra (Table 3.1). The molecular structures of compounds **1**, **2**, **3**, **4**, and **5** with their axial ligand orientations relative to the porphyrin cores, and their perpendicular atom displacements relative to the 24-atom mean planes of the porphyrins are shown in Figures 3.4−3.8.

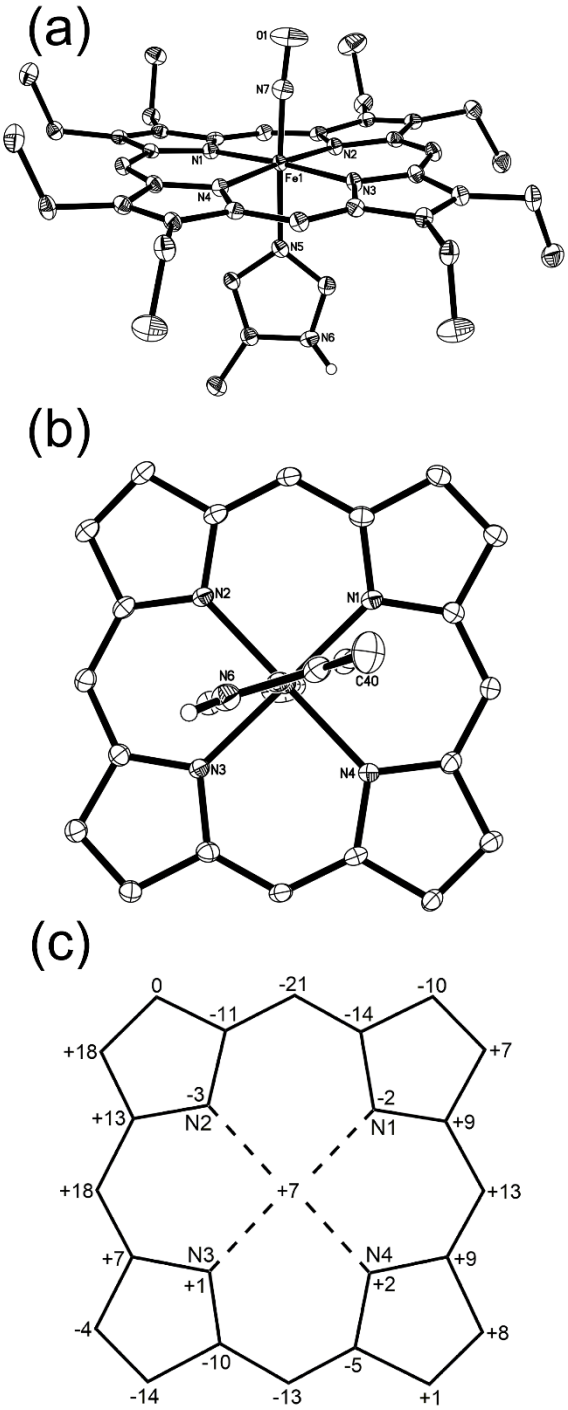

Figure 3.4. (a) Molecular structure of the cation of [(OEP)Fe(NO)(5-MeIm)]OTf, (b) View of the axial ligand orientation relative to the porphyrin plane**,** (c) Perpendicular atom displacements (in Å x 100) of the porphyrin core atoms relative to the 24-atom mean plane of the porphyrin. H atoms have been omitted for clarity except for the N6−H proton.

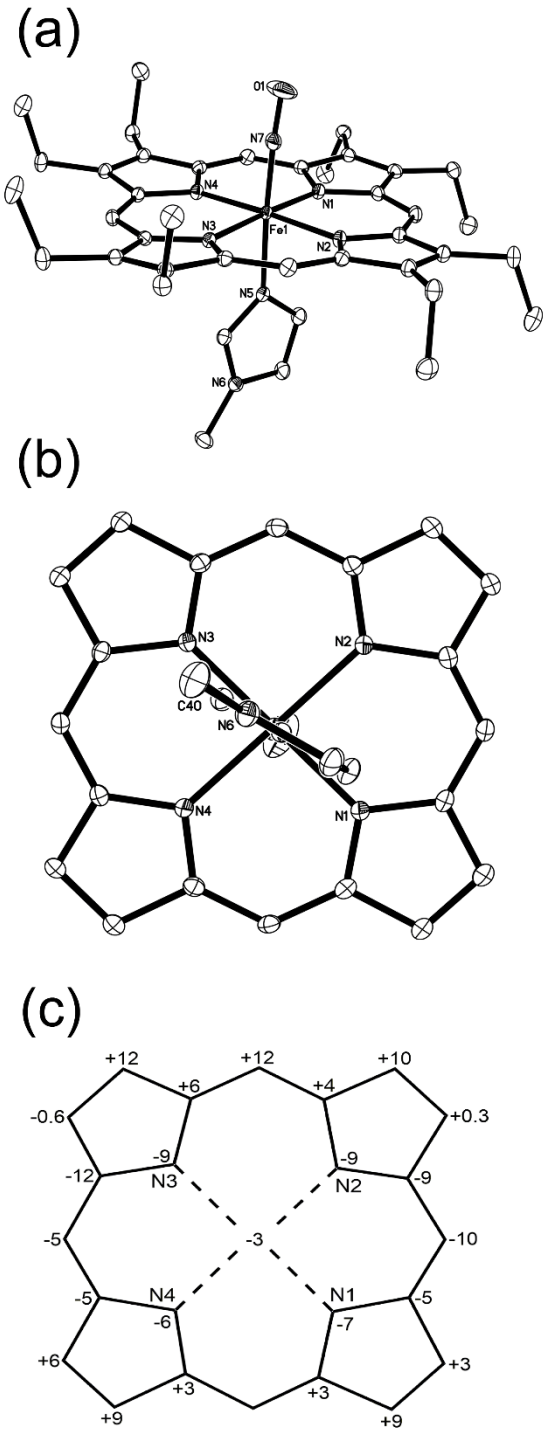

Figure 3.5. (a) Molecular structure of the cation of [(OEP)Fe(NO)(1-MeIm)]OTf, (b) View of the axial ligand orientation relative to the porphyrin plane**,** (c) Perpendicular atom displacements (in Å x 100) of the porphyrin core atoms relative to the 24-atom mean plane of the porphyrin. H atoms have been omitted for clarity.

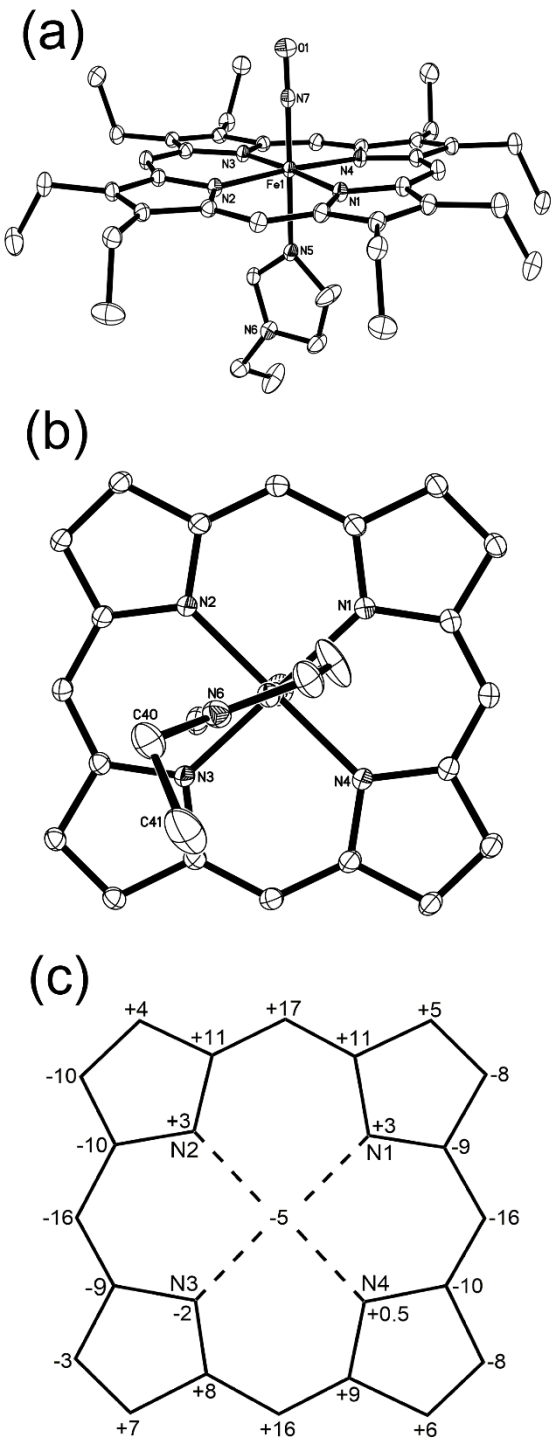

Figure 3.6. (a) Molecular structure of the cation of [(OEP)Fe(NO)(1-EtIm)]OTf, (b) View of the axial ligand orientation relative to the porphyrin plane**,** (c) Perpendicular atom displacements (in Å x 100) of the porphyrin core atoms relative to the 24-atom mean plane of the porphyrin. H atoms have been omitted for clarity.

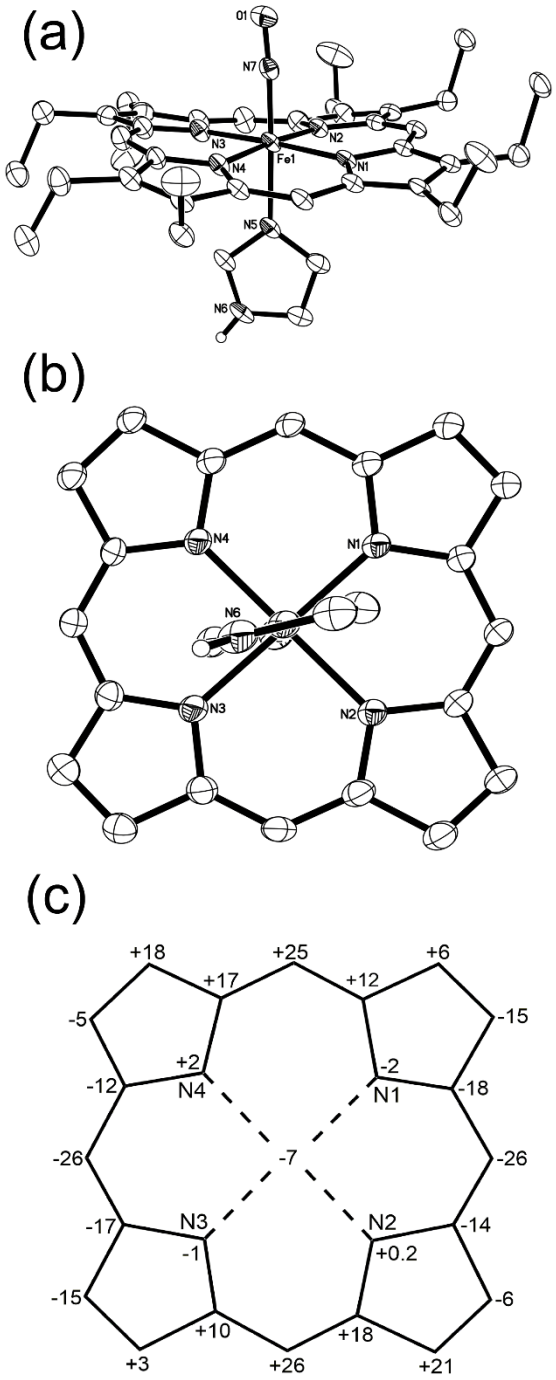

Figure 3.7. (a) Molecular structure of the cation of [(OEP)Fe(NO)(Im)]OTf, (b) View of the axial ligand orientation relative to the porphyrin plane**,** (c) Perpendicular atom displacements (in Å x 100) of the porphyrin core atoms relative to the 24-atom mean plane of the porphyrin. H atoms have been omitted for clarity except for the N6−H proton.

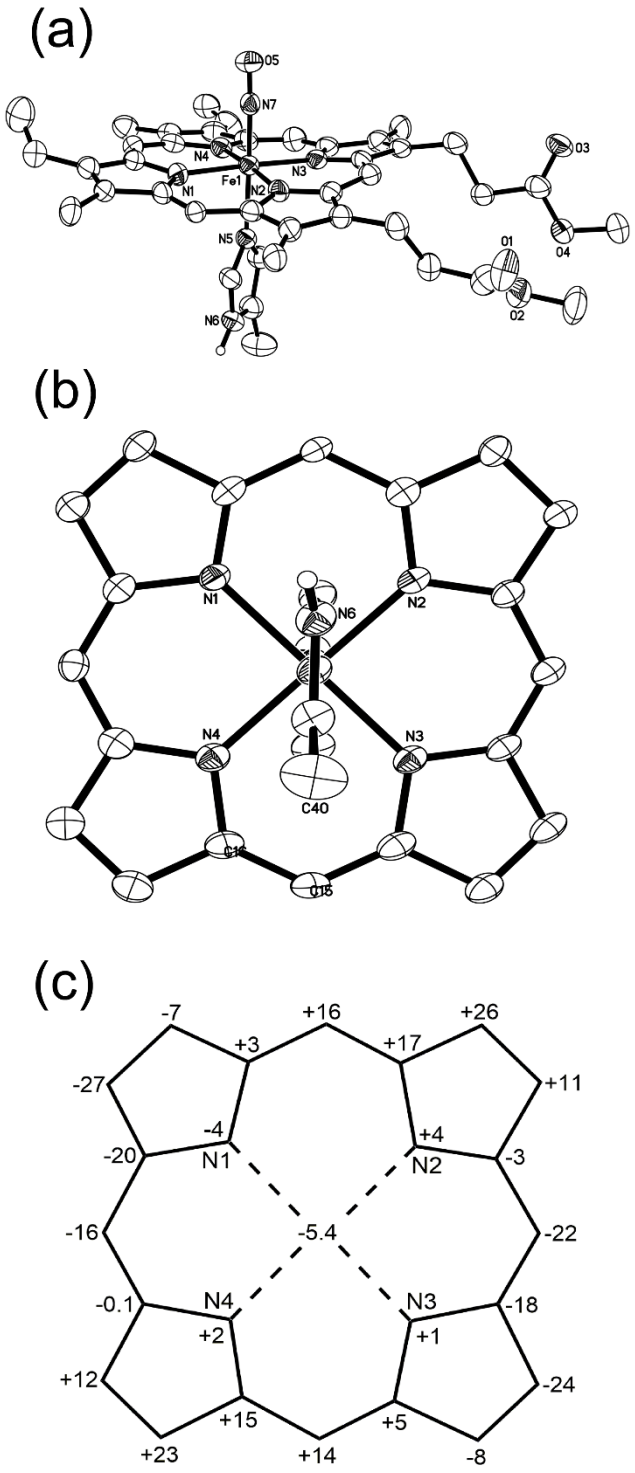

Figure 3.8. (a) Molecular structure of the cation of [(PPDME)Fe(NO)(5-MeIm)]SbF_6, (b) View of the axial ligand orientation relative to the porphyrin plane**,** (c) Perpendicular atom displacements (in Å x 100) of the porphyrin core atoms relative to the 24-atom mean plane of the porphyrin. H atoms have been omitted for clarity except for the N6−H proton.

The Fe−N(O) bond distances in these ferric−NO complexes are within the range of those previously reported six coordinate ferric nitrosyls (Table 3.2). The average Fe−Np bond distances are also within the range of those observed in the diamagnetic ferric nitrosyl porphyrins,[40] and consistent with our ^{1}H NMR spectroscopy experiments that confirm the diamagnetic behavior of the complexes. I note that there are variable porphyrin core distortions/deformations observed in these heme ferric nitrosyl models depending on methyl/ethyl substitution pattern of the imidazole *trans* ligand. The ferric nitrosyls bearing *trans* imidazole ligands with an N−H moiety such as with 5-MeIm and Im show saddled porphyrin core deformations while the complexes having an imidazole with an N-alkyl moiety (*e.g.*, 1-MeIm and 1-EtIm) show ruffled core deformations. The types of distortions used in describing porphyrin cores in heme models are reviewed elsewhere.[41]

3.2.3 Reactions of the Six-coordinate {FeNO}^{6} Complexes with Hydride to Form the Elusive FeHNO Derivatives

Although Fe-bound HNO species have long been known to be involved in many physiological and biological processes[1,42] and implicated as the key active intermediates in the fungal P450 NO reduction pathway, it is surprising that there were no well-characterized Fe−HNO heme model systems prior to my work in this area. A couple of years ago, and as a result of a research discussion I had with our group, I became interested in utilizing novel synthetic methodologies to try to detect such Fe−HNO species that had eluded the scientific community for over five decades.

3.2.3.1 Formation of Fe−HNO complexes

Hydride attack on the ferric nitrosyl cation was monitored by low temperature IR and ^{1}H NMR spectroscopy, and both spectral techniques point to the formation of the ferrous (por)Fe(HNO)(L) (por = OEP, PPDME, TTP; L = 5-MeIm, 1-MeIm, and Im) products (eq. 3.3).

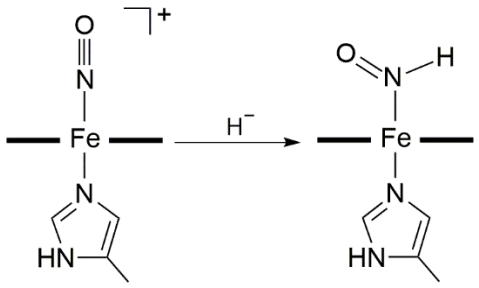

(3.3)

In a typical reaction, 1.5 equiv of a hydride source (*i.e.*, $[NBu_4]BH_4$) was added to a ferric nitrosyl precursor [(por)Fe(NO)(L)]OTf solution at low temperature. For example, addition of 1.5 equiv of $[NBu_4]BH_4$ to a $CHCl_3$ (1.5 mL) solution of [(OEP)Fe(NO)(5-MeIm)]OTf (9.5 mg, 0.011 mmol) at –45 °C resulted in a decrease of the precursor ν_{NO} band in the IR spectrum at 1912 cm^{-1} with concomitant formation of a medium intensity band at 1383 cm^{-1} (Fig. 3.9a). Employing the ^{15}N-labeled precursor [(OEP)Fe(^{15}NO)(5-MeIm)]OTf ($\nu_{^{15}NO}$ = 1874 cm^{-1}) for the reaction shifted this isotope-sensitive band from 1383 cm^{-1} in the unlabeled product to 1360 cm^{-1} (Fig. 3.10), confirming the assignment of this new band to ν_{NO} of the product.

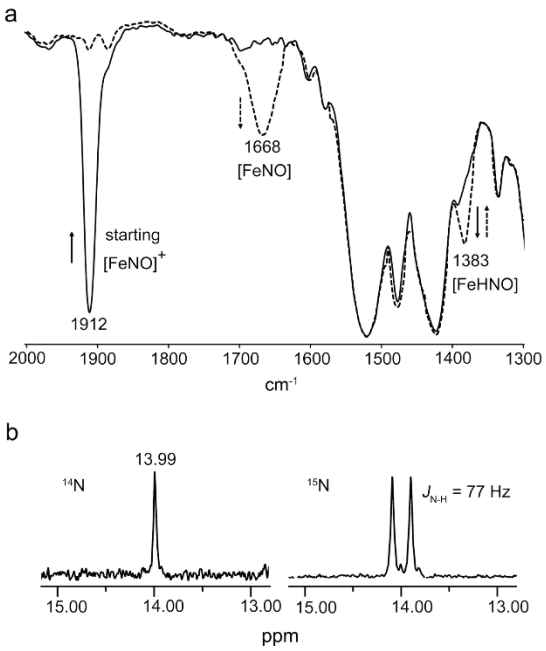

Figure 3.9. Spectroscopic characterization of the bound HNO ligand in (OEP)Fe(HNO)(5-MeIm). (a) IR spectrum showing the formation of the ν_{NO} band at 1383 cm^{-1} (dashed line) upon hydride addition to the cationic precursor (ν_{NO} = 1912 cm^{-1}). (b). ^{1}H NMR spectrum showing the formation of the HNO ligand at δ = 13.99 ppm (*left*) and the $J_{^{15}NH}$ coupling for the FeH^{15}NO derivative (*right*).

Addition of PPh_3 as an HNO trap[43] to the product mixture at –45 °C resulted in the generation of HN=PPh_3 (*m/z* 278.1101) and O=PPh_3 (*m/z* 279.0937) as determined by ESI mass spectrometry, confirming the formation of HNO in the product of eq. 3.3. The ν_{NO} band at 1383 cm^{-1} for this ferrous porphyrin derivative is in the range observed for non-porphyrin metal-HNO complexes (1335−1493 cm^{-1})[8] and is similar to the ν_{NO} determined for Mb(HNO) (1385 cm^{-1}).[44] This new 1383 cm^{-1} band assigned to (OEP)Fe(HNO)(5-MeIm) slowly converts to a band at 1668 cm^{-1} assigned to the ν_{NO} of known five-coordinate (OEP)Fe(NO), even at −20 ˚C, with an overall yield of ~85% based on the precursor ferric nitrosyl cation (ν_{NO} = 1912 cm^{-1}; Fig. 3.9a) as judged by IR spectroscopy.

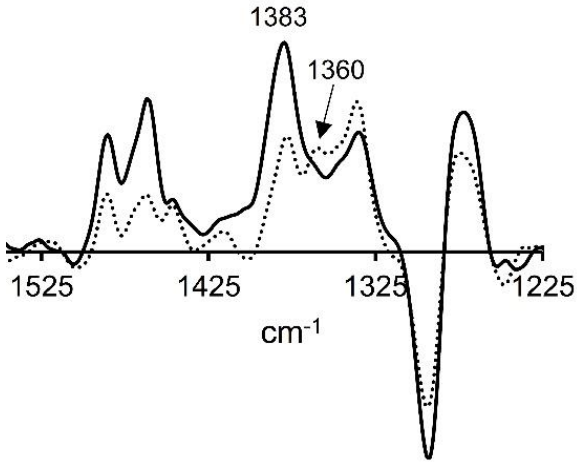

Figure 3.10. Difference IR spectra (product minus reactant) showing the new ν_{NO} bands for (OEP)Fe(HNO)(5-MeIm) (solid line; 1383 cm^{-1}) and the $H^{15}NO$ derivative (dashed line; 1360 cm^{-1}).

Monitoring the hydride addition to the ferric nitrosyl cation (eq. 3.3) in $CDCl_3$ at –20 °C by ^1H NMR spectroscopy revealed the appearance of a new peak at 13.99 ppm assigned to the bound HNO of the product of eq. 3.3 (Fig. 3.9b). When the ^{15}N-labeled nitrosyl cation precursor is used for the reaction, this new peak splits into a doublet with a $J_{^{15}NH}$ coupling constant of 77 Hz. The downfield ^1H NMR chemical shift of 13.99 ppm for the bound HNO ligand in (OEP)Fe(HNO)(5-MeIm) is close to those determined for ferrous heme globin-HNO adducts (14.63−15.53 ppm) reported by Farmer and coworkers.[7] The magnitude of the $J_{^{15}NH}$ coupling constant (77 Hz) is typical for N-coordinated HNO ligands and consistent with the direct attachment of the proton to the N-atom of the HNO moiety.[45] Examination of the ^1H NMR spectrum (Fig. 3.9b) revealed the presence of a minor (~9% of the HNO signal) species with δ = 13.91 ppm and $J_{^{15}NH}$ = 74 Hz, which I tentatively assign as a rotational isomer. I note that similar minor signals have been observed in some heme protein-HNO adducts.[7] The (OEP)Fe(HNO)(5-MeIm) compound is thermally unstable; however at −20 °C the ^1H NMR signal for the bound

Fe-HNO species persists in the product mixture for at least 2-4 hours, and integrates to ~11% yield at this temperature.

The generality of this hydride reaction on a bound ferric nitrosyl in a broad range of nitrosyl complexes of ferric porphyrins appears to be borne out by this work. An important example is the hydride attack on a bound ferric nitrosyl of a more biologically relevant protoporphyrin-IX dimethylester (PPDME-IX) derivative, namely [(PPDME)Fe(NO)(5-MeIm)]OTf (ν_{NO} = 1915 cm^{-1}) at low temperature that resulted in the formation of the ferrous (PPDME)Fe(HNO)(5-MeIm) product (ν_{NO} = 1384 cm^{-1}; Fig. 3.11).

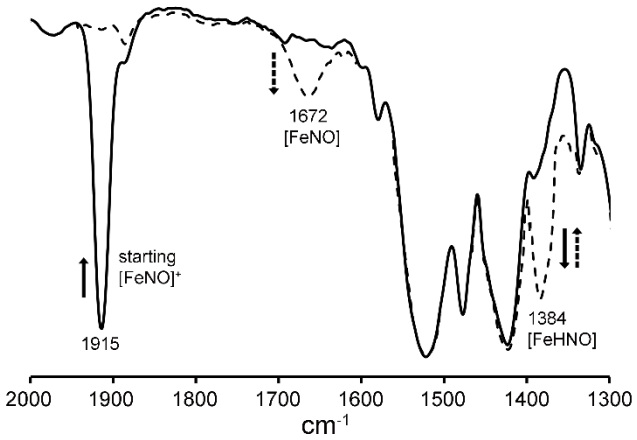

Figure 3.11. IR spectroscopic characterization of the bound HNO ligand in (PPDME)Fe(HNO)(5-MeIm), showing formation of the ν_{NO} 1384 cm^{-1} band (dashed line) upon hydride addition to the cationic precursor (ν_{NO} = 1915 cm^{-1}). The new 1384 cm^{-1} band slowly converts to the band at 1672 cm^{-1}.

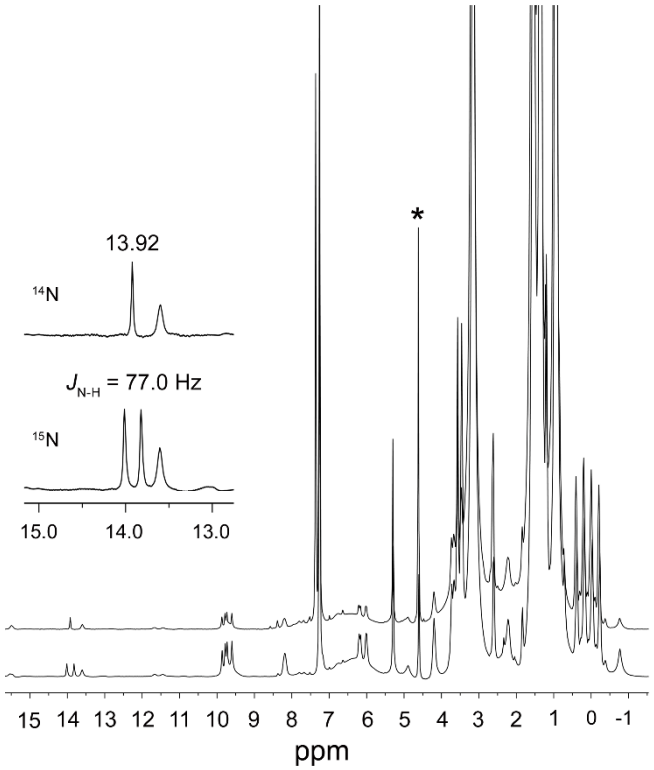

Figure 3.12. ^{1}H NMR spectral monitoring of the reaction of [(PPDME)Fe(NO)(5-MeIm)]OTf with [NBu$_4$]BH$_4$ in CDCl$_3$ to generate (PPDME)Fe(HNO)(5-MeIm). The bottom spectrum showing the splitting of the Fe−HNO peak at 13.92 ppm into a doublet was obtained using [(PPDME)Fe(^{15}NO)(5-MeIm)]OTf in the reaction. The peak labeled * is due to the H_2 decomposition product.

The generated (PPDME)Fe(HNO)(5-MeIm) product is also typified by a singlet peak at 13.92 ppm in the ^{1}H NMR spectrum that splits into a doublet ($J_{^{15}NH}$ = 77 Hz) with ^{15}NO labeling (Fig. 3.12). The percent yield of this hydride reaction on a bound ferric nitrosyl ranges from 5−21% as determined by ^{1}H NMR spectroscopy. That diborane is the boron-containing byproduct in the hydride attack at the bound NO$^+$ in [(por)Fe(NO)(L)]OTf was verified by ^{11}B{^{1}H} NMR spectroscopy (Fig. 3.13). This reaction mixture shows an identical ^{11}B NMR signal at −26 ppm when compared with the authentic diborane prepared from the reaction of borohydride with a reactive alkyl halide.[46]

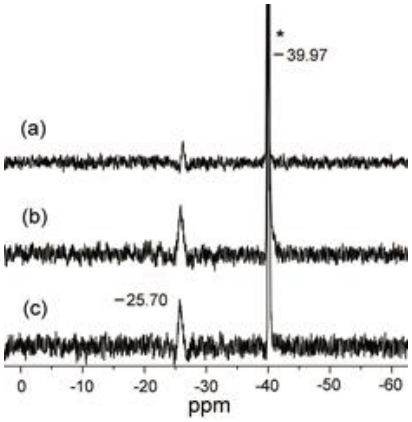

Figure 3.13. $^{11}B\{^{1}H\}$ NMR spectra of the product mixtures from (a) the reaction of [(OEP)Fe(NO)(5-MeIm)]OTf with excess $[NBu_4]BH_4$ (signal at –40 ppm), and (b) the reaction of [(OEP)Fe(NO)]OTf with excess $[NBu_4]BH_4$, and (c) the control and known reaction of $[NBu_4]BH_4$ with 1,2-dichloroethane to generate diborane.

The low-temperature IR and ^{1}H NMR spectral data for the ferric nitrosyl precursors $[(por)Fe(NO)(L)]^{+}$ and their corresponding Fe–HNO products prepared in this work are collected in Table 3.3.

Table 3.3. Spectral data for the precursor $[(por)Fe(NO)(L)]^{+}$ and (por)Fe(HNO)(L) complexes.[a]

		$[(por)Fe(NO)L]^{+}$	(por)Fe(HNO)(L)	
por	L	IR (cm^{-1})	IR (cm^{-1})	^{1}H NMR, ppm[b]
OEP	ImH	1911	1381	13.93 (78)
	5-MeIm	1910	1383	13.99 (76)
	1-MeIm	1912	1388	13.72 (77)
PPDME	ImH	1915	1382	13.90 (76)
	5-MeIm	1912	1384	13.92 (77)
	1-MeIm	1915	1384	13.65 (77)
TTP	ImH	1917	1386	14.20 (76)
	5-MeIm	1912	1381	14.26 (76)
	1-MeIm	1914	1389	14.02 (76)

[a] IR data in $CHCl_3$ (at –45 °C), and ^{1}H NMR data in $CDCl_3$ (at –20 °C). [b] The $J_{^{15}NH}$ coupling constants (in Hz) for the $Fe(H^{15}NO)$ derivatives are in parentheses.

3.2.3.2 DFT calculations for the hydride attack at the coordinated NO moiety

The mechanism of hydride attack on the ferric nitrosyl cation was investigated using DFT calculations by our collaborators. Three different DFT methods were used (detailed in the Experimental Sections), and all three methods showed basically the same trends. The mPW1PW91 method was previously found to yield excellent predictions of mechanistic properties,[47,48] hence results from this method are shown in Scheme 3.1 and discussed here.

For the isolated nitrosyl cation $[(P)Fe(NO)(5\text{-MeIm})]^+$ (reactant 1; R1 in Scheme 3.1; P = unsubstituted porphine macrocycle), the nitrosyl N-atom has a large positive charge of 0.705e, whereas the O-atom has a charge of –0.040e. This suggests that the N-atom shall be more easily attacked (than the O-atom) by the incoming negatively charged hydride from BH_4^- (reactant 2; R2) to form the HNO rather than the NOH product. Interestingly, we find that for the first intermediate formed from the intermolecular interaction between R1 and R2, all trials that attempted to place the hydride closer to the nitrosyl N-atom of R1 than the O-atom to form a potential I-1_N intermediate, resulted in the same structure as the intermediate I-1_O (*i.e.*, I-1_N = I-1_O; Scheme 3.1), with the distance between the hydride (H^-) to be transferred and the O-atom (2.738 Å) being shorter than that for the nitrosyl N-atom (3.353 Å). This is probably due to the repulsion between the strong negative charge of BH_4^- and the porphine ring. This result is reminiscent of that obtained from quantum chemical investigations of hydride attack on the NO moiety in the heme protein cyt P450nor.[3]

Since both the N- and O-atoms of the nitrosyl moiety in the first intermediate I-$1_{N/O}$ may, in principle, accept the transferred hydride from borohydride, we investigated

both the N- and O-pathways for hydride addition to the bound nitrosyl of the common intermediate I-$1_{N/O}$. Relative electronic energy (ΔE_{SCF}), zero-point energy corrected electronic energy ($\Delta E_{SCF+ZPE}$), enthalpy (ΔH), and Gibbs free energy (ΔG) results with respect to reactants for both the N- and O-pathways are shown in Table 3.4.

Table 3.4. Relative energies of all species in the N- and O-pathways using the mPW1PW91 method (Units: kcal/mol).

Pathway	System	ΔE_{SCF}	$\Delta E_{SCF+ZPE}$	ΔH	ΔG
	R1 + R2	0.00	0.00	0.00	0.00
	I-$1_{N/O}$	–9.81	–8.43	–8.21	0.51
N-path	TS-1_N	–9.22	–8.10	–8.51	2.25
	I-2_N	–41.91	–38.14	–38.76	–27.20
	P-1_N + P2	–29.93	–29.13	–28.76	–59.13
O-path	TS-1_O	10.47	8.57	8.41	18.59
	I-2_O	–18.22	–15.09	–15.62	–4.42
	P-1_O + P2	–8.30	–8.07	–7.57	–38.82

All the energy results show the same trend with the formation of the HNO complex (*i.e.*, N-pathway) having a much lower kinetic barrier and more favorable thermodynamic driving force.[3] Optimized structures of the lowest energy conformations of key species for the N- and O-pathways are shown in Scheme 3.1, as are selected bond lengths and angles for the complexes.

Hydride attack along the N-pathway (Scheme 3.1) proceeds via the transition state complex TS-1_N, in which the hydride to be transferred is positioned between the nitrosyl N-atom and boron. The geometric parameters (Scheme 3.1) show that this TS-1_N geometry is more similar to the reactants than the products, suggesting an early transition state for a facile reaction as observed experimentally. Charge analysis for TS-1_N shows that both the boron atom and the hydride to be transferred possess negative charges, –0.671e and –0.073e, respectively, to help repel each other to break the B–H bond in the

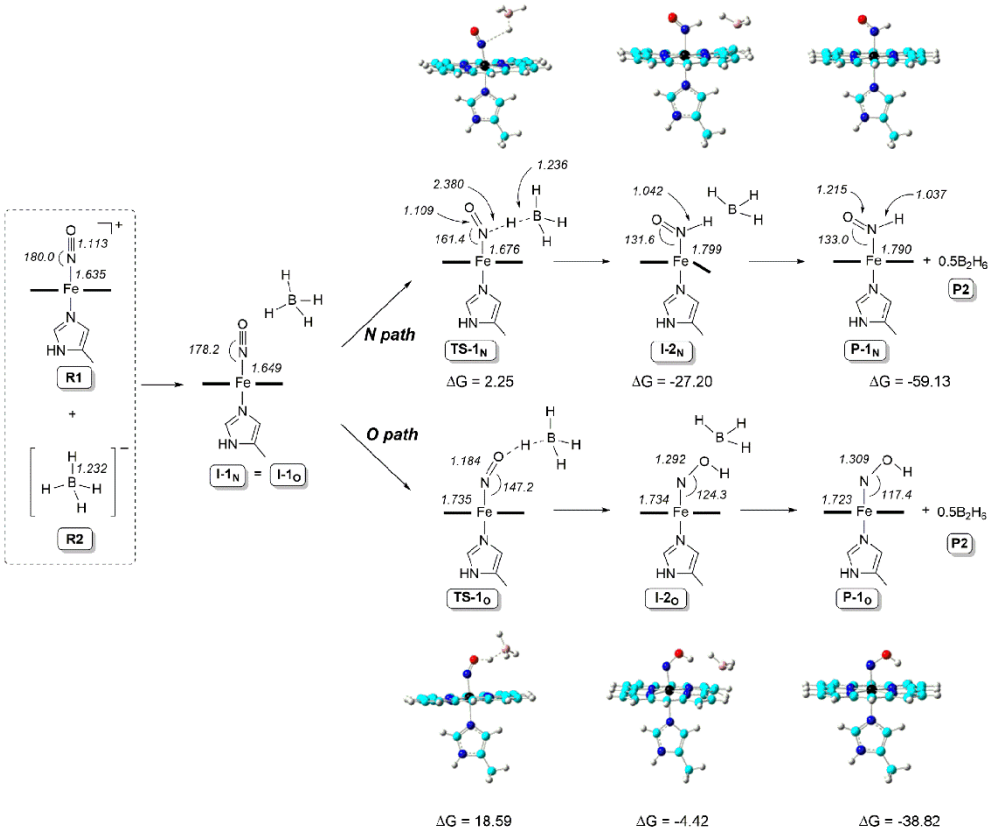

Scheme 3.1. DFT-calculated N- and O-pathways for hydride addition to the $[(P)Fe(NO)(5\text{-MeIm})]^+$ cation.

borohydride. The B–H bond cleavage generates the second intermediate I-2_N, followed by the BH_3 molecule dissociation and subsequent dimerization to form B_2H_6 and (porphine)Fe(HNO)(5-MeIm), as P2 and P-1_N products, respectively.

In contrast, reaction along the O-pathway (Scheme 3.1) generates the first transition state TS-1_O, for which charge analysis shows opposite charges for the boron atom (–0.237e) and the hydride to be transferred (0.243e). This results in an attraction between B and H that hinders the bond-breaking process needed for the hydride addition reaction to proceed via the O-pathway.

Further evidence for the formation of the Fe−HNO rather than the Fe–NOH product comes from calculations of the spectral properties of these adducts (Table 3.5). The NMR properties were calculated using the B3LYP method with solvent effects, similar to the approach used previously to study ^{1}H NMR chemical shifts in various organometallic complexes.[49] Compared to the experimental values for (OEP)Fe(HNO)(5-MeIm), our results for (P)Fe(HNO)(5-MeIm) (P-1_N in Scheme 3.1) only have errors of 0.08 ppm (^{1}H NMR) and 8 cm^{-1} (IR). In contrast, the calculations for the various (P)Fe(NOH)(5-MeIm) conformations yield much greater errors of ~2 ppm and/or up to 400 cm^{-1}.

Table 3.5. ^{1}H NMR chemical shifts (in ppm) and NO vibrational stretching frequencies (cm^{-1}) for the bound HNO/NOH ligands.

system		δ_H	ν_{NO}
(OEP)Fe(HNO)(5-MeIm)	expt	13.99	1383
(P)Fe(HNO)(5-MeIm) P-1_N	calc	13.91	1375
(P)Fe(NOH_{Down})(5-MeIm) P-1_O (*trans*)[a]	calc	11.92	1005
(P)Fe(NOH_{Down})(5-MeIm) P-1_O (*cis*)[a]	calc	11.36	992
(P)Fe(NOH_{Up})(5-MeIm)	calc	13.54	955

NO *trans*/*cis* with respect to the Me substituent of 5-MeIm. As this *trans/cis* effect is relatively small, only the *trans* isomer for the NOH_{up} conformation was studied here. The Down/Up conformations are for the H pointing to and away from the porphyrin ring, respectively.

The spectral data for the Fe–HNO complexes (Table 3.6) are reproduced well by DFT calculations using both the pyrrole-substituted (OEP) and *meso*-substituted (TTP) porphyrins, and an N-substituted imidazole (1-MeIm) and the histidine mimic (5-MeIm). Our experimental observations of a mild effect of OEP vs. TTP macrocycle and axial ligand (5-MeIm vs. 1-MeIm) type on ^{1}H NMR chemical shifts (range of 0.54 ppm; ~4%), but essentially negligible (<1%) υ_{NO} shifts for these systems, are reproduced by the

calculations (Table 3.6); with a range of proton shifts of 0.69 ppm (~5%) and a range of υ_{NO} shifts of <1%, affirming that ^{1}H NMR spectroscopy is a more sensitive structural probe for these Fe–HNO systems.

Table 3.6. NO vibrational frequencies and ^{1}H NMR chemical shifts.

System		δ_H (ppm)	ν_{NO} (cm^{-1})
Fe(TTP)(5-MeIm)(HNO)	Expt	14.26	1381
	Calc	14.60	1371
Fe(TTP)(1-MeIm)(HNO)	Expt	14.02	1389
	Calc	14.55	1369
Fe(OEP)(5-MeIm)(HNO)	Expt	13.99	1383
	Calc	13.91	1369
Fe(OEP)(1-MeIm)(HNO)	Expt	13.72	1388
	Calc	13.92	1371

3.2.3.3 Decomposition pathways of (por)Fe(HNO)(L)

IR and ^{1}H NMR spectroscopy, gas chromatography, and DFT calculations were used to probe the decomposition pathways for the ferrous (por)Fe(HNO)(L) products. Low temperature IR monitoring reveals that the peak at 1383 cm^{-1} assigned to ν_{NO} of (OEP)Fe(HNO)(5-MeIm) slowly decreases with concomitant formation of a new band at 1668 cm^{-1} assigned to the known five-coordinate (OEP)Fe(NO) (Fig. 3.9a). This observation is consistent with the low temperature ^{1}H NMR experiment showing a slow decomposition of the complex even at −20 ˚C with formation of the H_2 gas by-product as identified on the basis of its characteristic peak at 4.62 ppm in $CDCl_3$[50] (Fig. 3.14). The H_2 product was also detected in the headspace of the reaction mixture as revealed by ^{1}H NMR spectroscopy and gas chromatography, consistent with the previous report by Ryan.[10]

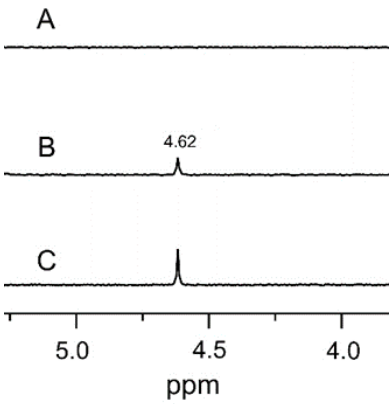

Figure 3.14. ^{1}H NMR spectroscopic detection of the H_2 by-product from the decomposition of (OEP)Fe(HNO)(5-MeIm) in $CDCl_3$. (A) Spectrum of the blank $CDCl_3$ solvent. (B) Spectrum of the reaction headspace. (C) Spectrum of an authentic H_2/N_2 mixture.

I find that these (OEP)Fe(HNO)L compounds decompose to generate H_2 (by ^{1}H NMR) and the five-coordinate (OEP)Fe(NO) derivative (by IR), with overall yields of 85% (L = 5-MeIm), 52% (L = ImH), and 76% (L = 1-MeIm), respectively, based on their cationic $[(OEP)Fe(NO)(L)]^{+}$ precursors. The analogous overall yields for the PPDME systems to give (PPDME)Fe(NO) are 41%, 65%, and 51%, respectively. We surmise that HNO dissociation from the six-coordinate (por)Fe(HNO)(imidazole) products does not occur, as N_2O (the HNO dimerization product) was not detected in the headspace gas by IR spectroscopy. Curiously, when borodeuteride is used for the reaction with the $[(OEP)Fe(NO)(5\text{-MeIm})]^{+}$ cationic precursor (eq. 3.3), D_2 is similarly generated (identified by ^{2}H NMR spectroscopy) together with (OEP)Fe(NO), but the presence of N_2O (by IR) and D_2O (by ^{2}H NMR spectroscopy) were also detected, indicative of both D–NO bond cleavage and partial DNO dissociation from the (OEP)Fe(DNO)(5-MeIm) complex (Scheme 3.2).

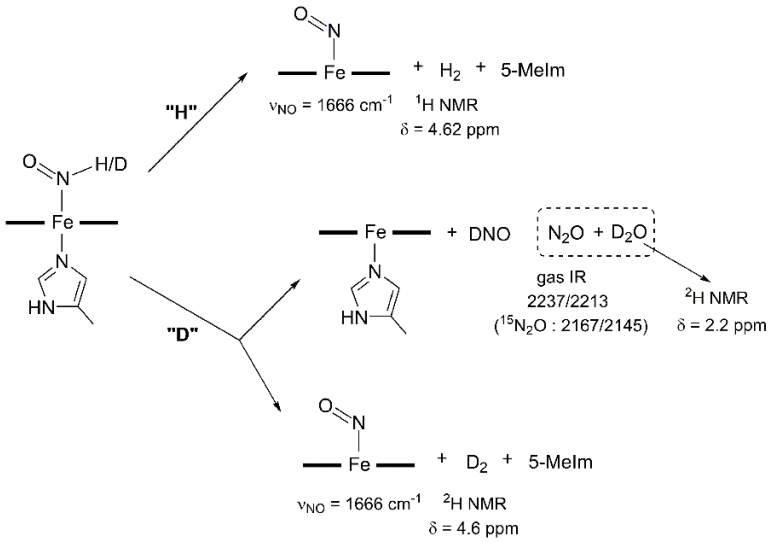

Scheme 3.2. Variable decomposition pathways of (por)Fe(HNO)(L). "H" refers to FeHNO decomposition; "D" refer to FeDNO decomposition.

DFT calculations were employed to gain insight on the stability and decomposition of the (por)Fe(HNO)(L) compounds. Selected data are shown in Fig. 3.15 and in Table 3.7. As seen from the enthalpy costs to break the H–NO and Fe–N(H)O bonds, the covalent H–NO bond is stronger than the Fe–N(H)O coordination bond, as expected from the bonding nature, and both bonds become stronger in the presence of the axial 5-MeIm ligand. Although the *trans* effect elongates the Fe–N(H)O bond length by 0.054 Å (Fig. 3.15) it also donates charge (0.248 e) to (P)Fe(HNO).

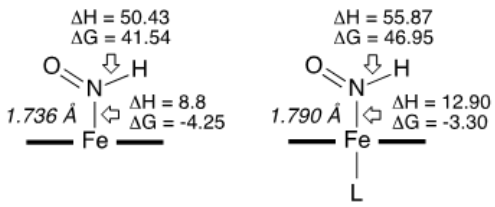

Figure 3.15. Bond strength energies (ΔH and ΔG) for the five-coordinate and six-coordinate Fe–HNO systems (L = 5-MeIm). Values are in kcal/mol.

The reaction pathway associated with Fe–N(H)O bond breaking and subsequent HNO dimerization is much more thermodynamically favorable, by ~44 kcal/mol in Gibbs free energy, than that associated with the H–NO bond breaking and subsequent H_2 formation. This is largely due to the strong thermodynamic driving force of HNO dimerization (ΔG of –44.46 kcal/mol; Table 3.7). In fact, the ΔG of –4.25 kcal/mol for the decomposition of the Fe–N(H)O bond in the five-coordinate (porphine)Fe(HNO) compound is similar to that for the H_2 formation pathway with an overall energy of –4.78 kcal/mol.

Table 3.7. Reaction energies (in kcal/mol) for the decomposition pathways of (por)Fe(HNO) vs. (por)Fe(HNO)(5-MeIm).

C.N.	Decomposition pathway	ΔG
5-C	(P)Fe(HNO) $\rightarrow$ (P)Fe + 1/2(N_2O + H_2O)	–48.71
5-C	(P)Fe(HNO) $\rightarrow$ (P)Fe(NO)+ 1/2 H_2	–4.78
6-C	(P)Fe(HNO)L $\rightarrow$ (P)Fe(L) + 1/2(N_2O + H_2O)	–47.76
6-C	(P)Fe(HNO)L $\rightarrow$ (P)Fe(NO) + L + 1/2 H_2	–3.19
	HNO $\rightarrow$ 1/2(N_2O + H_2O)	–44.46

The corresponding data for Fe–N(H)O decomposition and for H_2 formation pathways are similar for the six-coordinate (porphine)Fe(HNO)L, at –3.30 kcal/mol (Fig. 3.15) and –3.19 kcal/mol (Table 3.8), respectively. This suggests that the experimentally observed relative preference of H_2 formation in the presence of the axial ligand, versus HNO loss and subsequent dimerization, is not due to thermodynamics alone, but could be due to the kinetic effect of the hydrogen radical formation and dimerization.

3.2.3.4 Reactions of (por)Fe(HNO)(L) with external NO

The successful preparation and spectral characterization of the Fe–HNO complexes allowed us to probe their N–N bond-forming reactions with external

NO, a key coupling reaction step that is at the center of NO detoxification by fungal NO reductases (Figure 3.1).[17] As described above, the decomposition of the six-coordinate (OEP)Fe(HNO)(5-MeIm) complex generates H_2 and (OEP)Fe(NO) with no evidence of N_2O formation as judged by headspace IR spectroscopy. Interestingly, however, our preliminary results from the reactions of (OEP)Fe(HNO)(5-MeIm) with external NO show clear N_2O formation resulting from an N–N coupling reaction. To verify that N_2O was indeed formed from a coupling reaction involving the bound HNO and external NO, we employed various NO isotopomers (*i.e.*, containing ^{15}N and/or ^{18}O) in these reactions. Our results reveal that the terminal N-atom of the mixed-isotope N_2O product originates from the Fe-HNO moiety, whereas the central N- and the O-atoms of the N_2O product originate from the external NO reagent (sketched schematically at the top of Fig. 3.16).

The mixed-isotopic N_2O products were identified by their characteristic gas-phase IR spectra.[51] For example, the reaction of unlabeled (OEP)Fe(HNO)(5-MeIm) with external and doubly-labeled $^{15}N^{18}O$ generates $^{14}N^{15}N^{18}O$ (bands at 2185 and 2162 cm^{-1}) as shown in the solid trace in Fig. 3.16b. The related reaction of (OEP)Fe($H^{15}N^{18}O$)(5-MeIm) with unlabeled NO generates $^{15}N^{14}N^{16}O$ (Fig. 3.16c, broken line trace; bands at 2195 and 2169 cm^{-1}). Further, the reaction of (OEP)Fe($H^{15}NO$)(5-MeIm) with unlabeled NO generates $^{15}N^{14}N^{16}O$, namely the same reaction product from the (OEP)Fe($H^{15}N^{18}O$)(5-MeIm)/NO reaction. It is worthy to mention that addition of protons (e.g., from HOTf) in the reaction mixture appears to enhance the amount of the mixed isotope $^{14}N^{15}NO$ gas product.

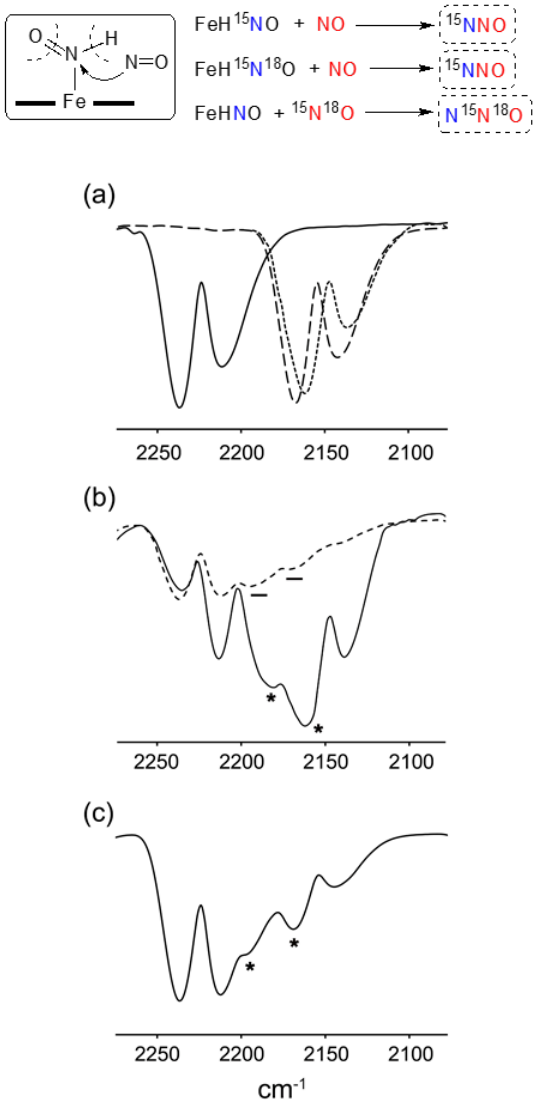

Figure 3.16. N_2O formation from the reactions of *in situ* generated (OEP)Fe(HNO)(5-MeIm) with external NO. (a) spectra of authentic samples of $^{14}N_2O$ (solid line trace, 2237/2212 cm^{-1}), $^{15}N_2O$ (broken line trace, 2167/2142 cm^{-1}), and $^{15}N_2{}^{18}O$ (dotted line trace, 2160/2138 cm^{-1}), (b) spectra of the headspace from the reactions of (solid line trace) (OEP)Fe(HNO)(5-MeIm) with $^{15}N^{18}O$, and (broken line trace) (OEP)Fe($H^{15}N^{18}O$)(5-MeIm) with NO; the newly formed mixed-isotope N_2O bands are highlighted. The solid line trace shows formation of $^{14}N^{15}N^{18}O$ (2185/2162 cm^{-1}), while the broken line trace shows formation of $^{15}N^{14}N^{16}O$ (2195/2169 cm^{-1}), (c) IR spectrum of the headspace from the reaction of (OEP)Fe($H^{15}NO$)(5-MeIm) with NO. The newly formed bands for the mixed-isotope $^{15}N^{14}N^{16}O$ product at 2195/2169 cm^{-1} are highlighted. The singly labeled N_2O gases are also present in the headspace, and provide good internal reference spectra.

Our finding that the terminal N-atom of the mixed-isotope N_2O products originates from the Fe–HNO moiety, whereas the central N- and O-atoms derive from external NO, is consistent with that predicted by DFT calculations for the related N–N coupling reaction catalyzed by fungal cyt P450nor.[17,52] The generation of the additional singly labeled (at the N-atom) N_2O isotopomers implies that other pathways may supplement the mixed-isotope Fe–HNO/NO coupling reactions observed in this non-protein system. Scheme 3.3 depicts the summary and proposed mechanism for NO to N_2O reduction by imidazole-ligated ferric heme models. It is noted that this N−N coupling reaction appears to be unique for Fe-HNO complexes as there is no N_2O gas observed from the reaction of Ru-HNO with external NO.

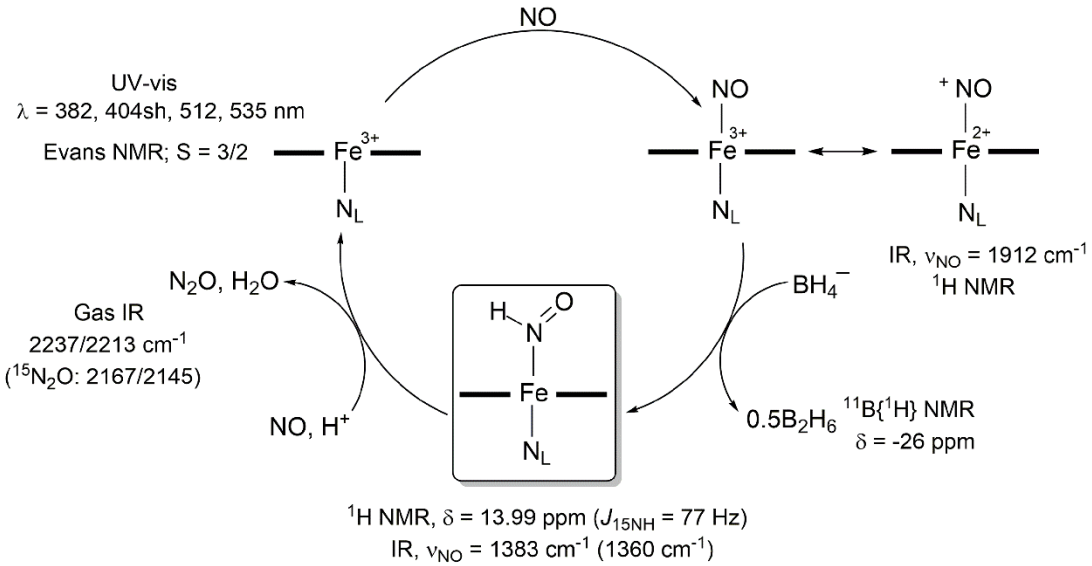

Scheme 3.3. Summary and proposed reaction mechanism of the NO to N_2O transformation mediated by the imidazole-ligated ferric porphyrin. The spectroscopic data are representative of the 5-MeIm-ligated derivative.

3.2.4 Reactions of the Five-coordinate {FeNO}^{6} Complexes with Hydride

The availability of both five- and six-coordinate ferric nitrosyls has allowed us to compare their reactivities with hydride experimentally and computationally. In the case of five-coordinate ferric nitrosyls, hydride can potentially attack both the Fe-center and the electrophilic N-atom of NO (eq. 3.4).

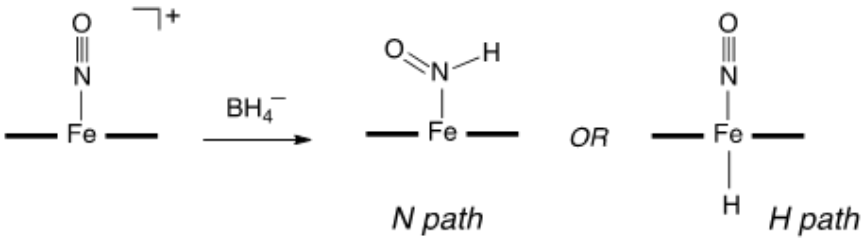

(**3.4**)

3.2.4.1 Formation of the Fe−H derivative

In contrast to what I observed with the six-coordinate ferric nitrosyls, the reaction of the five-coordinate [(OEP)Fe(NO)]$^+$ species with borohydride at −50 ˚C does not result in new ^{15}N isotope sensitive peaks in the 11−15 ppm region of the ^{1}H NMR spectrum attributable to an Fe–HNO derivative. Rather, a new sharp peak at –4.11 ppm is observed that we attribute to the six-coordinate Fe-hydride (OEP)Fe(NO)H product (Fig. 3.17). Importantly, the DFT-calculated ^{1}H NMR chemical shift of the hydride peak for (OEP)Fe(NO)H is at δ = –3.64 ppm, which is in good agreement with the experimentally observed value of δ = –4.11 ppm.

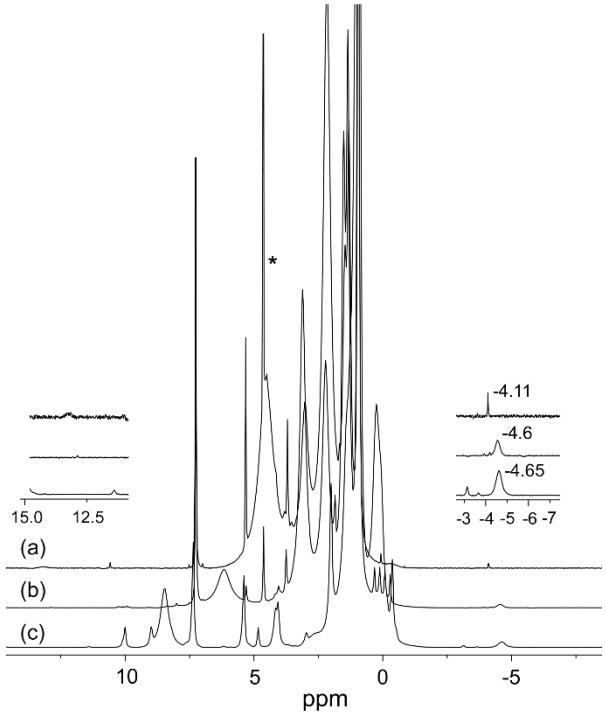

Figure 3.17. ^{1}H NMR spectra (in $CDCl_3$) of the reaction to generate (OEP)Fe(NO)H, highlighting the upfield and downfield regions of (a) (OEP)Fe(NO)H (top spectrum), (b) (OEP)Fe(H) byproduct (middle spectrum), and (c) (OEP)Fe(H) from the control reaction of [(OEP)Fe]OTf with hydride (bottom spectrum). The peak labeled * is due to the H_2 decomposition product (see text).

The calculated optimized geometry of the model (porphine)Fe(NO)H product reveals a core geometry not unlike that of the structurally characterized aryl derivative (OEP)Fe(NO)(C_6H_4F-*p*),[53] showing an off-axis tilt of the nitrosyl N-atom, a bent FeNO moiety (∠FeNO = 155.2°), and an asymmetry of the equatorial Fe–N(por) core displaying longer Fe–N(por) distances in the direction of the bent FeNO moiety (Fig. 3.18).

I also observed, on occasion, an additional broad peak at –4.6 ppm in the ^{1}H NMR spectrum (Fig. 3.17b). I attribute this latter peak to the non-nitrosyl paramagnetic (OEP)Fe(H) compound, probably resulting from dissociation of NO from the ferric $[(OEP)Fe(NO)]^{+}$ cation in solution prior to hydride attack. Indeed, a control experiment involving the reaction of $[(OEP)Fe]^{+}$ with borohydride reproduces this peak (Fig. 3.17c).

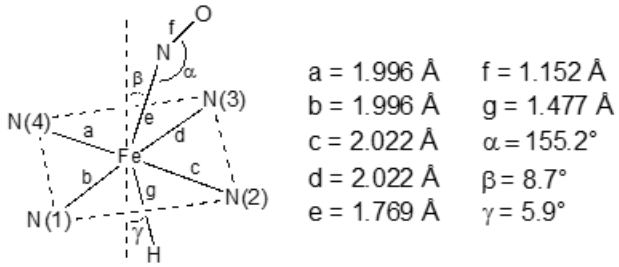

Figure 3.18. Selected geometrical parameters (in Å and degrees) for DFT-calculated (OEP)Fe(NO)H. The tilting angles are with respect to the axis normal to the four-nitrogen porphyrin plane.

The (OEP)Fe(NO)H product is very unstable even at −35 °C, with the Fe−H peak at −4.11 ppm in the ^{1}H NMR spectrum disappearing even after only ~15 mins. In fact, this peak is not detectable in the ^{1}H NMR experiments when the reaction is carried out at −20 °C. The (OEP)Fe(NO)H decomposition products are (OEP)Fe(NO) (87% total yield by IR) and H_2 (85% total yield by NMR). ^{11}B{^{1}H} NMR spectroscopy revealed that the boron-containing byproduct was diborane (Fig. 3.13b).

3.2.4.2 DFT calculations for the Fe(N−H)O versus (NO)Fe−H bond formations

DFT calculations were employed to provide insight into the differential Fe–H versus Fe(N−H)O bond-forming reactions (Scheme 3.4) when the five-coordinate [(porphine)Fe(NO)]$^{+}$ cation (**R1**) is reacted with borohydride (**R2**). The reaction path for the analogous six-coordinate compound [(porphine)Fe(NO)(5-MeIm)]$^{+}$ was shown previously in Scheme 3.1.[54] The "N path" in Scheme 3.4 represents an attack of hydride at the coordinated NO, and the "H path" represents direct Fe–H bond formation. The calculated electronic energies (ΔE), zero-point energy corrected electronic energies

(ΔE_{ZPE}), enthalpies (ΔH), and Gibbs free energy (ΔG) follow the same trends for the N- and the H-paths (Table 3.8).

Table 3.8. Relative energies with respect to reactants (in kcal/mol).

Pathway	System	ΔE_{SCF}	$\Delta E_{SCF+ZPE}$	ΔH	ΔG
	R1+R2	0.00	0.00	0.00	0.00
	I-1$_N$	−12.22	−10.71	−10.62	−1.33
N-Pathway	**TS$_N$**	−12.08	−11.04	−11.39	−1.08
	I-2$_N$	−49.69	−45.51	−46.25	−33.91
	P-1$_N$ + P2	−87.46	−79.42	−81.17	−69.04
H-Pathway	**R1+R2**	0.00	0.00	0.00	0.00
	I-1$_H$/I-2$_H$	−30.30	−28.58	−28.79	−18.90
	TS$_H$	−30.13	−28.78	−29.41	−18.51
	P-1$_H$+ P2	−59.92	−54.39	−55.98	−44.72

The first encounter intermediate in the N-path is represented by **I-1$_N$** in Scheme 3.4, with a distance of 2.984 Å between the nitrosyl N-atom and the hydride to be transferred. This distance shortens to 2.441 Å in the transition state **TS$_N$**, with an accompanying very slight lengthening of the bond between boron and the hydride to be transferred. In fact, the similarity of the B–H bond lengths in **TS$_N$** and the reagent **R2**, and the large difference (of 1.405 Å) in the N–H bond lengths between that in **TS$_N$** and the final Fe–HNO product **P-1$_N$** suggests an early transition state along the N-path, as observed also for the six-coordinate systems.[54]

The H-path first generates the intermediate I-1$_H$ with a distance of 1.594 Å (Scheme 3.4) between the Fe and the hydride to be transferred; this distance is much shorter than that seen in I-1$_N$, suggesting a stronger Fe···HBH$_3$ interaction in I-1$_H$ (H-path) than the N···HBH$_3$ interaction in I-1$_N$ (N-path). This trend is also maintained in both transition states TS$_N$ and TS$_H$. While the data for the N-path

suggests an early transition state, that for the H-path suggests a much later transition state. For example, for the H-path, the difference in the Fe–H distances between TS_H and P-1_H is only 0.115 Å (*c.f.*, the analogous difference in N–H dis-

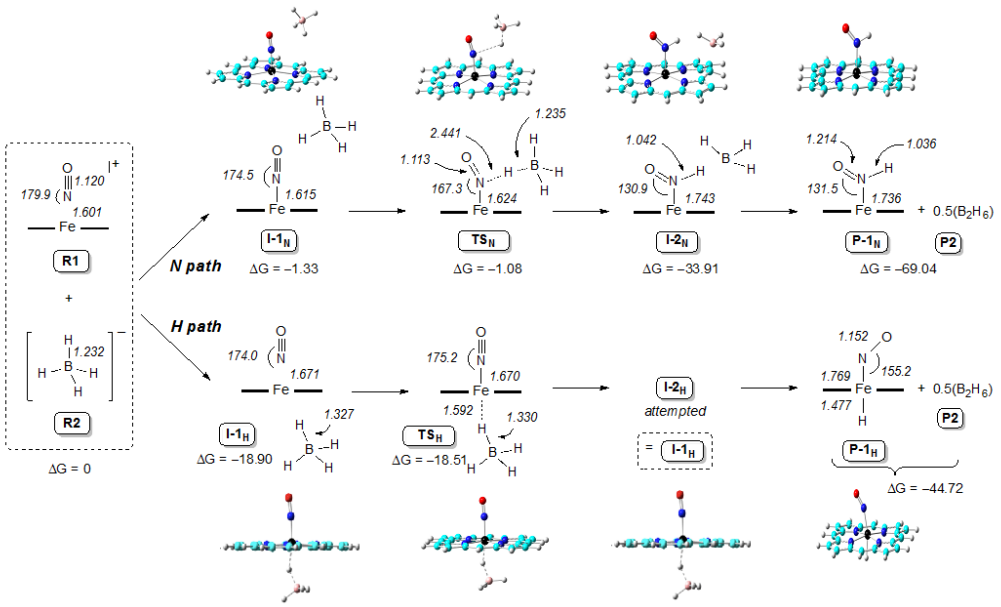

Scheme 3.4. DFT-calculated N- and H-pathways for hydride addition to the five-coordinate $[(P)Fe(NO)]^+$ cation.

tances of 1.405 Å along the N-path). Furthermore, the difference in the B–H (H to be transferred) bond distances in TS_H and in the initial reactant R2 is 0.098 Å, ~33x the noted difference along the related N-path. Attempts to locate a distinct second intermediate I-2_H, using a shorter Fe···H length and longer FeH···BH_3 distance (en route P-1_H), yielded the same I-1_H structure, probably due to the strong favorable electronic driving force between the ferric metal center and the hydride as discussed above, and the strong interaction between hydride and BH_3 (the B-H bond length difference between I-1_H/I-2_H and TS_H is only 0.003 Å).

Analysis of the data above shows that although both pathways of hydride attack on the five-coordinate $[(por)Fe(NO)]^+$ are thermodynamically favorable, the H-path is kinetically more favorable than the N-path by 17.43 kcal/mol (*i.e.*, $\Delta G|TS_H–TS_N|$), supporting the experimental formation of the Fe–H hydride complex with no observation of the Fe–HNO product. The charge analysis data is also consistent with the experimental and energy results; in the precursor cation $[(porphine)Fe(NO)]^+$ (R1), the Fe-atom bears a more positive charge (0.999e) than the nitrosyl N-atom (0.101e; *i.e.*, by ~9.9x), consistent with a more ready hydride transfer to Fe than N. In accordance with such a strong electronic driving force difference, and based on the charge differences in transition states and reactants, hydride transfer to Fe results in a donation of 0.652e from borohydride, while the hydride transfer to the nitrosyl N-atom results in a much smaller donation of 0.136e from borohydride.

3.3 Summary and Conclusions

As shown in this chapter, I have prepared a series of pure and very stable six-coordinate $\{FeNO\}^6$ complexes that were amenable to further reactivity studies to generate the once-elusive Fe−HNO species. Low temperature reactions of these compounds with borohydride afforded the formation of ferrous Fe−HNO derivatives as revealed by IR and ^1H NMR spectroscopy, coupled with DFT calculations. These FeHNO compounds exhibit varied decomposition pathways; (i) one involving H_2 gas and Fe−NO formation from Fe(N−H)O bond cleavage, and (ii) the other involving Fe−N(H)O bond cleavage forming N_2O gas and H_2O.

Importantly, reactions of FeHNO species with external NO generates N_2O gas, modeling for the first time, the critical N−N bond formation step catalysed by the fungal cyt P450nor enzyme.

Differential reactivity of six- vs. five-coordinate ferric nitrosyls was also systematically investigated. Low temperature reactions of five-coordinate $\{FeNO\}^6$ species with borohydride afforded the formation of the elusive (NO)Fe-H species as evidenced in IR and ^1H NMR spectroscopy with the aid of DFT calculations. This compound decomposes to form H_2 gas and the known five-coordinate (OEP)Fe(NO).

Vertical advances from this work can be summarized as follows:

(i) First experimental spectroscopic (IR and ^1H NMR) evidence of the hydride attack on bound heme-model ferric nitrosyls mimicking the formation of the proposed Fe−HNO active intermediate in NO to N_2O biotransformation by P450nor.

(ii) Reactivity of this synthetic heme-model FeHNO species with external NO to yield N_2O gas via a N−N coupling reaction step supports the proposed FeHNO species as an active intermediate in the NO reduction by fungal P450nor. This is the first unambiguous experimental evidence for this key critical N−N bond forming step employed by nature during NO detoxification.

(iii) This very challenging work provides fundamental information that would lead to successful nucleophilic reactions of hydride on a

coordinated NO^+ (in the six coordinate $\{FeNO\}^6$ case) versus the metal center (in the five coordinate $\{FeNO\}^6$ case).

3.4 Experimental Section

The reactions were performed anaerobically using nitrogen as the inert gas. Air-sensitive samples and reagents were handled inside a glove box, and all reactions were performed using Schlenk glassware. Solvents used in the reactions were collected under nitrogen from a Pure Solv 400-5-MD Solvent Purification System (Innovative Technology) or distilled from appropriate drying agents under an atmosphere of nitrogen.

3.4.1 Chemicals

The free base porphyrin $(TTP)H_2$[55] was synthesized as described in the literature. The related $(OEP)H_2$, $(PPDME)H_2$, and (PPDME)FeCl compounds were purchased from Mid-century Chemicals and used as received. The metalloporphyrins (por)FeCl (por = OEP, TTP)[56] were prepared according to published procedures. The [(por)Fe]OTf precursors (por = OEP, PPDME, TTP) were prepared in a similar manner as described for $[(OEP)Fe]ClO_4$ with slight modifications.[57] Silver triflate ($AgCF_3SO_3$, 99%), tetrabutylammonium borohydride ($[NBu_4]BH_4$, 98%), 5-methylimidazole (5-MeIm, ≥99%), 1-methylimidazole (1-MeIm, ≥99%), 1-ethylimidazole (1-EtIm, ≥99%), imidazole (Im, ≥99%), and triphenylphosphine (PPh_3, 99%) were purchased from Sigma-Aldrich and were used as received. Deuterated tetrabutylammonium borodeuteride ($[NBu_4]BD_4$) was prepared by a literature method.[58] Chloroform-*d* ($CDCl_3$, 99.96 %D) was purchased from Cambridge Isotopes, deaerated by three freeze-pump-thaw cycles,

and stored over molecular sieves. Natural abundance nitric oxide (NO) gas was passed through a KOH column, then through a cold trap prior to its contact with the precursor solution to avoid the introduction of NO_x impurities. Labeled ^{15}NO (Icon Isotope Inc., 99% ^{15}N) and $^{15}N^{18}O$ (Icon Isotope Inc., 99% ^{15}N, and 95% ^{18}O) were used as received without further purification.

3.4.2 Instrumentation/Spectroscopy

FT-IR spectra were collected using a Bruker Tensor 27 spectrometer equipped with a mid-IR fiber optic dip probe and liquid N_2 cooled MCT detector (RemSpec Corporation, Sturbridge, MA). UV-vis spectra were collected using a Hewlett-Packard 8453 diode array instrument (model 8453). ^1H NMR spectroscopy experiments for Fe-HNO and Fe-H detection were carried out using a 400 MHz Varian NMR spectrometer at −20°C and −50°C, respectively. Boron-containing by-products from the reactions of six- and five-coordinate $\{FeNO\}^6$ species with $[NBu_4]BH_4$ were determined by $^{11}B\{^1H\}$ NMR experiments performed at 128 MHz. ESI mass spectra were recorded on a high resolution Micromass Q-TOF mass spectrometer operated by Dr. Steve Foster. A Shimadzu GC-8A gas chromatograph equipped with a thermal conductivity detector (TCD) and fitted with 50/80 Porapak Q (2m x 1/8 in) column was used to confirm the formation of H_2 gas in the reaction mixture (a collaboration with Dr. Tanner, OU Department of Microbiology and Plant Biology). GC conditions: Tank pressure of 22 psi; inj/det temperature set at 110 °C; column temperature of 100 °C; at a current of 100 mA. The GC instrument was pre-calibrated using two $H_2/CO_2/N_2$ mixtures of known compositions. Elemental analyses were performed by Atlantic Microlab Inc., Norcross,

GA. X-ray diffraction experiments were performed by Dr. Douglas R. Powell using a Bruker diffractometer fitted with an APEX ccd area detector, and graphite monochromated Mo Kα radiation (λ = 0.71073 Å). Density Functional Theory (DFT) calculations for probing the hydride attack at the bound−NO group in the six- and five-coordinate {FeNO}^{6} compounds to form the Fe−HNO and (NO)Fe−H derivatives, respectively, were performed by our collaborator Dr. Yong Zhang at the Stevens Institute of Technology (SIT) in New Jersey.

3.4.3 Syntheses

3.4.3.1 Preparation of the six-coordinate [(por)Fe(NO)(L)]OTf complexes

The six-coordinate {FeNO}^{6} complexes were prepared by bubbling NO gas into a CH_2Cl_2 solution of the [(por)Fe]OTf precursors in the presence of an *N*-base ligand L (L = 5-MeIm, 1-MeIm, 1-EtIm, and Im). The following are representative reactions. The PPDME (except with 5-MeIm *trans* ligand) and TTP derivatives of the six-coordinate ferric nitrosyls were prepared *in situ* followed by immediate reactivity studies with the hydride reagent.

[(OEP)Fe(NO)(5-MeIm)]OTf (1). To a CH_2Cl_2 (5 mL) solution of [(OEP)Fe]OTf[57] (16.8 mg, 0.023 mmol) was added 5-MeIm (2.1 mg, 0.025 mmol) followed by NO gas, in a manner similar to that used to prepare other crystalline [(por)Fe(NO)(*N*-ligand)]$^+$ complexes.[19] X-ray quality crystals of the product [(OEP)Fe(NO)(5-MeIm)]OTf (10.1 mg, 52% isolated yield based on the [(OEP)Fe]OTf precursor) were obtained from its CH_2Cl_2/*n*-hexane solution kept at 0 ˚C. Anal. Calcd for $C_{41}H_5F_3FeN_7O_4S\bullet0.5CH_2Cl_2$: C, 55.86; H, 5.76; N, 10.99; S, 3.59. Found: C, 56.84; H,

5.98; N, 10.93; S, 3.40. Solution IR (CH_2Cl_2): ν_{NO} = 1910 cm^{-1} (ν^{15}_{NO} = 1874 cm^{-1}); IR (KBr): ν_{NO} = 1895 cm^{-1}; characteristic bands of an uncoordinated triflate anion: $\nu_{as}(SO_3)$ = 1295 cm^{-1}, $\nu_s(CF_3)$ = 1225 cm^{-1}, $\nu_s(SO_3)$ = 1022 cm^{-1} in addition to porphyrin signals.[59] UV-vis (CH_2Cl_2): λ_{max} = 411, 526, 558 nm.[19] ^{1}H NMR ($CDCl_3$, −20 °C, 400 MHz; δ, ppm): 10.19 (s, 4H, methine C−*H*), 9.25 (s, 1H, 5-MeIm N−*H*), 7.26 (s, $CHCl_3$), 5.32 (s, CH_2Cl_2), 4.13 (overlapping q, 16H, ethyl-CH_2), 1.97(t, $J_{H\text{-}H}$ = 7.6 Hz, 24H, ethyl-CH_3), 1.68 (s, H_2O), 1.23 and 0.86 (*n*-hexane impurity), 0.45 (s, 3H, 5-MeIm-CH_3), 0.22 (s, 1H, 5-MeIm-H), −0.77 (s, 1H, 5-MeIm-H). High resolution ESI mass spectrum of [(OEP)Fe(NO)(5-MeIm)]OTf: positive (+) mode, *m/z* of $[(OEP)Fe(5\text{-}MeIm]^+$ = 670.3447, *m/z* of $[(OEP)Fe]^+$ = 588.2916; and negative (−) mode, *m/z* of $[OSO_2CF_3]^-$ = 148.9520.

[(OEP)Fe(NO)(1-MeIm)]OTf (2). This compound was prepared in 47% isolated yield in a similar manner to that described for compound **1** above. IR (CH_2Cl_2): ν_{NO} = 1914 cm^{-1} (ν^{15}_{NO} = 1877 cm^{-1}); IR (KBr): ν_{NO} = 1888 cm^{-1} (ν^{15}_{NO} = 1852 cm^{-1}); characteristic bands of an uncoordinated triflate anion: $\nu_{as}(SO_3)$ = 1285 cm^{-1}, $\nu_s(CF_3)$ = 1223 cm^{-1}, $\nu_s(SO_3)$ = 1021 cm^{-1} in addition to porphyrin vibrational signals.[59] UV-vis (CH_2Cl_2): λ_{max} = 410, 526, 558 nm.[19] ^{1}H NMR ($CDCl_3$, −20 °C, 400 MHz; δ, ppm): 10.23 (s, 4H, methine C−*H*), 7.26 (s, $CHCl_3$), 5.32 (s, CH_2Cl_2), 4.60 (s, 1H, 1-MeIm-H), 4.10 (overlapping q, 16H, ethyl-CH_2), 1.96 (t, $J_{H\text{-}H}$ = 7.6 Hz, 24H, ethyl-CH_3), 1.92 (s, 3H, 1-MeIm-CH_3), 1.23 and 0.86 (*n*-hexane impurity), 0.16 (s, 1H, 1-MeIm-H), −0.42 (s, 1H, 1-MeIm-H). Compound **2** was successfully crystallized in a CH_2Cl_2/*n*-hexane solution at 0 ˚C.

[(OEP)Fe(NO)(Im)]OTf (3). This imidazole-ligated {FeNO}^{6} derivative was prepared in a similar manner to that described for compound **1** above and the product was isolated in 70% yield. IR (CH_2Cl_2): ν_{NO} = 1910 cm^{-1} (ν^{15}_{NO} = 1873 cm^{-1}); IR (KBr): ν_{NO} = 1906 and 1890 cm^{-1} (ν^{15}_{NO} = 1866 and 1854 cm^{-1}); characteristic bands of an uncoordinated triflate anion: ν_{as} (SO_3) = 1285 cm^{-1}, ν_s (CF_3) = 1223 cm^{-1}, ν_s (SO_3) = 1021 cm^{-1} in addition to porphyrin vibrational signals.[59] UV-vis (CH_2Cl_2): λ_{max} = 403, 524, 558 nm.[19] ^{1}H NMR ($CDCl_3$, −20 °C, 400 MHz; δ, ppm): 10.22 (s, 4H, methine C−*H*), 9.53 (s, 1H, Im N−*H*), 7.26 (s, $CHCl_3$), 5.32 (s, CH_2Cl_2), 4.14 (overlapping q, 16H, ethyl-CH_2), 1.97 (t, $J_{H\text{-}H}$ = 7.6 Hz, 24H, ethyl-CH_3), 1.23 and 0.86 (*n*-hexane impurity), 0.40 (s, 1H, Im-H), −0.41 (s, 1H, Im-H), −1.13 (s, 1H, Im-H). X-ray quality crystals of the product [(OEP)Fe(NO)(Im)]OTf were obtained from its CH_2Cl_2/*n*-hexane solution kept at 0 ˚C.

[(OEP)Fe(NO)(1-EtIm)]OTf (4). The 1-ethylimidazole (1-EtIm)-ligated {FeNO}^{6} derivative **4** was prepared in 63% isolated yield in a similar manner to that used to prepare compound **1**. IR (CH_2Cl_2): ν_{NO} = 1912 cm^{-1} (ν^{15}_{NO} = 1874 cm^{-1}); IR (KBr): ν_{NO} = 1908 cm^{-1}; characteristic bands of an uncoordinated triflate anion: ν_{as} (SO_3) = 1285 cm^{-1}, ν_s (CF_3) = 1223 cm^{-1}, ν_s (SO_3) = 1021 cm^{-1} in addition to porphyrin vibrational signals.[59] UV-vis (CH_2Cl_2): λ_{max} = 411, 526, 558 nm.[19] ^{1}H NMR ($CDCl_3$, −20 °C, 400 MHz; δ, ppm): 10.24 (s, 4H, methine C−*H*), 7.26 (s, $CHCl_3$), 5.32 (s, CH_2Cl_2), 4.61 (s, 1H, 1-EtIm-H), 4.15 (overlapping q, 16H, ethyl-CH_2), 2.19 (q, 2H, 1-EtIm-CH_2) 1.96 (t, $J_{H\text{-}H}$ = 7.6 Hz, 24H, ethyl-CH_3), 1.49 (s, H_2O), 1.24 and 0.86 (*n*-hexane impurity), 0.11 (s, 1H, 1-EtIm-H), −0.04 (t, 3H, 1-EtIm-CH_3), −0.36 (s, 1H, 1-EtIm-H). The product [(OEP)Fe(NO)(1-EtIm)]OTf was successfully crystallized from its CH_2Cl_2/*n*-heptane solution kept at 0 ˚C.

[(PPDME)Fe(NO)(5-MeIm)]SbF_6 (5). A CH_2Cl_2 (5 mL) solution of [(PPDME)Fe]SbF_6 (13.8 mg, 0.016 mmol) containing 1 equiv of 5-MeIm (1.3 mg, 0.016 mmol) was stirred for 2 h, followed by the introduction of NO gas, in a similar manner to that used to prepare compound **1**. X-ray diffraction-quality crystals of the product [(PPDME)Fe(NO)(5-MeIm)]SbF_6 (9.0 mg, 58% isolated yield based on Fe) were obtained from a mixed CH_2Cl_2/methanol solvent under an NO atmosphere. IR (KBr): ν_{NO} = 1905 cm^{-1}. Characteristic band of an uncoordinated hexafluoroanti-monate: $\nu_{Sb\text{-}F}$ = 659 cm^{-1}.[60]

3.4.3.2 Preparation of five-coordinate [(OEP)Fe(NO)]OTf

The following procedure is representative for the preparation of [(OEP)Fe(NO)]OTf. NO gas was introduced to a CH_2Cl_2 (5 mL) solution of [(OEP)Fe]OTf (10.7 mg, 0.015 mmol).[57] X-ray quality crystals of the product [(OEP)Fe(NO)]OTf (6.7 mg, 61% isolated yield based on [(OEP)Fe]OTf) were obtained from its CH_2Cl_2/*n*-hexane solution under an NO atmosphere. IR (KBr): ν_{NO} = 1856, 1841 cm^{-1}.

3.4.4 Reactions of the Six-coordinate {FeNO}^{6} Complexes with Hydride

3.4.4.1 Reactions of the six-coordinate [(por)Fe(NO)(L)]OTf complexes with hydride to form (por)Fe(HNO)L derivatives (por = OEP, PPDME, TTP; L = 5-MeIm, 1-MeIm, Im)

Below is a representative procedure describing the preparation of the elusive (por)Fe(HNO)L complexes from the reactions of the [(por)Fe(NO)(L)]OTf compounds with hydride. Important characteristic reactions (*e.g.*, phosphine trapping experiments),

spectroscopy (*e.g.*, ^{1}H and ^{11}B{^{1}H} NMR, IR), and mass spectrometric characterizations to confirm the formation of (por)Fe(HNO)L product are also discussed. The other (por)Fe(HNO)L products are prepared in the same manner as described for the preparation of (OEP)Fe(HNO)(5-MeIm).

Preparation of (OEP)Fe(HNO)(5-MeIm). To a $CDCl_3$ (1.5 mL) solution of compound **1** (9.5 mg, 0.011 mmol) in a J. Young NMR tube at −20 °C was added a $CDCl_3$ (0.2 mL) solution of $[NBu_4]BH_4$ (4.5 mg, 0.017 mmol). The ^{1}H NMR spectrum was recorded immediately. The ^{1}H NMR signal at 13.99 ppm (s) assigned to bound Fe-HNO integrates to 11% yield against a C_6H_6 internal standard. The characteristic NO stretching frequency of the (OEP)Fe(HNO)(5-MeIm) complex was obtained from a separate reaction in $CHCl_3$ at −45°C. Solution IR: ν_{NO} = 1383 cm^{-1} ($\nu_{^{15}NO}$ = 1360 cm^{-1}). This signal decreases with concomitant increase of a band at 1668 cm^{-1} assigned to the ν_{NO} of the known (OEP)Fe(NO) (85% yield by solution IR based on the precursor [(OEP)Fe(NO)(5-MeIm)]OTf). The boron-containing by-product was determined to be diborane (B_2H_6) by ^{11}B{^{1}H} NMR spectroscopy in a quartz J. Young NMR tube, identified by comparison with a spectrum from the known diborane-producing reaction (*e.g.*, reaction of $[NBu_4]BH_4$ with 1,2-dichloroethane).[46]

Reaction of (OEP)Fe(HNO)(5-MeIm) with PPh$_3$. To the *in situ* generated (OEP)Fe(HNO)(5-MeIm) in $CHCl_3$ at −20 °C was added excess PPh_3, and the resulting mixture was stirred for 5 min at this temperature. The reacting solution was warmed slowly to room temperature and stirred for another 30 min. High resolution ESI mass spectra of the product mixture: *m/z* of $[HN{=}PPh_3]^+$ = 278.1101 (expected 278.1099), *m/z* of $[O{=}PPh_3]^+$ = 279.0937 (expected 279.0939).

Detection of H_2 from the decomposition of (OEP)Fe(HNO)(5-MeIm). The headspace atmosphere of the reaction mixture to generate (OEP)Fe(HNO)(5-MeIm) was collected after warming the mixture to room temperature. The headspace gases were then injected into pre-cooled $CDCl_3$ and the ^1H NMR spectrum was recorded. ^1H NMR (δ, ppm): 7.26 (*s*, $CHCl_3$), 4.62 (s, dissolved H_2 gas).[50] These data matched the H_2 signal of an authentic commercial sample of 5% H_2/N_2. The identity of H_2 was further confirmed by gas chromatography (GC), by injection of 30 μL of the headspace gas using an air-tight syringe into a Shimadzu gas chromatograph (GC-8A) equipped with thermal conductivity detector (TCD) and fitted with 50/80 Porapak Q (2m x 1/8 in) column.

Detection of N_2O from the decomposition of (OEP)Fe(DNO)(5/1-MeIm). The headspace atmosphere of the reaction mixture to generate (OEP)Fe(DNO)(5/1-MeIm) was vacuum transferred to an IR gas cell (10 cm pathlength) after warming the mixture to room temperature. IR (gas phase): ν_{as} (N_2O) = 2237/2213 ($^{15}N_2O$ = 2167/2145) cm^{-1}. ^2H NMR: δ = 2.2 ppm assigned to D_2O which was confirmed by spiking the sample with authentic D_2O. In a separate reaction, formation of the known five-coordinate (OEP)Fe(NO) (solution ν_{NO} = 1665 cm^{-1}) was also formed during the decomposition of (OEP)Fe(DNO)(5/1-MeIm).

3.4.4.2 Reactions of the (OEP)Fe(HNO)(5/1-MeIm) complexes with external NO

(a) $^{15}N^{18}O$ gas was introduced to a CH_2Cl_2 (3 mL) solution of the *in-situ* prepared (OEP)Fe(HNO)(5-MeIm) at −95 °C in a sealed Schlenk tube. The reaction mixture was stirred for 10 min at this temperature. The solution was then slowly warmed to room temperature and stirred for an additional 30 min. The headspace atmosphere was vacuum

transferred to a gas IR cell (10 cm path length). IR (gas phase): in addition to the bands due to singly labeled N-atom of N_2O gases; N_2O = 2237/2213 cm^{-1} and $^{15}N_2{}^{18}O$ = 2160/2137 cm^{-1}, new bands were observed to have formed at 2185/2162 cm^{-1} (the latter band overlaps with the $^{15}N_2{}^{18}O$ signal) assigned to $^{14}N^{15}N^{18}O$.[51]

(b) A separate reaction of (OEP)Fe($H^{15}N^{18}O$)(5-MeIm) with NO was also conducted in a similar manner described above. IR (gas phase): in addition to the bands due to singly labeled N-atom of N_2O gases, new bands were formed at 2195/2169 cm^{-1} assigned to $^{15}N^{14}N^{16}O$.[51]

(c) To determine which N−O bond was cleaved in these reactions, I conducted a control experiment to verify the formation of $^{15}N^{14}N^{16}O$ from different isotope combinations. In a similar manner, I conducted a coupling reaction of (OEP)Fe($H^{15}NO$)(5-MeIm) with unlabeled NO. Gas phase IR spectroscopy showed formation of the same new bands as those from the reaction of (OEP)Fe($H^{15}N^{18}O$)(5-MeIm) with NO. IR (gas phase): in addition to the bands due to singly labeled N-atom of N_2O gases, new bands were formed at 2195/2169 cm^{-1} assigned to $^{15}N^{14}N^{16}O$.[51]

3.4.5 Reactions of the Five-coordinate {FeNO}^{6} Complexes with Hydride

Below is a representative procedure describing the formation of a very unstable (OEP)Fe(NO)H product from the reaction of [(OEP)Fe(NO)]OTf with hydride. Spectroscopic characterizations (*e.g.*, low temperature ^1H and $^{11}B\{^1H\}$ NMR, and IR spectroscopy) and several control experiments to confirm the formation of the (OEP)Fe(NO)H product are also described.

Preparation of (OEP)Fe(NO)H. To a $CDCl_3$ (0.5 mL) solution of [(OEP)Fe(NO)]OTf (7.9 mg, 0.013 mmol)[61] in a J. Young NMR tube at −50 °C was added a $CDCl_3$ (0.2 mL) solution of $[NBu_4]BH_4$ (6.0 mg, 0.02 mmol). The ^1H NMR spectra were recorded immediately. ^1H NMR (−50° C, 400 MHz; δ, ppm): −4.11 (sharp s, (NO)Fe−H). $^{11}B\{^1H\}$ NMR spectra (0° C, 128 MHz; δ, ppm): −26 (br s, assigned to B_2H_6). This was further confirmed by comparing with the spectrum of a diborane from a known reaction (*e.g.*, $[NBu_4]BH_4$ with 1,2-dichloroethane).[46]

Thermal decomposition of (OEP)Fe(NO)H. IR and ^1H NMR spectroscopy were utilized to monitor the decomposition of (OEP)Fe(NO)H detected in the product mixture from the reaction of [(OEP)Fe(NO)]OTf with $[NBu_4]BH_4$. The IR spectrum was recorded after warming the product mixture to room temperature for 0.5 h. IR ($CHCl_3$): ν_{NO} = 1668 cm^{-1}. ^1H NMR (−50° C, 400 MHz; δ, ppm): 4.62 ppm assigned to the H_2 by-product of the decomposition.[50]

3.4.6 X-ray Crystallography

Intensity data for the crystals at 100(2) K were collected using a diffractometer with a Bruker APEX CCD area detector[62,63] using graphite-monochromated Mo Kα radiation (λ = 0.71073 Å). The crystal and refinement data are collected in Table 3.9.

Table 3.9. Crystallographic collection and refinement parameters.

Complex	1	2	3	4	5
Empirical formula (fw)	$[C_{40}H_{50}FeN_7O]CF_3SO_3 \bullet CH_2Cl_2$ (892.25)	$[C_{40}H_{50}FeN_7O]CF_3SO_3$ (849.79)	$[C_{41}H_{52}FeN_7O]CF_3SO_3$ (863.81)	$[C_{39}H_{48}FeN_7O]CF_3SO_3$ (835.76)	$[(C_{40}H_{42}FeN_7O_5) \bullet 0.5(C_4H_7N_2)]1.5SbF_6$
Crystal system, space group	triclinic, $P\bar{1}$	triclinic, $P\bar{1}$	triclinic, $P\bar{1}$	triclinic, $P\bar{1}$	triclinic, $P\bar{1}$
Unit cell dimensions					
a (Å)	8.8510(9)	12.1406(12)	9.4390(10)	13.643(2)	12.0338(10)
b (Å)	15.6741(16)	13.9664(14)	13.1091(14)	13.683(2)	14.0169(12)
c (Å)	15.9474(16)	14.0395(14)	17.3768(19)	13.834(2)	16.3482(14)
α (°)	98.2007(15)	113.7661(13)	89.699(2)	115.498(3)	67.9924(14
β (°)	105.5290(15)	90.3387(15)	85.877(2)	98.492(3)	68.7999(14)
γ (°)	93.3465(16)	111.9136(14)	71.607(2)	99.421(3)	64.7066(14)
Volume (Å^3)	2099.0(4)	1986.7(3)	2034.7(4)	2229.4(6)	2244.7(3)
Z, Z'	2, 1	2, 1	2, 1	2, 1	2,1
F(000)	934	892	908	876	1154
Absorption coefficient(mm^{-1})	0.537	0.498	0.487	0.443	1.311
Max. and min. trans.	0.822 and 0.757	0.894 and 0.869	0.892 and 0.836	0.957 and 0.816	0.925 and 0.779
Theta range (°)	1.319 to 27.497	1.612 to 27.514	1.175 to 26.000	1.561 to 26.455	1.384 and 25.902
Reflections collected	36273	64351	18097	36280	68484
Independent reflections	9360 [R(int) = 0.0481]	9112 [R(int) = 0.0218]	18097[R(int) = 0.0429]	36280[R(int) = 0.0492]	16006[R(int) = 0.0417]
Data/restraints/parameters	9360/0/545	9112/0/514	18097/358/626	9158/1/508	16006/1337/751
$wR(F^2$ all data) [a]	$wR2$ = 0.1073	$wR2$ = 0.0904	$wR2$ = 0.1257	$wR2$ = 0.1571	$wR2$ = 0.1854
$R(F$ obsd data) [b]	$R1$ = 0.0383	$R1$ = 0.0300	$R1$ = 0.0442	$R1$ = 0.0473	$R1$ = 0.0646
Goodness-of-fit on F^2	0.982	0.974	1.005	1.010	1.010
Observed data [$I > 2\sigma(I)$]	7918	8157	15802	6959	11046
Largest and mean shift / s.u.	0.001and 0.000	0.001 and 0.000	0.0013 and 0.000	0.000 and 0.000	0.000 and 0.000
Largest diff. peak and hole (e/Å^3)	0.820 and –0.461	0.425 and –0.0406	0.528 and −0.668	1.064 and −0.606	1.234 and −0.560

3.4.7 Density Functional Theory (DFT) Calculations

These calculations were done by our collaborator, Dr. Yong Zhang (PI) and his student Dr. Rahul Khade at the Stevens Institute of Technology in New Jersey.

All calculations were done using the program Gaussian 09.[64] Full geometry optimizations were conducted for all studied chemical species with subsequent frequency calculations to verify the nature of the corresponding stationary states on their potential energy surfaces and provide zero-point energy corrected electronic energies, enthalpies, and Gibbs free energies.

In the case of ^{1}H NMR chemical shifts and NO vibrational frequencies calculations, the geometries were optimized using the mPW1PW91[65] method and the NMR properties were calculated using the B3LYP[66] method with solvent ($CHCl_3$) effect included using the PCM formalism,[67-70] similar to the approach used previously to study ^{1}H NMR chemical shifts in various organometallic complexes.[49] The basis sets used in the geometry optimizations were Wachters' basis[71] for iron, 6-311++G(2d,2p) for 1st shell atoms (atoms bonded to iron, HNO, and BH_3/B_2H_6), and 6-31G(d) for other atoms. Similar basis sets were used for the NMR calculation except the use of LanL2DZ[72] basis for Fe. The calculated NO frequencies of various iron porphyrin systems studied in this work were scaled using the experimental/computational NO frequency (1380/1568) for a related HNO Ru porphyrin system.[13] The atomic charges were calculated using the Merz-Singh-Kollman scheme[73] as implemented in Gaussian 09.

For the reaction pathway calculations, three sets of methods were used together with the above geometry optimization basis sets. In the first two sets of calculations, the hybrid HF-DFT method mPW1PW91[65] and the pure DFT method mPWVWN[65,74] were

used in full geometry optimization and frequency analysis with the experimental chloroform solvent effect included using the PCM formalism.[67-70] For the third set of calculations, the dispersion effect corrected B3LYP-D3[75] method was used to perform single point energy calculations of the mPWVWN optimized structures and generated corrected energy results.

The energy trends observed for mPW1PW91, mPWVWN, and B3LYP-D3 methods obtained for N- and O-pathways are basically the same, with the formation of HNO complex being of lower Gibbs free energies of activation by ~16-19 kcal/mol and lower Gibbs free reaction energy by ~17−20 kcal/mol than the formation of NOH complex. The discussion was focused on the data generated using mPW1PW91 method.

Since the O-pathway product could have additional conformations with H in NOH pointing to or away from porphyrin ring and with NO *cis* or *trans* to the Me group in the axial ligand, these different conformations were studied and the lowest energy one was used to compare with the N-pathway product formation. The (por)Fe^{II}(5-MeIm)(NOH_{Down}) structure is more stable than the (por)Fe^{II}(5-MeIm)(NOH_{up}) conformation by 3.76 kcal/mol in Gibbs free energy, which is in good agreement with previous computational investigation of these two conformations.[16] However, this (por)Fe^{II}(5-MeIm)(NOH_{Down}) with a *trans* NO/Me orientation is slightly less stable than a conformation with the *cis* NO/Me orientation by 0.31 kcal/mol. Therefore, the *cis* conformation was used as the lowest energy conformation for the NOH product (**P-1$_O$**).

3.5 References

1. Miranda, K. M. *Coord. Chem. Rev.* **2005**, *249*, 433-455.

2. Daiber, A., Shoun, H., and Ullrich, V. *J. Inorg. Biochem.* **2005**, *99*, 185-193.

3. Kramos, B., Menyhard, D. K., and Olah, J. *J. Phys. Chem. B* **2012**, *116*, 872-885.

4. Einsle, O., Messerschmidt, A., Huber, R., Kroneck, P. M. H., and Neese, F. *J. Am. Chem. Soc.* **2002**, *124*, 11737-11745.

5. Bykov, D. and Neese, F. *Inorg. Chem.* **2015**, *54*, 9303-9316.

6. Cabail, M. Z., Kostera, J., and Pacheco, A. A. *Inorg. Chem.* **2005**, *44*, 225-231.

7. Kumar, M. R., Pervitsky, D., Chen, L., Poulos, T., Kundu, S., Hargrove, M. S., Rivera, E. J., Diaz, A., Colon, J. L., and Farmer, P. J. *Biochemistry* **2009**, *48*, 5018-5025.

8. Farmer, P. J. and Sulc, F. *J. Inorg. Biochem.* **2005**, *99*, 166-184.

9. Doctorovich, F., Bikiel, D., Pellegrino, J., Suarez, S. A., Larsen, A., and Marti, M. A. *Coord. Chem. Rev.* **2011**, *255*, 2764-2784.

10. Choi, I.-K., Liu, Y., Feng, D., Paeng, K.-J., and Ryan, M. D. *Inorg. Chem.* **1991**, *30*, 1832-1839.

11. Barley, M. H., Takeuchi, K. J., and Meyer, T. J. *J. Am. Chem. Soc.* **1986**, *108*, 5876-5885.

12. Goodrich, L. E., Roy, S., Alp, E. E., Zhao, J. Y., Hu, M. Y., and Lehnert, N. *Inorg. Chem.* **2013**, *52*, 7766-7780.

13. Lee, J. and Richter-Addo, G. B. *J. Inorg. Biochem.* **2004**, *98*, 1247-1250.

14. Sellmann, D., Gottschalk-Gaudig, T., Haussinger, D., Heinemann, F. W., and Hess, B. A. *Chem. Eur. J.* **2001**, *7*, 2099-2103.

15. Speelman, A. L. and Lehnert, N. *Acc. Chem. Res.* **2014**, *47*, 1106-1116.

16. Linder, D. P. and Rodgers, K. R. *Inorg. Chem.* **2005**, *44*, 8259-8264.

17. Riplinger, C., Bill, E., Daiber, A., Ullrich, V., Shoun, H., and Neese, F. *Chem.-Eur. J.* **2014**, *20*, 1602-1614.

18. Zhang, Y. *J. Inorg. Biochem.* **2013**, *118*, 191-2000, and references therein.

19. Ellison, M. K. and Scheidt, W. R. *J. Am. Chem. Soc.* **1999**, *121*, 5210-5219.

20. Quinn, R., Mercersmith, J., Burstyn, J. N., and Valentine, J. S. *J. Am. Chem. Soc.* **1984**, *106*, 4136-4144.

21. Ellison, M. K., Schultz, C. E., and Scheidt, W. R. *J. Am. Chem. Soc.* **2002**, *124*, 13833-13841.

22. Ellison, M. K. and Scheidt, W. R. *J. Am. Chem. Soc.* **1999**, *121*, 5210-5219.

23. Scheidt, W. R., Lee, Y. J., and Hatano, K. *J. Am. Chem. Soc.* **1984**, *106*, 3191-3198.

24. Yi, G.-B., Chen, L., Khan, M. A., and Richter-Addo, G. B. *Inorg. Chem.* **1997**, *36*, 3876-3885.

25. Ellison, M. K., Schulz, C. E., and Scheidt, W. R. *Inorg. Chem.* **1999**, *38*, 100-108.

26. Xu, N., Powell, D. R., Cheng, L., and Richter-Addo, G. B. *Chem. Commun.* **2006**, 2030-2032.

27. Suzuki, N., Higuchi, T., Urano, Y., Kikuchi, K., Uchida, T., Mukai, M., Kitagawa, T., and Nagano, T. *J. Am. Chem. Soc.* **2000**, *122*, 12059-12060.

28. Hu, S. and Kincaid, J. R. *J. Am. Chem. Soc.* **1991**, *113*, 2843-2853.

29. Obayashi, E., Tsukamoto, K., Adachi, S.-i., Takahashi, S., Nomura, M., Iizuka, T., Shoun, H., and Shiro, Y. *J. Am. Chem. Soc.* **1997**, *119*, 7807-7816.

30. Hu, S. and Kincaid, J. R. *J. Biol. Chem.* **1993**, *268*, 6189-6193.

31. Benko, B. and Yu, N.-T. *Proc. Natl. Acad. Sci. U.S.A.* **1983**, *80*, 7042-7046.

32. Tomita, T., Haruta, N., Aki, M., Kitagawa, T., and Ikeda-Saito, M. *J. Am. Chem. Soc.* **2001**, *123*, 2666-2667.

33. Pinakoulaki, E., Gemeinhardt, S., Saraste, M., and Varotsis, C. *J. Biol. Chem.* **2002**, *277*, 23407-23413.

34. Miller, L. M., Pedraza, A. J., and Chance, M. R. *Biochemistry* **1997**, *36*, 12199-12207.

35. Wang, Y. and Averill, B. A. *J. Am. Chem. Soc.* **1996**, *118*, 3972-3973.

36. Ding, X. D., Weichsel, A., Andersen, J. F., Shokhireva, T. K., Balfour, C., Pierik, A. J., Averill, B. A., Montfort, W. R., and Walker, F. A. *J. Am. Chem. Soc.* **1999**, *121*, 128-138.

37. Maes, E. M., Walker, F. A., Montfort, W. R., and Czernuszewicz, R. S. *J. Am. Chem. Soc.* **2001**, *123*, 11664-11672.

38. Wang, J. L., Lu, S., Moenne-Loccoz, P., and de Montellano, P. R. O. *J. Biol. Chem.* **2003**, *278*, 2341-2347.

39. Roberts, S. A., Weichsel, A., Qiu, Y., Shelnutt, J. A., Walker, F. A., and Montfort, W. R. *Biochemistry* **2001**, *40*, 11327-11337.

40. Scheidt, W. R. and Reed, C. A. *Chem. Rev.* **1981**, *81*, 543-555.

41. Scheidt, W. R., *Systematics of the Stereochemistry of Porphyrins and Metalloporphyrins*, in *The Porphyrin Handbook*, K.M. Kadish, K.M. Smith, and R. Guilard, Editors. 2000, Academic Press: New York. p. Chapter 16.

42. Hunt, A. P. and Lehnert, N. *Acc. Chem. Res.* **2015**, *48*, 2117-2125.

43. Reisz, J. A., Zink, C. N., and King, S. B. *J. Am. Chem. Soc.* **2011**, *133*, 11675-11685.

44. Immoos, C. E., Sulc, F., Farmer, P. J., Czarnecki, K., Bocian, D. F., Levina, A., Aitken, J. B., Armstrong, R. S., and Lay, P. A. *J. Am. Chem. Soc.* **2005**, *127*, 814-815.

45. Southern, J. S., Green, M. T., Hillhouse, G. L., Guzei, I. A., and Rheingold, A. L. *Inorg. Chem.* **2001**, *40*, 6039-6046.

46. Brandstr.A, Lamm, B. O., and Junggren, J. L. *Tetrahedron Lett.* **1972**, 3173-3176.

47. Michael, M. A., Pizzella, G., Yang, L., Shi, Y. L., Evangelou, T., Burke, D. T., and Zhang, Y. *J. Phys. Chem. Lett.* **2014**, *5*, 1022-1026.

48. Zhang, Y., Guo, Z. J., and You, X. Z. *J. Am. Chem. Soc.* **2001**, *123*, 9378-9387.

49. Zhang, Y., Lewis, J. C., Bergman, R. G., Ellman, J. A., and Oldfield, E. *Organometallics* **2006**, *25*, 3515-3519.

50. Fulmer, G. R., Miller, A. J. M., Sherden, N. H., Gottlieb, H. E., Nudelman, A., Stoltz, B. M., Bercaw, J. E., and Goldberg, K. I. *Organometallics* **2010**, *29*, 2176-2179.

51. Dubowski, Y., Harush, D., and Shaviv, A. *Soil Sci. Soc. Am. J.* **2014**, *78*, 61-69.

52. Lehnert, N., Praneeth, V. K. K., and Paulat, F. *J. Comput. Chem.* **2006**, *27*, 1338-1351.

53. Richter-Addo, G. B., Wheeler, R. A., Hixon, C. A., Chen, L., Khan, M. A., Ellison, M. K., Schulz, C. E., and Scheidt, W. R. *J. Am. Chem. Soc.* **2001**, *123*, 6314-6326.

54. Abucayon, E. G., Khade, R. L., Powell, D. R., Zhang, Y., and Richter-Addo, G. B. *J. Am. Chem. Soc.* **2016**, *138*, 104-107.

55. Adler, A. D., Longo, F. R., Finarelli, J. D., Goldmacher, J., Assour, J., and Korsakoff, L. *J. Org. Chem.* **1967**, *32*, 476.

56. Adler, A. D., Longo, F. R., Kampas, F., and Kim, J. *J. Inorg. Nucl. Chem.* **1970**, *32*, 2443-2445.

57. Ogoshi, H., Watanabe, E., and Yoshida, Z. *Chemistry Lett.* **1973**, 989-992.

58. Song, B. *Bull. Korean Chem. Soc.* **2003**, *24*, 1035-1037.

59. Johnston, D. H. and Shriver, D. F. *Inorg. Chem.* **1993**, *32*, 1045-1047.

60. Reed, C. A., Mashiko, T., Bentley, S. P., Kastner, M. E., Scheidt, W. R., Spartalian, K., and Lang, G. *J. Am. Chem. Soc.* **1979**, *101*, 2948-2958.

61. Ellison, M. K., Schulz, C. E., and Scheidt, W. R. *Inorg. Chem.* **2000**, *39*, 5102-5110.

62. APEX2, *Data Collection: APEX2 Software Reference Manual*. 2007, Bruker-AXS: Madison, WI.

63. SAINT *Data Reduction: SAINT Software Refence Manual. Bruker-AXS, Madison, WI.* **2007**.

64. Frisch, M. J. T., G. W.; Schlegel, H. B.; Scuseria, G. E.; Robb, M. A.; Cheeseman, J. R.; Scalmani, G.; Barone, V.; Mennucci, B.; Petersson, G. A.; Nakatsuji, H.; Caricato, M.; Li, X.; Hratchian, H. P.; Izmaylov, A. F.; Bloino, J.; Zheng, G.; Sonnenberg, J. L.; Hada, M.; Ehara, M.; Toyota, K.; Fukuda, R.; Hasegawa, J.; Ishida, M.; Nakajima, T.; Honda, Y.; Kitao, O.; Nakai, H.; Vreven, T.; Montgomery, Jr., J. A.; J. Peralta, E.; Ogliaro, F.; Bearpark, M.; Heyd, J. J.; Brothers, E.; Kudin, K. N.; Staroverov, V. N.; Keith, T.; Kobayashi, R.; Normand,J.; Raghavachari, K.; Rendell, A.; Burant, J. C.; Iyengar, S. S.; Tomasi, J.; Cossi, M.; Rega, N.; Millam, J. M.; Klene, M.; Knox, J. E.; Cross, J. B.; Bakken, V.; Adamo, C.; Jaramillo, J.; Gomperts, R.; Stratmann, R. E.; Yazyev, O.; Austin, A. J.; Cammi, R.; Pomelli, C.; Ochterski, J. W.; Martin, R. L.; Morokuma, K.; Zakrzewski,V. G.; Voth, G. A.; Salvador, P.; Dannenberg, J. J.;

Dapprich, S.; Daniels, A. D.; Farkas, O.; Foresman, J. B.; Ortiz, J. V.; Cioslowski, J.; Fox, D. J., *Gaussian 09, Revision B.01*. 2010, Gaussian, Inc.: Wallingford CT.

65. Adamo, C. and Barone, V. *J. Chem. Phys.* **1998**, *108*, 664-675.

66. Becke, A. D. *J. Chem. Phys.* **1993**, *98*, 5648-5652.

67. Cossi, M., Barone, V., Cammi, R., and Tomasi, J. *Chem. Phys. Lett.* **1996**, *255*, 327-335.

68. Mennucci, B. and Tomasi, J. *J. Chem. Phys.* **1997**, *106*, 5151-5158.

69. Cossi, M., Barone, V., Mennucci, B., and Tomasi, J. *Chem. Phys. Lett.* **1998**, *286*, 253-260.

70. Cossi, M., Scalmani, G., Rega, N., and Barone, V. *J. Chem. Phys.* **2002**, *117*, 43-54.

71. Wachters, A. J. *J. Chem. Phys.* **1970**, *52*, 1033-&.

72. Hay, P. J. and Wadt, W. R. *J. Chem. Phys.* **1985**, *82*, 270-283.

73. Besler, B. H., Merz, K. M., and Kollman, P. A. *J. Comput. Chem.* **1990**, *11*, 431-439.

74. Vosko, S. H., Wilk, L., and Nusair, M. *Can. J. Phys.* **1980**, *58*, 1200-1211.

75. Grimme, S., Antony, J., Ehrlich, S., and Krieg, H. *J. Chem. Phys.* **2010**, *132*, 154104.

Chapter 4: Carbon−nitrogen bond formation from attack of a *C*-based nucleophile at a coordinated nitrosyl in a heme model

4.1 Introduction

The biological activity of NO is related to those of the nitroso (RNO) derivatives. However, there are no definitive molecular-level reports that reveal the NO−RNO interplay. RNO compounds are known to be carcinogenic and capable of deactivating the liver enzyme cyt P450, the muscle protein myoglobin, the blood protein hemoglobin, and other heme proteins by binding at the open coordination site of the heme to form stable heme-RNO adducts.[1,2] Carcinogenic nitrosobenzene (PhNO) metabolites are produced in biology via reductive organo-nitro[2] and oxidative amine[3] metabolism. However, given that NO is also present as a heme ligand in some heme-based proteins, one possible (chemical) way of generating carcinogenic RNO is through nucleophilic reaction of a ferric−NO species with a *C*-based nucleophile to form a stable heme-(R)NO derivative. Such nucleophilic reactions have been implicated in heme-based nitrosations by Mb (shown in Fig. 4.1) and cyt cd_1, where formally NO^+ ligands were transferred to *C*-, *N*-, *S*-, and *O*-nucleophiles.[4,5] Successful nucleophilic reaction of ferric nitrosyls in coordination (non-biological) compounds to generate RNO have been reviewed.[6]

Importantly, nucleophilic attack at the bound NO in ferric hemes is also highly relevant to the underexplored conversion of inorganic−NO_x to organo−N compounds observed in agriculture and in the environment as part of the metal-activated nitrite (NO_2^-) reduction. This underexplored research area has been highlighted by the NSF in

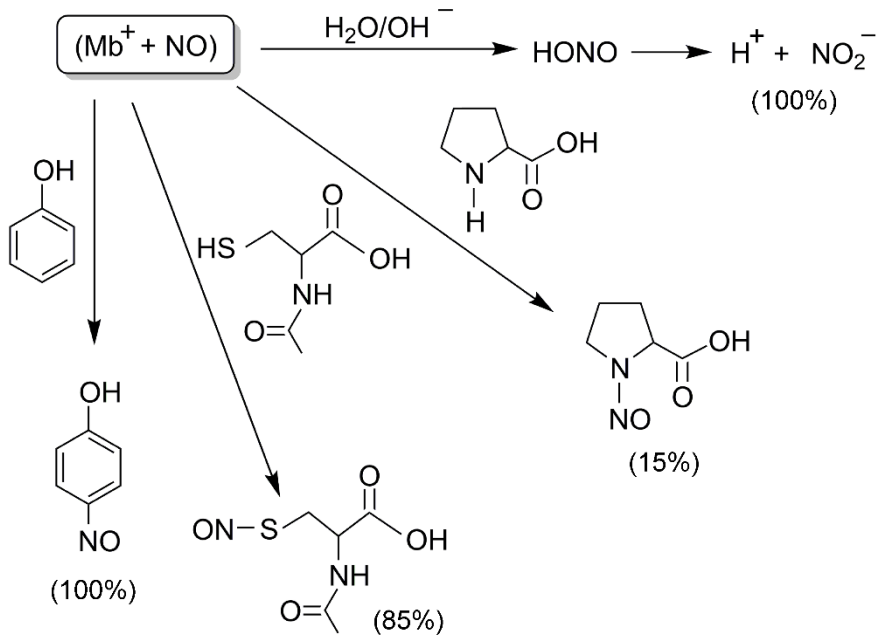

Fig. 4.1 Reaction scheme for the observed nitrosation by myoglobin via nucleophilic attack of substrates at the nitrosyl N-atom. (Mb = myoglobin)[4]

their NSF-INFEWS program[7] as a huge gap in the global nitrogen cycle. Indeed, despite the importance and biological relevance of the nucleophilic reactions of ferric−NO species in several transformations/modifications of NO, there are no definitive experimental reports on these reactions that provide chemical context to this field.

In this chapter, I focus on the reactions of the formally $\{MNO\}^6$ (M = Fe, Ru) complexes with a *C*-based nucleophile to generate new carbon−nitrogen bonds. This fills in an important gap in knowledge regarding the global N-cycle in particular relating to the inorganic−NO_x to organo−NO_x interconversion. I then extended this chemistry to nitrogen−nitrogen bond formation in these systems.

4.2 Results and Discussion

4.2.1 Reactions of the Six-coordinate {MNO}^{6} (M = Fe, Ru) Precursors with *C*−based Nucleophiles

The *in-situ* generation of the RNO molecule (*e.g.*, PhNO) from the nucleophilic reactions of heme−NO species with *C*−based nucleophiles is important in biology, and it provides insight into the NO_x reduction pathways in physiology and in agriculture.

4.2.1.1 Nitrogen−carbon and Fe−carbon bond-forming reactions

The main objective was to generate an Fe-bound PhNO species via nucleophilic reactions with *C*−based nucleophiles. Several phenyl donor compounds have been employed in this study but with variable outcomes (Scheme 4.1). In principle, any incoming *C*−based nucleophile can possibly react with ferric nitrosyls in four major ways; (i) with the Fe-bound NO^+ moiety to form a new nucleophile−NO compound (*e.g.*, RNO formation), (ii) with the Fe-center to form direct Fe−C bond (*e.g.*, organometallic Fe−phenyl formation), (iii) via electron transfer/reduction to form a stable ferrous (por)Fe(NO) species, or (iv) via deprotonation of the proximal histidine mimic (5-MeIm).

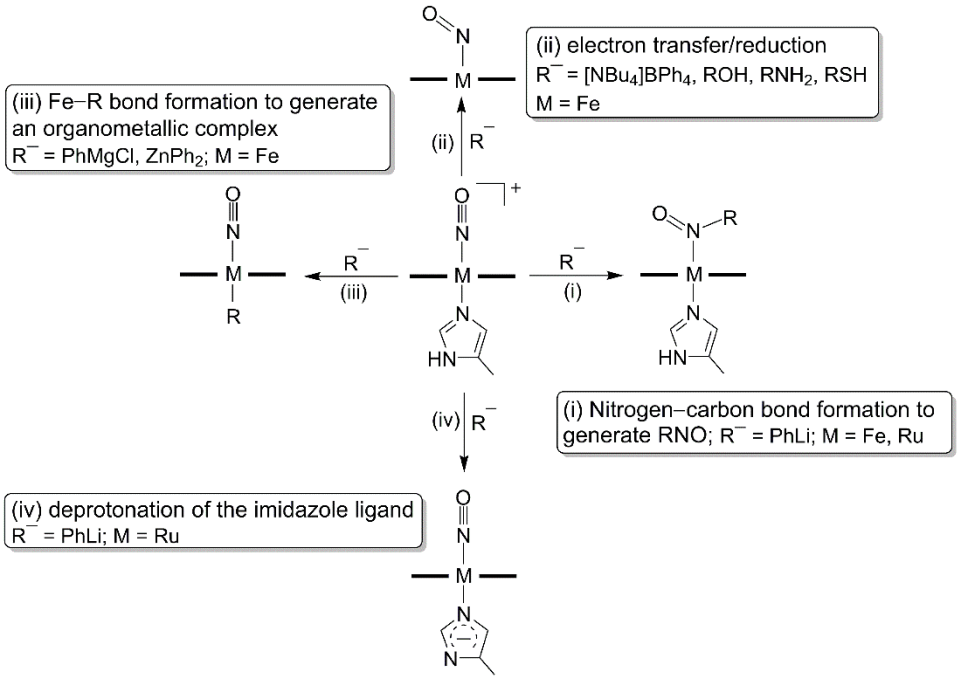

Scheme 4.1. Four major pathways by which nucleophiles can react with a six-coordinate {MNO}^{6} precursor. I show only the metal-containing products.

(a). PhLi as a nucleophile source

The reactions of PhLi with the ferric nitrosyls [(OEP)Fe(NO)(L)]OTf (L = 5-MeIm, 1-MeIm) were monitored by IR spectroscopy. In a typical reaction, the addition of 1.5 equiv of PhLi (in diethyl ether) to a stirred THF solution of [(OEP)Fe(NO)(5-MeIm)]OTf (**1**) precursor at 0 ˚C results in a gradual change in color of the solution, concomitant with the disappearance of the precursor ν_{NO} band at 1912 cm^{-1}. The IR spectrum (Fig. 4.2a) of the resulting product mixture obtained in ~50−55% isolated yield after work-up revealed the formation of (OEP)Fe(PhNO)(5-MeIm) (ν_{NO} = 1336 cm$^{-1;}$ minor), (OEP)Fe(PhNO)$_2$ (ν_{NO} = 1347 cm^{-1}; minor), and (OEP)Fe(Ph) (ν_{C-C} = 1556 cm^{-1}; major). [8] Employing the ^{15}N-labeled precursor [(OEP)Fe(^{15}NO)(5-MeIm)]OTf (ν^{15}_{NO} = 1874 cm^{-1}) for this reaction shifted the isotope sensitive band from 1347 cm^{-1} in the

unlabeled (OEP)Fe(PhNO)$_2$ product to 1319 cm^{-1} (Fig. 4.2, left) confirming its assignment as ν_{NO}. The ν^{15}_{NO} of the (OEP)Fe(Ph^{15}NO)(5-MeIm) component of the product mixture was not observed due to the overlapping porphyrin signals. The formation of both Fe−PhNO and Fe−Ph containing products suggests that phenyl anion is capable of attacking both the nitrosyl N-atom and the Fe center (left and right of Scheme 4.1).

The formation of PhNO from the nucleophilic reaction of [(OEP)Fe(NO)(5-MeIm)]$^+$ with PhLi was further supported by control experiments using PhNO to prepare an authentic sample of the (OEP)Fe(PhNO)(5-MeIm) compound. The reaction of (OEP)Fe with PhNO was characterized by the formation of a new band at 1347 cm^{-1} in the IR spectrum assigned to (OEP)Fe(PhNO)$_2$ (Fig. 4.2b, left). Addition of 1 equiv of 5-MeIm resulted in a disappearance of the band at 1347 cm^{-1} with concomitant formation of a new band at 1337 cm^{-1} assigned to the (OEP)Fe(PhNO)(5-MeIm) product (Fig. 4.2c, left). The ν_{NO} band of this authentic (OEP)Fe(PhNO)(5-MeIm) sample is identical to that of the (OEP)Fe(PhNO)(5-MeIm) product (ν_{NO} = 1336 cm^{-1}) generated from the nucleophilic attack of PhLi at the bound NO$^+$ in the [(OEP)Fe(NO)(5-MeIm)]OTf precursor.

Thus, IR spectroscopy coupled with control experiments confirmed the formation of Fe−RNO as one of the products from the nucleophilic attack of the phenyl anion at the bound ferric−nitrosyl species.

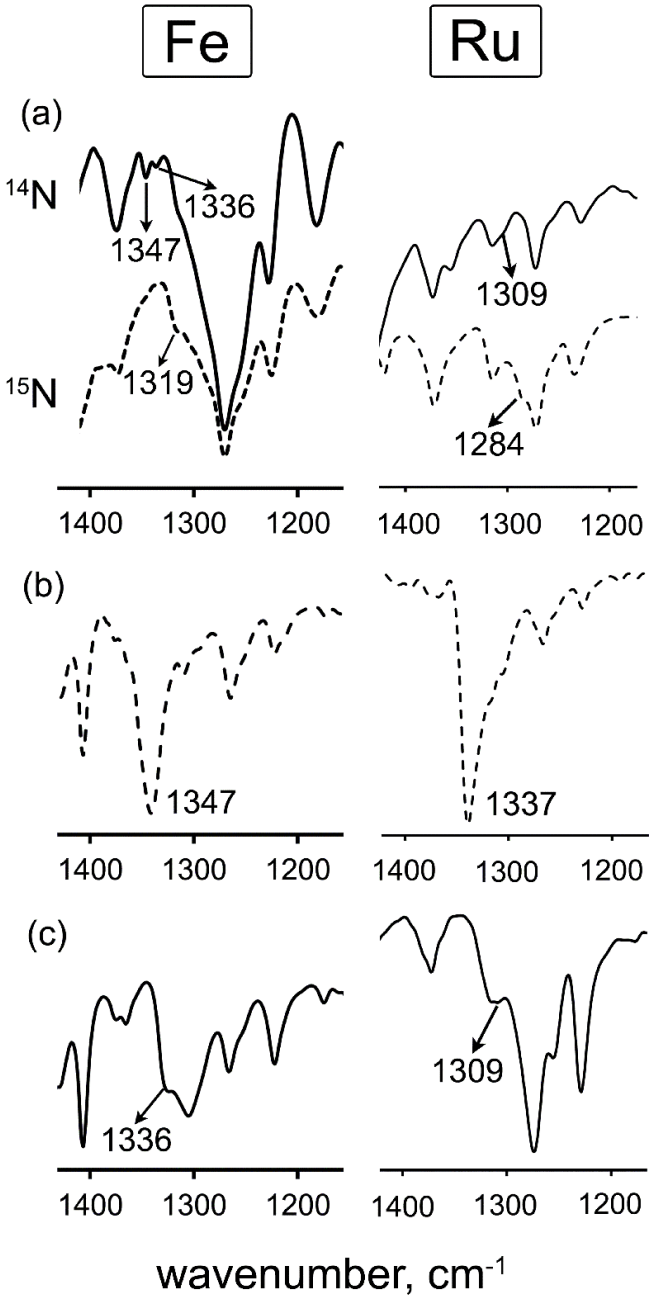

Figure 4.2. IR spectra showing the formation of the (OEP)M(PhNO)(5-MeIm) products, as KBr pellets, for Fe (*left*) and Ru (*right*). (a) formation of (OEP)Fe(PhNO)(5-MeIm) (ν_{NO} = 1336 cm^{-1}) and (OEP)Fe(PhNO)$_2$ (ν_{NO} = 1346 cm^{-1}) product mixture from the reaction of [(OEP)Fe(NO)(5-MeIm)]OTf with PhLi (*left*), and formation of the analogous (OEP)Ru(PhNO)(5-MeIm) (ν_{NO} = 1309 cm^{-1}) product (*right*). The related spectra when M–^{15}NO is used in the reactions are represented by the dotted lines. (b) IR spectra of the authentic (OEP)Fe(PhNO)$_2$ (*left*) and (OEP)Ru(PhNO)$_2$ (right). (c) IR spectra of independently synthesized (OEP)Fe(PhNO)(5-MeIm) (*left*) and (OEP)Ru(PhNO)(5-MeIm) (*right*).

The analogous reaction of [(OEP)Fe(NO)(1-MeIm)]OTf with PhLi yielded a product mixture similar to that obtained with the 5-MeIm derivative. The generation of (OEP)Fe(PhNO)(1-MeIm) and (OEP)Fe(PhNO)$_2$ as PhNO-containing products from this nucleophilic reaction was manifested by the formation of medium-to-weak bands at 1337 cm^{-1} and 1346 cm^{-1}, respectively. Employing the ^{15}N-labeled precursor [(OEP)Fe(^{15}NO)(1-MeIm)]$^+$ for this reaction shifted the isotope sensitive band from 1346 cm^{-1} (in the unlabeled compound) to 1318 cm^{-1}, confirming the band as ν_{NO} of (OEP)Fe(PhNO)$_2$. Similar to the 5-MeIm derivative described above, the $\nu_{^{15}NO}$ of the (OEP)Fe(Ph^{15}NO)(1-MeIm) in the product mixture was obscured by the overlapping porphyrin signals. In addition, a new band at 1556 cm^{-1} was assigned to $\nu_{C\text{-}C}$[8] of the other (OEP)Fe(Ph) product. Notably, the ν_{NO} of the (OEP)Fe(PhNO)(1-MeIm) product generated from the nucleophilic reaction of PhLi with [(OEP)Fe(NO)(1-MeIm)]OTf is identical to that of the previously reported (OEP)Fe(PhNO)(1-MeIm) (ν_{NO} = 1337 cm^{-1}) that was characterized by IR spectroscopy and X-ray crystallography.[9]

(b). PhMgCl as a nucleophile source

In a typical reaction, 1.5 equiv of PhMgCl was added to a stirred THF solution of the ferric nitrosyl [(OEP)Fe(NO)(5-MeIm)]OTf. The identity of the major product of the reaction was found to be highly dependent on the reaction conditions. At room temperature, the major product of the reaction is the organometallic compound (OEP)Fe(Ph) (51% isolated yield), characterized by medium-to-sharp bands at 720 cm^{-1} and 1557 cm^{-1} in its IR spectrum assigned to the $\nu_{Fe–C}$ and $\nu_{C–C}$ of the Fe−phenyl moiety, respectively.[8] The identity of the product was further confirmed by X-ray structure

determination of the crystal grown by slow evaporation from a CH_2Cl_2/*n*-hexane solution of the complex. The solid-state structure of (OEP)Fe(Ph) is shown in Figure 4.3a. When the reaction was performed at 0 ˚C, the major product is the organometallic nitrosyl compound (OEP)Fe(NO)(Ph) typified by the presence of a strong ν_{NO} band at 1784 cm^{-1} in its IR spectrum.

The solid-state structure of the organometallic compound (OEP)Fe(Ph) exhibits a wave deformation of the porphyrin core with an Fe apical displacement of 0.21 Å from the 24-atom mean plane towards the phenyl ligand (Fig. 4.3a, bottom). The $Fe{-}N_{(axial)}$ and the Fe–Np bond lengths in (OEP)Fe(Ph) are 1.9701 Å and 1.9875 Å, respectively.

(c). $ZnPh_2$ as a nucleophile source

The reaction of [(OEP)Fe(NO)(5-MeIm)]OTf with $ZnPh_2$ was performed at room temperature. Addition of 1.3 equiv of $ZnPh_2$ to a stirred THF solution of the ferric nitrosyl resulted in a disappearance of the precursor ν_{NO} band at 1912 cm^{-1} with concomitant formation of new bands at 729 cm^{-1}, 1557 cm^{-1}, and 1785 cm^{-1} assigned to ν_{Fe-C}, ν_{C-C}, and ν_{NO} of (OEP)Fe(NO)(Ph) (53% yield), respectively.[8] The ν_{NO} band at 1785 cm^{-1} is close to that of the previously reported (OEP)Fe(NO)(*p*-C_6H_4F) which was characterized by IR spectroscopy (ν_{NO} = 1791 cm^{-1}) and X-ray crystallography.[10] X-ray diffraction experiments of the crystal revealed the identity of the product as (OEP)Fe(NO)(Ph). It was observed that the same product can be formed from the reaction of (OEP)Fe(Ph) with NO gas or $[(OEP)Fe(NO)]^+$ with Ph^-. The molecular structure of the (OEP)Fe(NO)(Ph) product is shown in Fig. 4.3b.

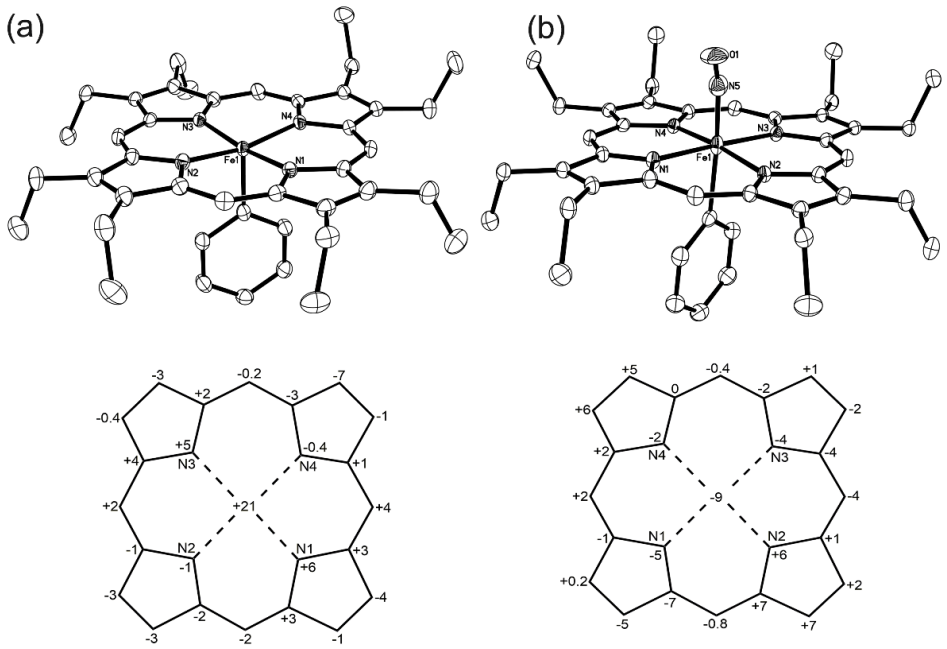

Figure 4.3. Molecular structures of (a) (OEP)Fe(Ph), and (b) (OEP)Fe(NO)(Ph). The lower panel shows the perpendicular atom displacements (in Å x 100) of the porphyrin core atoms relative to the 24-atom mean plane of the porphyrin macrocycle. Hydrogen atoms have been omitted for clarity.

There are a number of interesting features in the solid-state structure of (OEP)Fe(NO)(Ph). The Fe−$C_{(phenyl)}$ bond length of (OEP)Fe(NO)(Ph) (2.067 (2) Å) is substantially longer than that of the non-nitrosyl compound (OEP)Fe(Ph) (1.9701 (16) Å). This can be attributed to the *trans* effect of NO binding. The Fe−N(O) bond length of 1.735 (2) Å is significantly longer than those of other ferric nitrosyl complexes. The Fe−N−O linkage is slightly bent with an angle of 157.5(2)˚ which is significantly smaller than those normally expected for formally ferric $\{FeNO\}^6$ complexes (expected bond angle of 180˚). The solid-state structure of (OEP)Fe(NO)(Ph) reveals a core geometry showing an off-axis tilt of the axial nitrosyl N−atom and a bent FeNO moiety, not unlike that observed in the previously characterized (OEP)Fe(NO)(*p*-C_6H_4F).[10] However, the

asymmetry of the equatorial Fe−Np core of (OEP)Fe(NO)(Ph) displays longer Fe−Np bond lengths in the direction perpendicular to the bent FeNO group (Fig. 4.4).

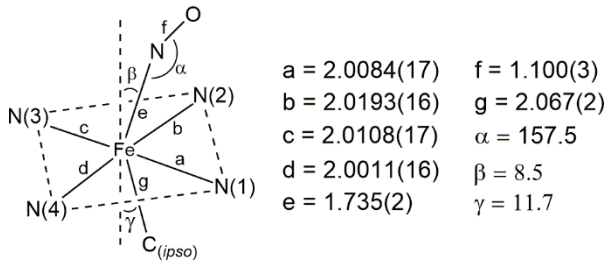

Figure 4.4. Selected geometrical parameters (in Å and degrees) of (OEP)Fe(NO)(Ph). The axial angles are with respect to the normal to the four-nitrogen porphyrin plane.

I noted that several attempts at employing other nucleophiles such as $[NBu_4]BPh_4$, alcohols, amines, sulfides, and substituted aromatic compounds (*e.g.*, $Me_2N(C_6H_5)$, phenol, aniline) in their reactions with ferric nitrosyls (Scheme 4.1, (iii)) form the known (por)Fe(NO) product as confirmed by IR spectroscopy.

The observed reactivities of *C*−based nucleophiles with the Fe-center and/or the nitrosyl N-atom in the six-coordinate ferric nitrosyls to form Fe−C and N−C bonds, respectively, are distinct from those of the hydride (H^-) reactions. As discussed in Chapter 3, the hydride anion reacts favorably with the nitrosyl N-atom of the six-coordinate ferric−NO to generate the ferrous−HNO derivative. However, the five-coordinate ferric−NO precursor reacts with H^- or *C*−based nucleophiles in a similar fashion to form Fe−H or Fe−C bonds, respectively. The observed divergent reactivities of H^- and *C*−based nucleophiles with six-coordinate ferric−NO species can be attributed, in part, to steric effects. The likely repulsion between the incoming negatively charged phenyl and the electron cloud at the porphyrin core hinders (although not completely) the close

contact between the phenyl nucleophile and the nitrosyl N-atom. This also explains why the N−C bond-forming reaction results in a very low yield of the Fe−PhNO product as compared to that forming the organometallic Fe−phenyl complex. It is noted that a mild repulsion between the H^- and the porphyrin ring during hydride attack at the FeNO moiety was also implicated from DFT calculations (Chapter 3).

4.2.1.2 Nitrogen−carbon bond formation from the reactions of the six-coordinate {RuNO}^{6} compounds with *C*−based nucleophiles

Ruthenium analogues of the formally {MNO}^{6} (M = metal) complexes are known to be more stable in solution than the iron derivatives which make them more amenable for further reactivity studies. In principle, the electrophilicity of the nitrosyl N-atom of {RuNO}^{6} is comparable to that of {FeNO}^{6}. Nucleophilic reactions of the formally {RuNO}^{6} complexes with *C*−based nucleophiles were explored to gain insight and to further our knowledge of the N−C bond formation step enabled by heme.

The products of the reactions of [(OEP)Ru(NO)(L)]BF_4 (L = 5-MeIm, 1-MeIm) with PhLi at 0 ˚C were characterized by IR and ^{15}N NMR spectroscopy, and by X-ray crystallography. The reaction of PhLi with [(OEP)Ru(NO)(L)]$^+$ in THF was usually typified by a change in color of the solution from red-brown to red-purple. For example, the addition of PhLi to a stirred solution of [(OEP)Ru(NO)(5-MeIm)]$^+$ in THF at 0 ˚C resulted in the said color change, concurrent with a decrease of the precursor ν_{NO} band at 1849 cm^{-1}. The IR spectrum of the product mixture revealed the formation of (OEP)Ru(PhNO)(5-MeIm) (ν_{NO} = 1309 cm^{-1}) and the neutral (OEP)Ru$^{(III)}$(NO)(5-MeIm) (ν_{NO} = 1839 cm^{-1}). Employing the ^{15}N-labeled precursor [(OEP)Ru(^{15}NO)(5-MeIm)]$^+$ in

the reaction shifted the isotope sensitive bands from 1309 cm^{-1} in the unlabeled product to 1284 cm^{-1} (Fig. 4.2a), and from 1839 cm^{-1} to 1804 cm^{-1}, confirming the assignment of new bands to ν_{NO} of the products. These two products were separated by neutral alumina column chromatography. The identity of the former was confirmed by single X-ray crystallography employing a crystal grown by slow evaporation of its CH_2Cl_2/*n*-hexane solution. The solid-state structure of the (OEP)Ru(PhNO)(5-MeIm) product is shown in Fig. 4.5.

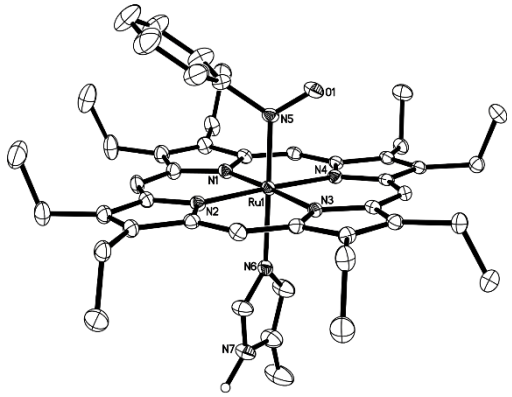

Figure 4.5. Molecular structure of (OEP)Ru(PhNO)(5-MeIm) generated from the nucleophilic reaction of $[(OEP)Ru(NO)(5\text{-MeIm})]BF_4$ with PhLi.

The reaction of the related $[(OEP)Ru(NO)(1\text{-MeIm})]^+$ compound with PhLi was performed similarly. The IR spectrum of the product mixture was characterized by the formation of new peaks at 1306 cm^{-1} and 1818 cm^{-1}. The band at 1306 cm^{-1} was assigned to ν_{NO} of the (OEP)Ru(PhNO)(1-MeIm) product, which is very close to that of the (OEP)Ru(PhNO)(5-MeIm) derivative. This compound was isolated from the product mixture by neutral alumina column chromatography using CH_2Cl_2:acetone (90:10) as the eluent. The ^{15}N NMR spectrum of the isolated (OEP)Ru(Ph^{15}NO)(1-MeIm) product is shown in Fig. 4.6. The chemical shift at δ = 541 ppm is relatively close to that of the

previously reported ^{15}N NMR chemical shift of δ = 593 ppm (vs. liq. NH_3) for the related (OEP)Fe(PhNO)(1-MeIm).[11] Also, the position of the chemical shift in the ^{15}N NMR spectrum is within the range (350 to > 800 ppm) of those expected for bent M−NO species.[12]

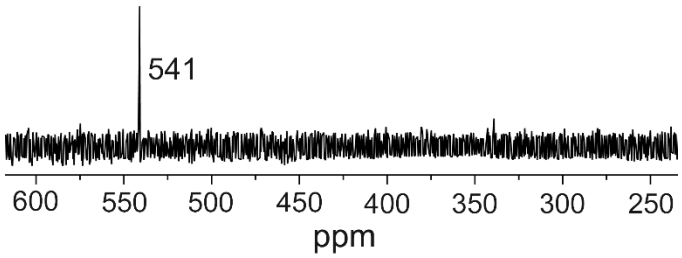

Figure 4.6. ^{15}N NMR spectrum of the isolate containing (OEP)Ru(Ph^{15}NO)(1-MeIm) (vs. liq. NH_3).

It is important to note that the observed *C*-based nucleophilic attack at bound nitrosyl ligands in heme models is unprecedented. This represents the first successful demonstration of the conversion of an inorganic−NO_x species to an organo−NO derivative mediated by synthetic metalloporphyrins.

4.2.2 Nitrogen−nitrogen Bond-forming Reactions of the Six-coordinate {MNO}^{6} (M = Fe, Ru) Precursors with *N*−based Nucleophiles

Another nucleophilic reaction that is related to the chemistry of metal-mediated NO_x activation is N−N bond formation from the reaction of {FeNO}^{6} with *N*−based nucleophiles. Catalysis of NO^+ transfer to different biologically relevant nucleophiles catalyzed by the heme-containing dissimilatory nitrite reductase (cyt. cd_1) has been reported.[5,13] Despite the importance of this biological reaction, there are no reported

examples of well-defined nucleophilic reactions of this type in heme ferric−nitrosyls to result in the N−N bond formation prior to my work in this area.

The reaction of {FeNO}^{6} with sodium azide (an N_3^- source) was monitored by gas phase and solution IR spectroscopy. The major product characterized from this reaction was N_2O (laughing gas) as shown in eq. 4.1.

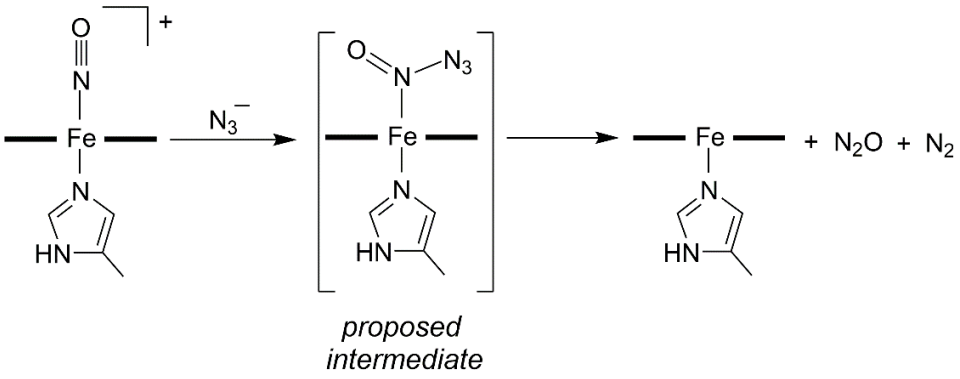

(**4.1**)

The IR spectra of the headspace gas collected from the reactions of [(OEP)Fe(NO)(L)]OTf (L = 5-MeIm, 1-MeIm) with N_3^- in THF/DMF were characterized by the formation of bands at 2237/2211 cm^{-1} which are the known asymmetric stretching bands for N_2O gas (Fig. 4.7a).[14] Interestingly, the solution IR spectrum of the reaction mixture shows the disappearance of the precursor ν_{NO} band at 1912 cm^{-1} without the formation of any ^{15}N-isotope sensitive bands, suggesting that the NO moieties of the ferric−NO species were converted into N_2O product completely.

To determine the source of the N-atoms in the generated N_2O product, the ^{15}N-labeled {FeNO}^{6} precursor was employed in this reaction. In this case, the ^{15}N-isotope sensitive bands at 2237/2211 (in the unlabeled reaction) shifted to 2189/2165 cm^{-1} which is due to the formation of the mixed N-isotope $^{14}N^{15}NO$ gas, where the terminal ^{14}N-atom

originates from azide (Fig. 4.7a).[14] It is noted that there were no bands formed that are typical for the singly-labeled $^{14}N_2O/^{15}N_2O$ gases.

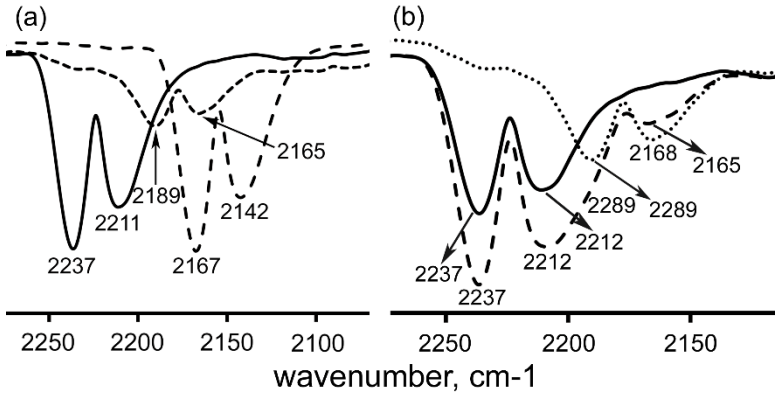

Figure 4.7. Headspace gas IR spectra from the reactions of (a) [(OEP)Fe(NO)(5-MeIm)]OTf with azide to form N_2O (*solid line trace*) and [(OEP)Fe(^{15}NO)(5-MeIm)]OTf with azide to form $^{14}N^{15}NO$ (*short broken line trace*). The *long broken line trace* (ν = 2167/2142 cm^{-1}) is a control spectrum of $^{15}N_2O$; (b) [(OEP)Ru(NO)(5-MeIm)]BF_4 with azide to form N_2O (*solid line trace*) and [(OEP)Ru(^{15}NO)(5-MeIm)]BF_4 with azide to form $^{14}N_2O$ and $^{14}N^{15}NO$ (*broken line trace*). The *dotted line trace* is a control spectrum for $^{14}N^{15}NO$ generated from the reaction of [(OEP)Fe(^{15}NO)(5-MeIm)]OTf with azide.

This reaction was extended to the Ru-analogue of {MNO}^{6}. The IR spectrum of the headspace gas collected from the reaction of [(OEP)Ru(NO)(5-MeIm)]BF_4 with N_3^- was characterized by the formation of bands at 2237/2212 cm^{-1} (Fig. 4.7b) due to the formation of N_2O. However, I observed in the solution IR spectrum of the same reaction that the disappearance of the precursor ν_{NO} band at 1849 cm^{-1} was accompanied by the formation of an ^{15}N-isotope sensitive band at 1829 cm^{-1} (not identified, $\nu_{^{15}NO}$ = 1790 cm^{-1}). Unlike the case of the {FeNO}^{6} reaction, not all of the NO ligand in the {RuNO}^{6} solution was converted to N_2O gas, as determined by solution IR spectroscopy. To probe the origin of the N_2O gas formed, the ^{15}N-labeled precursor was employed in the reaction.

Surprisingly, the IR spectrum of the headspace gas from this ^{15}N-labeled reaction contained unequal amounts of $^{14}N_2O$ (major) and $^{14}N^{15}NO$ (minor).

This result is consistent with a previous report for a non-biologically related coordination compound[15,16] that if the intermediate formed from the nucleophilic attack of N_3^- on a metal-bound NO^+ is relatively stable, the NO−N_3 adduct will cyclize to form a 5-membered N_4O ring. The N_2O and N_2 gases generated from its decomposition will then be a combination of $^{14}N_2O$, $^{14}N^{15}NO$, $^{14}N_2$, and $^{14}N^{15}N$, depending on which N−N bonds cleave as illustrated in Fig. 4.8. The unequal amounts of the $^{14}N_2O$ and $^{14}N^{15}NO$

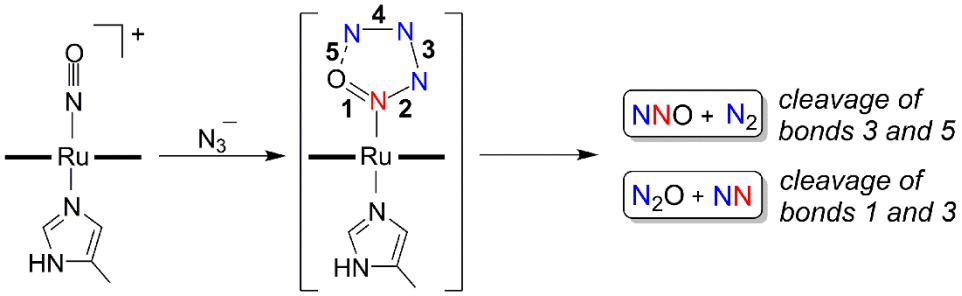

Figure 4.8. Reaction scheme illustrating how the different isotope combinations of N_2O can result from the reaction of [(OEP)Ru(^{15}NO)(5-MeIm)]BF_4 with N_3^-.

products formed implies that the N−N bond cleavage occurs while the 5-membered N_4O ring is still bound to the Ru metal center; dissociation of N_4O from Ru prior to decomposition will necessitate the formation of a statistical 1:1 mixture of $^{14}N_2O$ and $^{14}N^{15}NO$. A previous report suggested that the reaction of NaN_3 with NOCl generated N_4O which decomposed to equal amounts of N_2O and N_2.[15,17]

The successful demonstration of the nucleophilic attack of N_3^- at the bound ferric nitrosyl heme models provides insight regarding the origin of the catalytic NO^+ transfer

to the nucleophiles observed in the dissimilatory nitrite reductase and Mb-catalyzed nitrosations.

4.3 Summary and Conclusion

The formally six-coordinate ferric $\{FeNO\}^6$ complexes exhibit interesting biologically relevant reactivities towards nucleophiles. Nucleophilic attack by phenyl anions on these $\{FeNO\}^6$ species occurs at two electrophilic sites, (i) at the Fe-bound NO^+ to generate a new N−C bond, and (ii) at the Fe center to form an organometallic Fe−C bond. Such a nucleophilic reaction of a ferric nitrosyl heme model with *N*−based nucleophiles (*i.e.,* N_3^-) to generate N_2O gas was also successfully demonstrated.

This is the first successful demonstration of a *C*-based nucleophilic reaction of the formally $\{MNO\}^6$ (Fe, Ru) compounds to generate heme−RNO derivatives in heme models. This also represents the first experimental evidence of an inorganic−NO_x conversion to organo−NO derivatives mediated by metalloporphyrins. Furthermore, this provides fundamental information on the possible alternative pathways for the generation of carcinogenic nitroso compounds *in vivo*, in addition to the known reduction of nitro-compounds, and oxidation of amine to nitroso compounds. The formation of the N_2O gas from the reaction of $\{MNO\}^6$ species with N_3^- further supports the generality of the biologically relevant nucleophilic reactions involving the $\{MNO\}^6$ heme models.

4.4 Experimental Section

All reactions (except when noted otherwise) were performed anaerobically using standard Schlenk techniques under N_2 gas. Air sensitive reagents and chemical precursors

were handled inside a glove box. Solvents used in the reactions were collected under nitrogen from a Pure Solv 400-5-MD Solvent Purification System (Innovative Technology) or distilled from appropriate drying agents under an atmosphere of nitrogen.

4.4.1 Chemicals

The free base porphyrin $(OEP)H_2$ was purchased from Mid-century Chemicals and used as received. The [(OEP)Fe]OTf precursor was prepared from (OEP)FeCl in a similar manner to that described for $[(OEP)Fe]ClO_4$[18] with slight modifications. The triruthenium dodecacarbonyl ($Ru_3(CO)_{12}$, 99%) was purchased from Strem Chemicals Inc. and was used without further purification. The (OEP)Ru(CO) compound was prepared from the reaction of $(OEP)H_2$ with $Ru_3(CO)_{12}$ according to the published procedure with slight modifications.[19] The compounds silver triflate (AgOTf; OTf = O_3SCF_3, 99%), silver hexafluoroantimonate ($AgSbF_6$, 99%), 5-methylimidazole (5-MeIm, ≥99%), 1-methylimidazole (1-MeIm, ≥99%), 1-ethylimidazole (1-EtIm, ≥99%), and imidazole (Im, ≥99%) were purchased from Sigma-Aldrich and were used as received. The labeled $^{15}NOBF_4$ was synthesized following the published procedure.[20] Chloroform-*d* ($CDCl_3$, 99.96 %D) was purchased from Cambridge Isotopes, deaerated by three freeze-pump-thaw cycles, and stored over molecular sieves. Natural abundance nitric oxide (NO) gas was passed through a KOH column, then through a cold trap prior to its contact with the precursor solution to avoid the introduction of NO_x impurities. ^{15}NO (Icon Isotopes Inc., 99% ^{15}N) was used as received without further purification.

4.4.2 Instrumentation/Spectroscopy

Room temperature FT-IR spectra for compound characterization were recorded on a Bruker Tensor 27 spectrometer. UV-vis spectra were collected on a Hewlett-Packard diode array instrument (model 8453). ^{1}H NMR spectroscopy was performed on a 400 MHz Varian NMR spectrometer. X-ray diffraction data collection was performed by our staff crystallographer, Dr. Douglas R. Powell using a Bruker diffractometer equipped with an APEX ccd area detector and graphite monochromated Mo Kα radiation (λ = 0.71073 Å).

4.4.3 Syntheses

*4.4.3.1 Preparation of [(OEP)Fe(NO)(L)]OTf (L = 5-MeIm, **(1)**; 1-MeIm,**(2)**)*

The preparation, spectroscopic, and crystallographic characterization of these six-coordinate ferric nitrosyl derivatives were presented and detailed in Chapter 3.

4.4.3.2 Preparation of [(OEP)Ru(NO)(L)]BF_4 (L = 5-MeIm, 1-MeIm)

The six-coordinate {RuNO}^{6} complexes were synthesized in a similar manner as described for the preparation of [(TTP)Ru(NO)(1-MeIm)]BF_4.[21]

[(OEP)Ru(NO)(5-MeIm)]BF_4 (3): A CH_2Cl_2 (10 mL) solution of (OEP)Ru(CO) (43.1 mg, 0.065 mmol) containing 5-MeIm (6.0 mg, 0.07 mmol) was stirred for 1 h. Solid $NOBF_4$ (8.0 mg, 0.068 mmol) was added and the solution stirred for 1 h. During this time, the red solution changed to a red-brown, accompanied by the disappearance of the ν_{CO} band of the precursor (OEP)Ru(CO) at 1930 cm^{-1} and the appearance of a new band at 1849 cm^{-1} in the IR spectrum. The volume of the solution was reduced to *ca*. 2 mL

followed by the addition of anhydrous *n*-hexane to induce precipitation of a solid. The solvent was then decanted from the suspension. The residue was washed with anhydrous *n*-hexane (3x10 mL) and subsequently dried under reduced pressure to afford the product [(OEP)Ru(NO)(5-MeIm)]BF_4 in 67% isolated yield. IR (KBr): ν_{NO} = 1849 cm^{-1} ($\nu_{^{15}NO}$ = 1815 cm^{-1}). ^{15}N NMR of an ^{15}N-enriched sample ($CDCl_3$; 40.54 MHz; δ, ppm): 350 ppm (vs. liq. NH_3).

[(OEP)Ru(NO)(1-MeIm)]BF_4, (**4).** The 1-MeIm derivative namely [(OEP)Ru-(NO)(1-MeIm)]BF_4, was obtained similarly in 70% isolated yield. IR (KBr): ν_{NO} = 1852 cm^{-1} ($\nu_{^{15}NO}$ = 1814 cm^{-1}). ^{15}N NMR of an ^{15}N-enriched sample ($CDCl_3$; 40.54 MHz; δ, ppm): 340 ppm (vs. liq. NH_3)

4.4.4 Reactivity Studies

4.4.4.1 Reactions of the [(OEP)Fe(NO)(L)]OTf compounds (L = 5-MeIm, 1-MeIm) with Ph^- (Ph^- = PhLi, PhMgCl, $ZnPh_2$)

The reactions described below are representative of several reproducible nucleophilic reactions of the six-coordinate $\{FeNO\}^6$ precursors with phenyl anion to generate the (por)Fe(PhNO)(*N*-base ligand) products.

Reaction of [(OEP)Fe(NO)(5-MeIm)]OTf (1) with PhLi. To a THF (5 mL) solution of [(OEP)Fe(NO)(5-MeIm)]OTf (18.9 mg, 0.022 mmol) at 0 ˚C was added PhLi (40 μL, 1.8 mmol/mL in diethyl ether). The mixture was stirred for 30 min during which time the red-purple solution changed to a red color. The solution was filtered using a cannula to remove the LiOTf salt by-product. The volume of the filtrate was reduced to *ca*. 2 mL, and dry *n*-hexane was added to induce precipitation of a solid. The solvent was

then decanted from the suspension, and the remaining solid washed with *n*-hexane (3x10 mL) and subsequently dried in vacuo. IR (KBr): ν_{NO} = 1336 cm^{-1} assigned to (OEP)Fe(PhNO)(5-MeIm) (a minor product), ν_{NO} = 1345 cm^{-1} (ν^{15}_{NO} = 1319 cm^{-1}) assigned to (OEP)Fe(PhNO)$_2$ (a minor product), and ν_{C-C} = 1556 cm^{-1} assigned to the phenyl ligand in (OEP)Fe(Ph) (the major product). [Note: The yield was not determined for each product. The formation of Fe−PhNO minor products were reproducible.]

Reaction of [(OEP)Fe(NO)(1-MeIm)]OTf (2) with PhLi. The reaction of [(OEP)Fe(NO)(1-MeIm)]OTf with PhLi was performed in a similar manner. The IR spectrum of the final product mixture , as a KBr pellet, revealed ν_{NO} = 1337 cm^{-1} assigned to (OEP)Fe(PhNO)(1-MeIm)[9] (a minor product), ν_{NO} = 1346 cm^{-1} (ν^{15}_{NO} = 1318 cm^{-1}) assigned to (OEP)Fe(PhNO)$_2$ (a minor product), and ν = 1557 cm^{-1} assigned to the ν_{C-C} of the phenyl ligand in (OEP)Fe(Ph) (the major product).

Independent synthesis of the (OEP)Fe(PhNO)(5-MeIm). To (OEP)FeCl (19.2 mg, 0.031 mmol) in THF was added Cp_2Co (8.0 mg, 0.04 mmol) and the solution was stirred for 30 min at room temperature during which time the starting pale purple solution changed to a bright red color. The solution was filtered using a cannula to remove the Cp_2CoCl by-product, and the filtrate subsequently dried in vacuo. The resulting purple solid was redissolved in CH_2Cl_2 and nitrosobenzene (PhNO) (5.1 mg, 0.05 mmol) was added, and the solution stirred for 1 h. The volume of the solution was reduced to *ca*. 2 mL followed by the addition of anhydrous *n*-hexane to result in the precipitation of a solid. The solvent was decanted from the suspension, and the remaining solid was washed with anhydrous *n*-hexane (3x10 mL) and subsequently dried under reduced pressure. IR (KBr): ν_{NO} = 1346 cm^{-1} assigned to (OEP)Fe(PhNO)$_2$. This product was redissolved in

CH_2Cl_2 and 1 equiv of 5-MeIm was added, and the mixture stirred for additional 30 min, during which time the 1346 cm^{-1} band in the IR spectrum disappeared with concomitant formation of a new band at 1336 cm^{-1}. The solvent was removed under vacuum, and the remaining solid washed with anhydrous *n*-hexane (3x10 mL) and subsequently dried in vacuo. IR (KBr): 1336 cm^{-1} assigned to ν_{NO} of (OEP)Fe(PhNO)(5-MeIm).

Reaction of [(OEP)Fe(NO)(5-MeIm)]OTf (1) with PhMgCl. To a THF (5 mL) solution of **1** (13.5 mg, 0.016 mmol) at room temperature was added PhMgCl (20 μL 1.8 mmol/mL in diethyl ether), and the mixture was stirred for 30 min. The red-purple solution changed to light red over this time period. The solution was filter-cannulated to remove the $Mg(Cl)_x(OTf)_y$ salt by-product. The volume of the solution was reduced to *ca*. 2 mL, addition of 10 mL of anhydrous *n*-hexane resulted in the precipitation of the product in 51% isolated yield. The solvent was decanted, and the remaining solid was washed with *n*-hexane (3x10 mL). The final product was dried under reduced pressure. IR (KBr): ν = 1557 cm^{-1} assigned to the ν_{C-C} of the phenyl ligand in (OEP)Fe(Ph) (**5**). The identity of this product was confirmed by X-ray crystallography.

Interestingly, the reaction of the [(OEP)Fe(NO)(5-MeIm)]OTf with PhMgCl at 0 ˚C afforded the six-coordinate (OEP)Fe(NO)(Ph) compound with a ν_{NO} band at 1785 cm^{-1} (*c.f.* ν_{NO} = 1791 for (OEP)Fe(NO)(*p*-C_6H_4F)).[10] Single X-ray diffraction experiments confirmed the identity of the product as (OEP)Fe(NO)(Ph).

Reaction of [(OEP)Fe(NO)(5-MeIm)]OTf (1) with $ZnPh_2$. To a THF (5 mL) solution of **1** (11.5 mg, 0.014 mmol) at room temperature was added ~1.4 equiv of $ZnPh_2$ (4 mg, 0.019 mmol). The solution was stirred for 30 min during which time the red-purple solution changed to a red color. The $Zn(OTf)_2$ by-product was removed by filter

cannulation and discarded. The filtrate was reduced to *ca*. 2 mL followed by product precipitation using 10 mL of *n*-hexane. The solvent was decanted from the suspension. The remaining solid was washed with *n*-hexane (3x10 mL) and subsequently dried in vacuo. IR (KBr): ν_{NO} = 1785 cm^{-1}, and ν_{C-C} = 1557 cm^{-1} for (OEP)Fe(NO)(Ph). X-ray diffraction experiments of a suitable crystal confirmed the identity of the product as (OEP)Fe(NO)(Ph) (**6)** that was obtained in 53% isolated yield.

4.4.4.2 Reactions of [(OEP)Ru(NO)(L)]OTf (L = 5-MeIm, 1-MeIm) with PhLi

The reactions described below are representative of the nucleophilic reactions of the six-coordinate $\{RuNO\}^6$ derivatives with the phenyl anion to generate the (por)Ru(PhNO)(*N*-base ligand) derivatives.

Reaction of [(OEP)Ru(NO)(5-MeIm)]BF_4 (3) with PhLi. To a THF (5 mL) solution of **3** (53.3 mg, 0.064 mmol) at 0 ˚C was added PhLi (55 μL 1.8 mmol/mL in diethyl ether). The mixture was stirred for 2−3 h during which time the brown-red solution changed to a red-purple color. IR monitoring of the reaction revealed the disappearance of the precursor ν_{NO} band at 1849 cm^{-1} and the formation of new weak to medium bands at 1309 cm^{-1} and 1839 cm^{-1} as a NaCl plate. The $LiBF_4$ by-product was removed via filter cannulation. The filtrate was then dried in vacuo, and the remaining residue redissolved in a small amount of CH_2Cl_2 was loaded onto a neutral alumina column developed in CH_2Cl_2. The first component to elute as a red-purple CH_2Cl_2-acetone (90:10 ratio) eluent displayed a band in its IR spectrum (KBr) at 1309 cm^{-1} (ν^{15}_{NO} = 1284 cm^{-1}) assigned to (OEP)Ru(PhNO)(5-MeIm) (27% isolated yield). ^{1}H NMR ($CDCl_3$, 400 MHz; ppm): δ = 9.5 (s, 4H, methine C−*H*), 7.26 (s, $CHCl_3$), 6.12−5.25 (m,

phenyl−*H*), 5.30 (s, CH_2Cl_2), 3.86 (overlapping q, 16H, ethyl-CH_2), 1.77 (t, 24H, ethyl-CH_3), 1.27 and 0.90 (hexane impurity), 0.65 (s, 1H 5-MeIm-H), 0.23 (s, 1H 5-MeIm-H), and 0.21 (s, 3H, 5-MeIm-CH_3). The identity of this compound was confirmed by X-ray crystallography. The second component to elute using an CH_2Cl_2-acetone (50:50 ratio) solvent mixture revealed a ν_{NO} = 1839 cm^{-1} ($\nu_{^{15}NO}$ = 1804 cm^{-1}) assigned to the neutral (OEP)$Ru^{(III)}$(NO)(5-MeIm) (*c.f.* ν_{NO} = 1846 cm^{-1} for (TTP)$Ru^{(III)}$(NO)(Im))[22] in 25% isolated yield.

Reaction of [(OEP)Ru(NO)(1-MeIm)]BF_4 (4) with PhLi. The reaction was performed in a similar manner as described for compound **3** above. To a THF (5 mL) solution of **4** (20.2 mg, 0.024 mmol) at 0 ˚C was added PhLi (20 μL 1.8 mmol/mL in diethyl ether) and the mixture was stirred for 2−3 h. IR spectral monitoring of the reaction revealed the disappearance of the precursor ν_{NO} band at 1851 cm^{-1} and the formation of new weak to medium bands at 1306 cm^{-1} and 1818 cm^{-1} (as a NaCl plate). The product characterized by its ν_{NO} band at 1306 cm^{-1} ($\nu_{^{15}NO}$ = 1281 cm^{-1}) was isolated in 33% yield from the product mixture via neutral alumina column chromatography using CH_2Cl_2-acetone (90:10) as the eluent. IR (KBr): ν_{NO} = 1306 cm^{-1} assigned to (OEP)Ru(PhNO)(1-MeIm). ^{15}N NMR ($CDCl_3$; 40.54 MHz; δ, ppm) of the ^{15}N-enriched sample: 541 ppm (vs. liq. NH_3).

Independent synthesis of the (OEP)Ru(PhNO)(5-MeIm): This compound was prepared in a similar manner to that described for the known (TTP)Ru(PhNO)(5-MeIm) reported previously by us.[23] To a CH_2Cl_2 (10 mL) solution of (OEP)Ru(CO) (24.9 mg, 0.038 mmol) was added an excess of PhNO (19.5 mg, 0.182 mmol). The solution was stirred at room temperature for 30 min during which time the color changed from a pink-

red to brown. The IR (NaCl) spectrum of the product solution revealed the disappearance of the precursor ν_{CO} band at 1930 cm^{-1} with concomitant formation of a strong peak at 1337 cm^{-1} assign to ν_{NO} of (OEP)Ru(PhNO)$_2$. The volume of the solution was reduced to *ca*. 2 mL and 15 mL anhydrous *n*-hexane was added to result in the precipitation of the (OEP)Ru(PhNO)$_2$ intermediate. The solvent was decanted from the suspension. The remaining solid was washed with dry *n*-hexane (3x10 mL) and dried in vacuo. The solid was redissolved in CH_2Cl_2 (10 mL) and excess 5-MeIm was added. The solution was stirred at room temperature for 30 min during which time the solution gradually changed color from brown to a bright red-purple. Dry *n*-hexane was added to precipitate a solid. The solvent was decanted and the solid residue was washed with dry *n*-hexane. The solid was then dried under reduced pressure. IR (KBr): ν_{NO} = 1308 cm^{-1} of the (OEP)Ru(PhNO)(5-MeIm) product.

4.4.4.3 Reactions of [(OEP)M(NO)(5-MeIm)]X (M = Fe, Ru; X = OTf^-, BF_4^-) with NaN_3

Reaction of [(OEP)Fe(NO)(5-MeIm)]OTf (1) with NaN_3. To a THF/DMF (4:1 mL) solution of **1** (17.9 mg, 0.021 mmol) was added 1.5 equiv of NaN_3, and the reaction solution stirred for 2−3 h inside a sealed Schlenk tube. The headspace gases were then vacuum transferred to an IR gas cell (10 cm in length) for IR spectral data collection. IR (gas): $\nu_{as N_2O}$ = 2237/2211 cm^{-1} ($\nu_{as ^{14}N^{15}NO}$ = 2191/2165 cm^{-1}) assigned to the newly-formed N_2O gas.[14] The IR spectrum of the product solution showed that no ^{15}N-isotope sensitive products formed that remained in the solution.

Reaction of [(OEP)Ru(NO)(5-MeIm)]BF_4 (3) with NaN_3. To a THF/DMF (4:1 mL) solution of **3** (37.7 mg, 0.045 mmol) was added 1.5 equiv of NaN_3, and the mixture stirred for 5 h in a sealed Schlenk tube. The headspace gases were vacuum transferred to an IR gas cell (10 cm in length) for gas phase IR spectral data collection. IR (gas): ν_{asN_2O} = 2237/2211 cm^{-1} assigned to N_2O gas.[14] In the case of the ^{15}N-labeled precursor, the reaction of [(OEP)Ru(^{15}NO)(5-MeIm)]OTf with N_3^- afforded the formation of both $^{14}N_2O$ (major) and $^{14}N^{15}NO$ (minor). IR (gas): ν_{asN_2O} = 2237/2211 cm^{-1} and $\nu_{as^{14}N^{15}NO}$ = 2191/2165 cm^{-1}.

4.4.5 X-ray Crystallography

A summary of the crystal and refinement data for compounds **5**, **6**, and **7** are shown in Table 4.1.

Table 4.1. Crystallographic collection and refinement parameters.

Complex	**5**	**6**	**7**
Empirical formula	$C_{42}H_{49}FeN_4$	0.936[$C_{42}H_{49}FeN_5O$]	($C_{46}H_{55}RuN_7O$).(C_6H_{14})
(fw)	(665.70)	(696.11)	909.12
Crystal system, space group	triclinic, $P\bar{1}$	triclinic, $P\bar{1}$	triclinic, $P\bar{1}$
Unit cell dimensions			
a (Å)	12.242(3)	10.4934(7)	9.552(3)
b (Å)	12.250(2)	10.7584(7)	13.686(5)
c (Å)	13.635(3)	15.7322(10)	19.441(7)
α (°)	112.282(4)	67.9924(11)	91.654(6)
β (°)	94.156(4)	68.7999(11)	93.988(6)
γ (°)	110.395(4)	64.7066(10)	109.163(50
Volume (Å^3)	1723.4(6)	1718.71(19)	2391.2(14)
Z, Z'	2, 1	2,1	2, 1
F(000)	710	740	964
Absorption coefficient(mm^{-1})	0.474	0.490	0.372
Max. and min. trans.	0.920 and 0.891	0.953 and 0.828	0.986 and 0.818
Theta range (°)	1.661 to 28.363	1.320 and 27.507	1.052 to 27.576
Reflections collected	40669	39818	29772
Independent reflections	8602[R(int) = 0.0343]	7880[R(int) = 0.0366]	10849[R(int) = 0.0487]
Data/restraints/parameters	8602/8/443	7880/157/478	10849/0/553
$wR(F^2$ all data) [a]	$wR2$ = 0.1015	$wR2$ = 0.1402	$wR2$ = 0.1187
$R(F$ obsd data) [b]	$R1$ = 0.0378	$R1$ = 0.0502	$R1$ = 0.0480
Goodness-of-fit on F^2	1.000	1.006	1.020
Observed data [$I > 2\sigma(I)$]	7539	6767	8727
Largest and mean shift / s.u.	0.001 and 0.000	0.001 and 0.000	0.001 and 0.000
Largest diff. peak and hole (e/Å^3)	0.886 and −0.347	1.390 and −0.362	1.148 and −0.606

4.5 References

1. Lee, J., Chen, L., West, A. H., and Richter-Addo, G. B. *Chem. Rev.* **2002**, *102*, 1019-1065.

2. Murayama, M. *J. Biol. Chem.* **1960**, *235*, 1024-1028.

3. Fukuto, J. M., Di Stefano, E. W., Burstyn, J. N., Valentine, J. S., and Cho, A. K. *Biochemistry* **1985**, *24*, 4161-4167.

4. Wade, R. S. and Castro, C. E. *Chem. Res. Toxicol.* **1990**, *3*, 289-291.

5. Kim, C.-H. and Hollocher, T. C. *J. Biol. Chem.* **1984**, *259*, 2092-2099.

6. Bottomley, F. *Acc. Chem. Res.* **1978**, *11*, 158-163.

7. Feeding the World in the 21st Century: Grand Challenge in the Nitrogen Cycle. *NSF-INFEWS* **2015**, 1-37.

8. Guilard, R., Boisselier-Cocolios, B., Tabard, A., Cocolios, P., Simonet, B., and Kadish, K. M. *Inorg. Chem.* **1985**, *24*, 2509-2520.

9. Xu, N., Christian, J. H., Dalal, N. S., Abucayon, E. G., Lingafelt, C., Powell, D. R., and Richter-Addo, G. B. *Dalton Trans.* **2015**, *44*, 20121-20130.

10. Richter-Addo, G. B., Wheeler, R. A., Hixon, C. A., Chen, L., Khan, M. A., Ellison, M. K., Schulz, C. E., and Scheidt, W. R. *J. Am. Chem. Soc.* **2001**, *123*, 6314-6326.

11. Godbout, N., Sanders, L. K., Salzmann, R., Havlin, R. H., Wojdelski, M., and Oldfield, E. *J. Am. Chem. Soc.* **1999**, *121*, 3829-3844.

12. Mason, J., Larkworthy, L. F., and Moore, E. A. *Chem. Rev.* **2002**, *102*, 913-934.

13. Goretski, J. and Hollocher, T. C. *Biochem. and Biophys. Res. Commun.* **1991**, *175*, 901-905.

14. Dubowski, Y., Harush, D., and Shaviv, A. *Soil Sci. Soc. Am. J.* **2014**, *78*, 61-69.

15. Douglas, P. G. and Feltham, R. D. *J. Am. Chem. Soc.* **1972**, *94*, 5254-5258.

16. Wolfe, S. K., Andrade, C., and Swinehart, J. H. *Inorg. Chem.* **1974**, *13*, 2567-2572.

17. Schulz, A., Tornieporthoetting, I. C., and Klapotke, T. M. *Angew. Chem. Int. Ed.* **1993**, *32*, 1610-1612.

18. Ogoshi, H., Watanabe, E., and Yoshida, Z. *Chem. Lett*. **1973**, 989-992.

19. Rillema, D. P., Nagle, J. K., Barringer, L. F., Jr., and Meyer, T. J. *J. Am. Chem. Soc*. **1981**, *103*, 56-62.

20. Connelly, N. G., Draggett, P. T., Green, M., and Kuc, T. A. *J. Chem. Soc., Dalton Trans.* **1977**, 70-73.

21. Lee, J. and Richter-Addo, G. B. *J. Inorg. Biochem.* **2004**, *98*, 1247-1250.

22. Bohle, D. S., Hung, C.-H., Powell, A. K., Smith, B. D., and Wocadlo, S. *Inorg. Chem.* **1997**, *36*, 1992-1993.

23. Lee, J., Twamley, B., and Richter-Addo, G. B. *Can. J. Chem.* **2002**, *80*, 1252-1258.